# Quantitative Applications of Optical Coherence Tomography Angiography in Ophthalmology

Zhongdi Chu

A dissertation

submitted in partial fulfillment of the

requirements for the degree of

Doctor of Philosophy

University of Washington

2019

Reading Committee:

Ruikang K. Wang, Chair

Kathryn L. Pepple

Ying Zheng

Program Authorized to Offer Degree:

Bioengineering

University of Washington

## Abstract

**Quantitative Applications of Optical Coherence Tomography Angiography in Ophthalmology**

Zhongdi Chu

Chair of the Supervisory Committee:
Professor Ruikang K. Wang
Bioengineering

Optical coherence tomography (OCT) angiography (OCTA) is a recently developed non-invasive functional imaging technique that have been widely utilized in ophthalmology. OCTA is capable of providing three dimensional detailed information of ocular vasculature and has great potentials for vascular quantification. In this thesis, OCTA's capacity in imaging microvasculature in great detail was demonstrated in human eyes, techniques to improve image quality and contrast were proposed and validated. With clinically available OCTA systems' data, quantitative analysis tools for both retinal choroidal microvasculature were developed and tested on diseased subjects. The reliability of proposed quantitative algorithms was tested with intra-visit scans and the robustness was tested with data from a wide range of disease diagnoses. Overall, this dissertation presents a set of tools that can describe the integrity of human ocular microvasculature reliably and objectively.

# TABLE OF CONTENTS

# LIST OF FIGURES

# LIST OF TABLES

# LIST OF JORNAL PUBLICATIONS

Part of this dissertation has been published in the selected journal papers from the list below.

*: Equally Contributed Authors.

[1] **Chu Z**, Zhou H, Cheng Y, Zhang Q, Wang RK. Improving visualization and quantitative assessment of choriocapillaris with swept source OCTA through registration and averaging applicable to clinical systems. Scientific reports. 2018;8(1):16826.

[2] **Chu Z**, Zhang Q, Zhou H, Shi Y, Zheng F, Gregori G, Rosenfeld PJ, Wang RK. Quantifying choriocapillaris flow deficits using global and localized thresholding methods: a correlation study. Quantitative Imaging in Medicine and Surgery. 2018.

[3] **Chu Z**, Chen C-L, Zhang Q, Pepple K, Durbin M, Gregori G, Wang RK. Complex signal-based optical coherence tomography angiography enables in vivo visualization of choriocapillaris in human choroid. Journal of biomedical optics. 2017;22(12):121705.

[4] **Chu Z**, Lin J, Gao C, Xin C, Zhang Q, Chen C-L, Roisman L, Gregori G, Rosenfeld PJ, Wang RK. Quantitative assessment of the retinal microvasculature using optical coherence tomography angiography. Journal of biomedical optics. 2016;21(6):066008-.

[5] **Chu Z**, Gregori G, Rosenfeld PJ, Wang RK. Quantification of choriocapillaris with OCTA: a comparison study. (Under Review)

[6] **Chu Z***, Weinstein JE*, Wang RK, Pepple KL. Quantitative Analysis of the Choriocapillaris in Uveitis Using Swept Source Optical Coherence Tomography Angiography. (Under Review)

[7] Kim AY*, **Chu Z***, Shahidzadeh A, Wang RK, Puliafito CA, Kashani AH. Quantifying microvascular density and morphology in diabetic retinopathy using spectral-domain optical coherence tomography angiography. Investigative ophthalmology & visual science. 2016;57(9):OCT362-OCT70.

[8] Pepple KL*, **Chu Z*,** Weinstein J, Munk MR, Van Gelder RN, Wang RK. Use of En Face Swept-Source Optical Coherence Tomography Angiography in Identifying Choroidal Flow Voids in 3 Patients With Birdshot Chorioretinopathy. JAMA ophthalmology. 2018;136(11):1288-92.

[9] Zhou H, **Chu Z**, Zhang Q, Dai Y, Gregori G, Rosenfeld PJ, Wang RK. Attenuation correction assisted automatic segmentation for assessing choroidal thickness and vasculature with swept-source OCT. Biomedical Optics Express. 2018;9(12):6067-80.

[10] Chang R, **Chu Z**, Burkemper B, Lee GC, Fard A, Durbin MK, Reznik A, Xu BY, Kashani A, Varma R. Effect of Scan Size on Glaucoma Diagnostic Performance using OCT Angiography En Face Images of the Radial Peripapillary Capillaries. Journal of glaucoma. 2019.

[11] Koulisis N, Kim AY, **Chu Z**, Shahidzadeh A, Burkemper B, de Koo LCO, Moshfeghi AA, Ameri H, Puliafito CA, Isozaki VL. Quantitative microvascular analysis of retinal venous occlusions by spectral domain optical coherence tomography angiography. PloS one. 2017;12(4):e0176404.

[12] Pakzad-Vaezi K, Khaksari K, **Chu Z**, Van Gelder RN, Wang RK, Pepple KL. Swept-Source OCT Angiography of Serpiginous Choroiditis. Ophthalmology Retina. 2017.

[13] Richter GM, Madi I, **Chu Z**, Burkemper B, Chang R, Zaman A, Sylvester B, Reznik A, Kashani A, Wang RK. Structural and Functional Associations of Macular Microcirculation in the Ganglion Cell-Inner Plexiform Layer in Glaucoma Using Optical Coherence Tomography Angiography. Journal of glaucoma. 2018;27(3):281-90.

[14] Richter GM, Sylvester B, **Chu Z**, Burkemper B, Madi I, Chang R, Reznik A, Varma R, Wang RK. Peripapillary microvasculature in the retinal nerve fiber layer in glaucoma by optical coherence tomography angiography: focal structural and functional correlations and diagnostic performance. Clinical ophthalmology. 2018;12:2285.

[15] Zhang Q, Chen C-L, **Chu Z**, Zheng F, Miller A, Roisman L, de Oliveira Dias JR, Yehoshua Z, Schaal KB, Feuer W. Automated quantitation of choroidal neovascularization: a comparison study between spectral-domain and swept-source OCT angiograms. Investigative ophthalmology & visual science. 2017;58(3):1506-13.

[16] Richter GM, Chang R, Situ B, **Chu Z**, Burkemper B, Reznik A, Bedrood S, Kashani AH, Varma R, Wang RK. Diagnostic Performance of Macular Versus Peripapillary Vessel Parameters by Optical Coherence Tomography Angiography for Glaucoma. Translational vision science & technology. 2018;7(6):21-.

[17] Kim, A.Y., Rodger, D.C., Shahidzadeh, A**., Chu Z**., Koulisis, N., Burkemper, B., Jiang, X., Pepple, K.L., Wang, R.K., Puliafito, C.A. and Rao, N.A., 2016. Quantifying retinal microvascular changes in uveitis using spectral-domain optical coherence tomography angiography. American journal of ophthalmology, 171, pp.101-112.

[18] Kashani AH, Green KM, Kwon J, **Chu Z**, Zhang Q, Wang RK, Garrity S, Sarraf D, Rebhun CB, Waheed NK. Suspended Scattering Particles in Motion: A Novel Feature of OCT Angiography in Exudative Maculopathies. Ophthalmology retina. 2018;2(7):694-702.

[19] Do JL, Sylvester B, Shahidzadeh A, Wang RK, **Chu Z**, Patel V, Richter GM. Utility of optical coherence tomography angiography in detecting glaucomatous damage in a uveitic

patient with disc congestion: A case report. American Journal of Ophthalmology Case Reports. 2017;8:78-83.

[20] Miller AR, Roisman L, Zhang Q, Zheng F, de Oliveira Dias JR, Yehoshua Z, Schaal KB, Feuer W, Gregori G, **Chu Z**. Comparison between spectral-domain and swept-source optical coherence tomography angiographic imaging of choroidal neovascularization. Investigative ophthalmology & visual science. 2017;58(3):1499-505.

[21] Thulliez M, Zhang Q, Shi Y, Zhou H, **Chu Z**, de Sisternes L, Durbin MK, Feuer W, Gregori G, Wang RK. Correlations Between Choriocapillaris Flow Deficits Around Geographic Atrophy and Enlargement Rates Based on Swept Source OCT Imaging. Ophthalmology Retina. 2019.

[22] Zhang Q, Rezaei KA, Saraf SS, **Chu Z**, Wang F, Wang RK. Ultra-wide optical coherence tomography angiography in diabetic retinopathy. Quantitative imaging in medicine and surgery. 2018;8(8):743.

[23] Zhang Q, Shi Y, Zhou H, Gregori G, **Chu Z**, Zheng F, Motulsky EH, De Sisternes L, Durbin M, Rosenfeld PJ. Accurate estimation of choriocapillaris flow deficits beyond normal intercapillary spacing with swept source OCT angiography. Quantitative imaging in medicine and surgery. 2018;8(7):658.

[24] Thulliez M, Zhang Q, Shi Y, Zhou H, **Chu Z**, de Sisternes L, Durbin MK, Feuer W, Gregori G, Wang RK, Rosenfeld PJ. Correlations Between Choriocapillaris Flow Deficits Around Geographic Atrophy and Enlargement Rates Based on Swept Source OCT Imaging. Ophthalmology Retina. 2019.

[25] Zhang Q, Zheng F, Motulsky EH, Gregori G, **Chu Z**, Chen C-L, Li C, de Sisternes L, Durbin M, Rosenfeld PJ. A Novel Strategy for Quantifying Choriocapillaris Flow Voids Using Swept-Source OCT Angiography. Investigative ophthalmology & visual science. 2018;59(1):203-11.

[26] Zhao Z, Faith P, Pakzad-Vaezi K, **Chu Z**, Wang RK, Mudumbai RC, Rezaei KA. PARACENTRAL ACUTE MIDDLE MACULOPATHY ASSOCIATED WITH BILATERAL OPTIC DISK SWELLING AND MENINGITIS. Retinal cases & brief reports. 2017.

[27] Zheng F, Zhang Q, Motulsky EH, de Oliveira Dias JR, Chen C-L, **Chu Z**, Miller AR, Feuer W, Gregori G, Kubach S. Comparison of neovascular lesion area measurements from different swept-source OCT angiographic scan patterns in age-related macular degeneration. Investigative ophthalmology & visual science. 2017;58(12):5098-104.

[28] Zheng F, Zhang Q, Shi Y, Russell JF, Motulsky EH, Banta JT, **Chu Z**, Zhou H, Patel NA, de Sisternes L. Age-Dependent Changes in the Macular Choriocapillaris of Normal Eyes Imaged with Swept-Source OCT Angiography. American journal of ophthalmology. 2019.

[29] Koulisis N, Moysidis SN, Yonekawa Y, Dai YL, Burkemper B, Wood EH, Lertjirachai I, Todorich B, Khundkar TZ, **Chu Z**, Wang RK. Correlating Changes in the Macular Microvasculature and Capillary Network to Peripheral Vascular Pathology in Familial Exudative Vitreoretinopathy. Ophthalmology Retina. 2019.

# ACKNOWLEDGEMENTS

First and foremost, I want to express my deepest gratitude for my parents, Jinqiao Chu and Xiaohong Su, none of this would have been possible without their unconditional love and support. They have always been great role models, providing me with motivation and inspiration to achieve my goals in life.

I would like to express my gratitude and appreciation for my Ph.D. mentor and advisor, Dr. Ruikang Wang. Dr. Wang has been a constant support ever since I joined the Biophotonics and Imaging Laboratory. Not only did he provided me with excellent research environment and resources, but he also mentored with example, showed me the importance of industriousness, productivity and persistence as a researcher. I would also like to express my gratitude to my collaborators and clinical mentors: Dr. Kathryn L. Pepple, Dr. Philip J Rosenfeld, Dr. Amir Kashani and Dr. Grace M. Richter. Dr. Pepple from department of ophthalmology, University of Washington has been such a great collaborator and mentor during my Ph.D. studies, her brilliance, work ethic and passion for research has been a great inspiration. Dr. Rosenfeld from Bascom Palmer Eye Institute has taught me a great deal about age-related macular degeneration; his clear and logical research mindset has also provided me with great guidance. Dr. Kashani and Dr. Richter USC Roski Eye Institute have also provided me with a great deal of help in my diabetic retinopathy and glaucoma related research work.

I also owe a debt of gratitude to many of my colleagues. Shaozhen Song, Qinqin Zhang, Chieh-li Chen, Yuxuan Cheng and Hao Zhou have all helped me in research with their knowledge and rapport. I would also like to thank my dear non-academic friends during my Ph.D. years, for always encouraging me, supporting me and occasionally distracting me and keeping me sane.

# DEDICATION

*To my dear mother and farther,*

# Chapter 1. INTRODUCTION

Blindness and vision impairment have a significant impact on quality of life, it can affect people's abilities in performing daily tasks as well as interacting with others. As of 2015, it is estimated that globally, 36.0 million people were blind, 216.6 million people had moderate to severe visual impairment, and 188.5 million had mild visual impairment.[1] Out of those people living with vision impairment, approximately 80% are considered preventable or treatable. Globally, the leading causes are uncorrected refractive errors, cataract, age-related macular degeneration, glaucoma, diabetic retinopathy, corneal opacity and trachoma. In low- and middle-income countries, uncorrected refractive errors and cataract are the main reasons for vision impairment while in upper-middle- and high-income countries, retinal diseases are the main causes of visual impairment. According to the nation eye institute, an estimated 1.3 million Americans are blind and 2.9 million Americans have low vision. The estimated annual economic burden of vision loss and eye diseases and vision disorders in In the U.S. is $139 billion. The leading causes of legal blindness are age-related macular degeneration, diabetic retinopathy, glaucoma, cataract, etc (prevalence varies in different ethnic groups).[2]

In clinical ophthalmology, disease diagnosis in the early stage is crucial because corresponding treatment can be more effective and some irreversible damages can be prevented or delayed. In order to achieve accurate early diagnosis, multiple ophthalmic imaging techniques have been developed to aid the traditional slit lamp microscope. Fluorescein angiography (FA) can visualize retinal vasculature with injected dye, providing helpful information about blood-retinal barrier integrity and neovascularization.[3] Indocyanine green angiography (ICGA), which absorbs and reflects in the near infrared portion of the spectrum (805 nm and 835 nm, respectively), is especially helpful to image choroidal vascular circulation and visualize

choroidal neovascularization.[4] However, both FA and ICGA requires injection of contrast agents and could lead to life-threatening complications.[5] Ultrasonography is a contrast-free imaging technique with deep penetration, but it requires physical contact with the eye ball and has a relatively low axial resolution of ~200 μm.[6] More recently developed high-frequency ultrasound can provide a higher axial resolution of ~ 20 μm but due to limited penetration, making this technology only suitable for anterior segment imaging.[7]

## 1.1 Optical Coherence tomography

Optical Coherence Tomography (OCT) is a recently developed optical imaging technique that can provide depth-resolved volumetric information of biological tissues non-invasively[8]. The fast imaging speed (up to 1.7MHz[9]), high axial resolution (up to 1 μm[10]), satisfactory imaging depth (~3mm [11]) and contrast-free nature of OCT has made it a popular tool in multiple areas of in vivo imaging, especially in ophthalmology. The basic principle of OCT is low coherence interferometry. Briefly speaking, the broad band light emitted from the light source is split into two arms: the reference arm and the sample arm. The reference arm travels to the reference mirror and reflects back, the sample arms travels to the sample and reflects back from different depths in the sample. Then the two arms of reflected light will recombine and result in observable interference when the optical path length from two arms matches. Currently, there are two types of OCT: time domain OCT (TDOCT) and Fourier domain OCT (FDOCT).

## 1.2 Time domain Optical Coherence tomography

Time domain OCT is the first generation of OCT, the basic system configuration is illustrated in Figure 1.1. TDOCT employs a mechanical scanning mirror in the reference arm to achieve depth-resolved imaging and its scanning speed is its major limitation. With a general A-

line scanning speed of a ~2-8 kHz, TDOCT has been mostly used to take 2 dimensional (2D) scans of human eye. To achieve 3 dimensional (3D) imaging, multiple 2D B-scans need to be taken and stacked into a volume. Since the patient's ability to keep still to avoid motion artifacts decays with elongate imaging time, 3D image with TDOCT has been challenging.

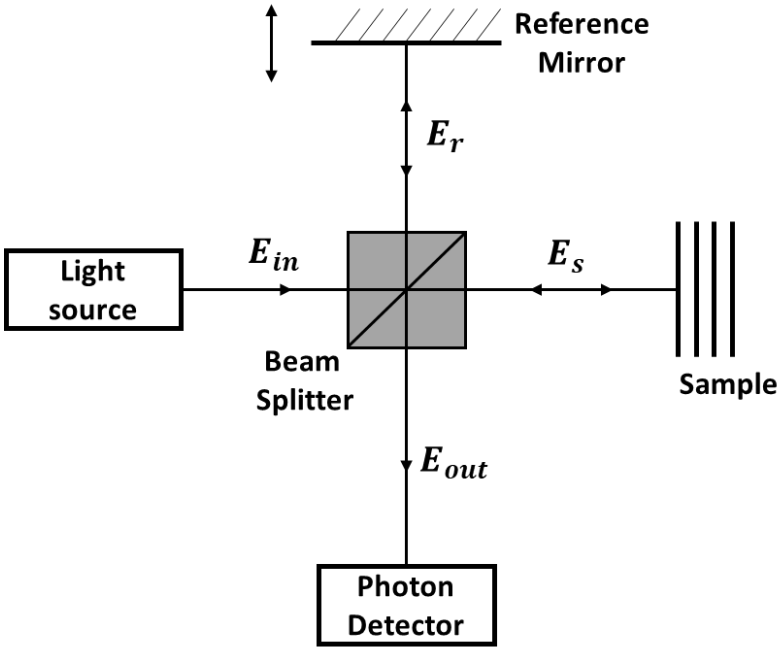


Figure 1.1. Schematic illustration of basic TDOCT set up.
$\boldsymbol{E_{in}}$ incident light; $\boldsymbol{E_r}$ reference light; $\boldsymbol{E_s}$ sample light; $\boldsymbol{E_{out}}$ detected light.

## 1.3 FOURIER DOMAIN OPTICAL COHERENCE TOMOGRAPHY

Fourier domain OCT shares the same basic principles with TDOCT, instead of using a scanning mirror to achieve interference at different depth in the sample, it utilizes spectral interference where the depth information provided by the scanning mirror in TDOCT is coded as a function of the wavelength of light. Using FDOCT, the A-line scanning speed can be significantly improved to achieve 3D scans of biological samples with less motion artifacts.

Based on interferogram detection, FDOCT can be further divided into two types: spectral domain OCT (SDOCT) and swept-source OCT (SSOCT).

### 1.3.1 *Spectral domain optical coherence tomography*

Spectral domain OCT utilizes a broadband light source and a spectrometer, Figure 1.2 illustrates its basic system configuration. By using a spectrometer, the recombined interference pattern is split by grating into different wavelength components and then detected by line-scanning camera. The detected interferogram will then further go through Fourier transform where the frequency corresponds to the depth and the amplitude corresponds to the reflectivity of the sample, resulting in an A-line. By utilizing a 2D scanner, multiple A-lines can be acquired to consist a B-scan, and multiple B-scans can be acquired to achieve a 3D volume.

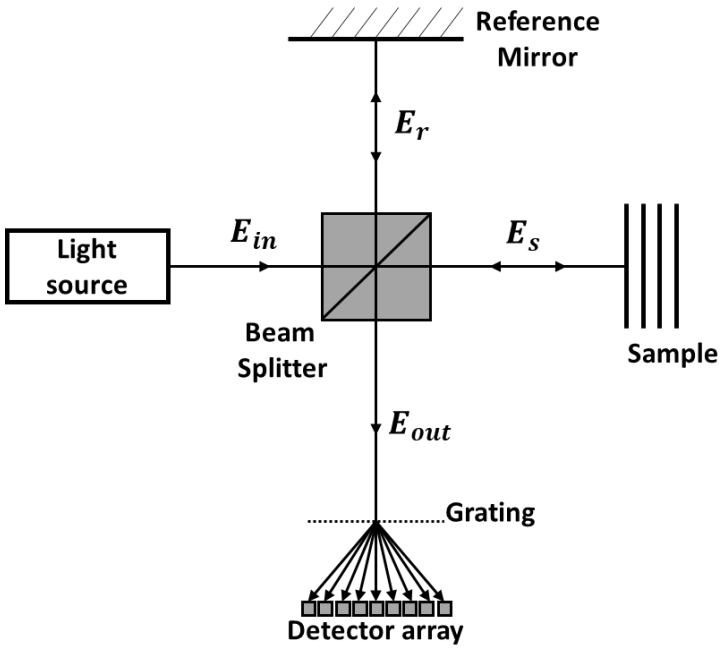


Figure 1.2. Schematic illustration of basic FDOCT set up.
$\boldsymbol{E_{in}}$ incident light; $\boldsymbol{E_r}$ reference light; $\boldsymbol{E_s}$ sample light; $\boldsymbol{E_{out}}$ detected light.

### 1.3.2 *Swept-source optical coherence tomography*

Differently from SDOCT, SSOCT utilize a frequency scanning light source and photodiode detector. In SDOCT, the interferogram spectrum was resolved spatially through a grating while in SSOCT, the interferogram spectrum was acquired by the timely sweeping of different light wavelength from the light source. Each swept wavelength corresponds to the different depth locations in the sample after Fourier transform. With a slightly different configuration. SSOCT presents several advantages over SDOCT, such as lower sensitivity loss along depth, longer imaging range and higher imaging speed.[12, 13] Currently, there are both SDOCT and SSOCT commercial systems that have been FDA approved and commonly used in ophthalmology clinics.

## 1.4 OPTICAL COHERENCE TOMOGRAPHY ANGIOGRAPHY

OCT can provide depth-resolved volumetric data from biological samples, based on OCT, a new angiography technique called OCT angiography (OCTA) has also been recently introduced. When acquiring 3D data from a biological sample, signals from both static and moving particles were obtained, from one time point. If multiple OCT scans were acquired along different time points, signal from static tissues have a very low variation while signal from moving particles would have a very high variation, in both amplitude and phase. OCTA differentiates vessels from surrounding static tissues by analyzing the differences in OCT signal variation along time. During the last decade, several OCTA techniques have been developed, they can be categorized into different groups based on if they utilize the 1) phase part of OCT signal, 2) amplitude part of the signal or 3) whole complex OCT signal.

Regardless of the specific OCTA approaches, OCTA has been widely adopted in both research and clinical ophthalmology imaging for various of ocular diseases. There are a couple of reasons for the rising popularity of OCTA compared to traditional dye-based angiography: 1) OCTA is quicker and safer; 2) OCTA is a 3D imaging technique that can provide detailed vascular information of different layers of ocular tissues; 3) OCTA has a high lateral resolution that can image ocular capillaries. With these advantages, OCTA is a lot more suitable than FA and ICGA to be widely used in ophthalmology for diseases screening and early diagnosis. In this thesis, the objective is to develop quantitative vasculature analyses with OCTA and ultimately to provide reliable and objective tools for clinicians and researchers to quantitatively describe the integrity of various ocular vascular networks in human eyes.

# Chapter 2. QUANTITATIVE ASSESSMENT OF THE RETINAL MICROVASCULATURE USING OPTICAL COHERENCE TOMOGRAPHY ANGIOGRAPHY

## 2.1 INTRODUCTION

Optical coherence tomography angiography was recently introduced for the imaging of microvascular networks in the human eye [14]. Recent investigations using OCTA have been mainly focused on showcasing its applications in visualizing the flow characteristics of microvascular diseases within the macula, such as age-related macular degeneration (AMD) [15] and diabetic retinopathy (DR) [16, 17], the two leading causes of blindness worldwide [18, 19]. In addition, OCTA has documented microvascular abnormalities in other macular diseases such as branch retinal vein occlusion (BRVO), central retinal vein occlusion (CRVO)[20], and macular telangiectasia type 2 (MacTel2) [21]. Compared with conventional dye-based angiography, OCTA offers a safer, faster, and more cost effective alternative for ocular imaging of the macular vasculature. Overall, the combination of OCT and OCTA can present integrated structural and flow information of the human eye in vivo, opening new opportunities for both qualitative and quantitative analysis of ocular diseases.

Optical microangiography (OMAG) [14] is one of the many OCTA approaches that utilizes the intrinsic properties of particles' (e.g. red blood cells) motion, to highlight the contrast between signals due to RBCs and signals due to static tissues. Unlike other OCTA approaches such as speckle variance [22], split-spectrum amplitude decorrelation angiography (SSADA) [23], and phase variance [24], OMAG is able to harness motion information to the fullest extent by exploiting both amplitude and phase information contained within the OCT signals.

Therefore, OMAG is able to produce OCT angiography with better vascular connectivity, higher signal-to-noise ratio (SNR), and higher sensitivity to capillary blood flows [25]. Consequently, OMAG is being established as a valuable tool for the investigation of ocular diseases both qualitatively [26] and quantitatively [27].

To objectively assess the OCT angiograms, a number of studies have introduced vessel area density (VAD) [28, 29], vessel skeleton density (VSD) [28, 30], and non-perfusion area [29]. These parameters have been reported useful in the analyses of disease progression in DR and AMD. While promising, there are limitations when evaluating indices individually. VAD provides information about the function of vascular network by calculating the percentage of area occupied by vessels on OCTA images. Thus, a change in VAD is coupled with changes in both vessel length and vessel size. Since the decrease of microvascular perfusion is sometimes accompanied with vessel dilation, VAD alone is only capable of providing partial information about vascular abnormalities. Similarly, VSD falls short because it only evaluates the vessel length without taking the vessel size information into account. Moreover, compared with fluorescein angiography (FA), it is difficult for OCTA to convey information about vascular leakage since it detects the existence of moving particles while FA senses the diffusion of injected dyes into the extravascular space. To our best knowledge, there has not been an attempt to extract vascular information other than vessel density from OCT angiograms.

In this study, we introduce a comprehensive quantitative OMAG analysis for OCTA vascular images. We propose to use the following metrics to quantitatively describe the OCTA images: vessel area density (VAD), vessel skeleton density (VSD), vessel diameter index (VDI), vessel perimeter index (VPI) and vessel complexity index (CVI). We illustrate the usefulness of these metrics by using five clinical cases. We also assess the repeatability of these metrics by

using OCTA scans captured from the same patients at different times. With our comprehensive quantitative OMAG strategy, we aim to provide clinicians and physicians with a rapid strategy for interpreting OCT angiograms from multiple perspectives and to help simplify the process of identifying pathological vascular features so as to enable the objective assessment of disease progression and treatment monitoring.

## 2.2 METHODS

An automated tool with a user interactive interface was developed to quantify the abnormalities in the retinal vasculature from multiple perspectives. Included within this tool are the quantitative parameters of VAD, VSD, VPI, VDI, and VCI. To demonstrate the usefulness of these parameters, we used OMAG *en face* images generated by using both spectral domain OCT (SD-OCT) and swept-source OCT (SS-OCT) angiography prototype instruments.

SD-OCT data was acquired using a Cirrus HD 5000 SD-OCT angiography system prototype (Carl Zeiss Meditec Inc., Dublin, CA, USA), with an 840 nm central wavelength and a 68 KHz A-scan rate. The scanning protocol in this system provided a field of view (FOV) of 2.4 mm × 2.4 mm, with 245 lines in each B-scan and 245 locations in the slow axis (where 4 repeated B-scans were acquired at each location). Equipped with FastTrac$^{TM}$ [31] technology, a custom sized montage scan could be acquired to give a widefield image with high resolution and high definition. In this study, customized scans consisting of nine motion-tracked smaller cubes, with a total field of vieiw (FOV) of 6.72 mm × 6.72 mm, were collected from each subjects.

SS-OCT data was acquired using a modified CIRRUS prototype containing a swept source laser provided by Carl Zeiss Meditec Inc., which had a 1,050 nm central wavelength and 100 kHz A-scan rate. SS-OCT provided a FOV of 3mm × 3mm with 300 A-lines per B-scan and a total of 300 B-scans centered at the fovea. To achieve OMAG imaging of the vascular

networks, a previously described repeated B-scan protocol was implemented to acquire the volumetric OCTA data [26, 31].

All participants in this study were consented before OCTA imaging, following the tenets of Declaration of Helsinki, in compliance with the Health Insurance Portability and Accountability Act. The study was approved by the Institutional Review Board of the University of Washington (UW), Seattle, as well as the University of Miami Miller School of Medicine, Miami. All SD-OCT scans were obtained at the University of Washington Eye Institute, while all SS-OCT scans were obtained at the Bascom Palmer Eye Institute, University of Miami Miller School of Medicine. Subjects with the diagnosis of DR and BRVO were prospectively enrolled at the UW Medicine Eye Institute, and subjects with diagnosis of MacTel2 were enrolled in the MacTel project and imaged at the Bascom Palmer Eye Institute.

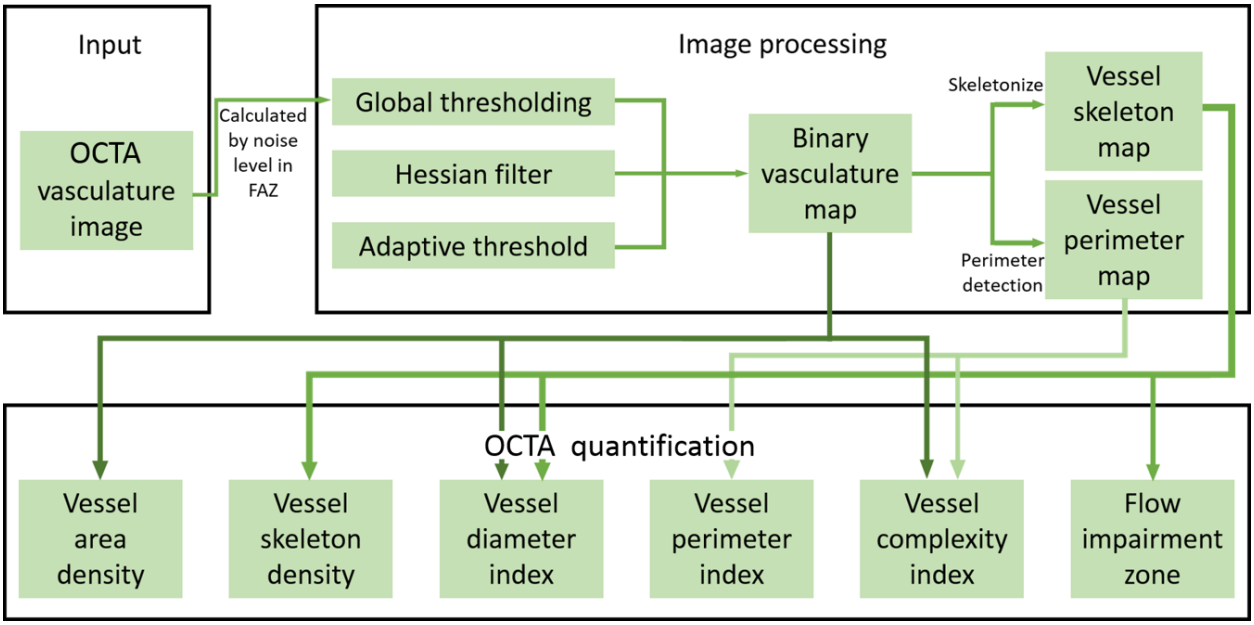


Figure 2.1. Overview of the quantitative OMAG algorithm.

Figure 2.1 shows a flowchart providing an overview of the processes involved in our proposed quantitative approach to OCTA metrics. First, a 2D *en face* OMAG image (Figure 2.2A) is generated from the volumetric data using a semi-automatic segmentation software [32].

This image is processed into a binary image in MATLAB (R2015b, MathWorks, Inc.) using a global threshold, hessian filter [33], and adaptive threshold. The global threshold is determined by the noise level in the foveal avascular zone (FAZ) that is selected with a user interactive interface by asking the operator to click on the center and edge of FAZ. This global threshold is then applied to the entire image. Then, hessian filter and adaptive threshold are combined to generate a binary vessel map (Figure 2.2 B). In doing so, the information of vessel area can be obtained. Second, a skeletonized vessel map is created (Figure 2.2C), where every vessel, regardless of its size or diameter, is represented by a single pixel line. This way, the information of vessel length can be obtained. Last, the vessel perimeter or the edges of vessels are detected and contoured as the vessel perimeter map (Figure 2.2D) to give the information about vessel perimeter. All five quantitative indices are calculated based on these three binary vessel maps, i.e., vessel area map, skeletonized vessel map and vessel perimeter map. Note that there are only two values, 1 and 0, in the binary maps where 1 represents white pixel (i.e., existence of blood vessel) and 0 the black pixel (i.e., absence of blood vessel).

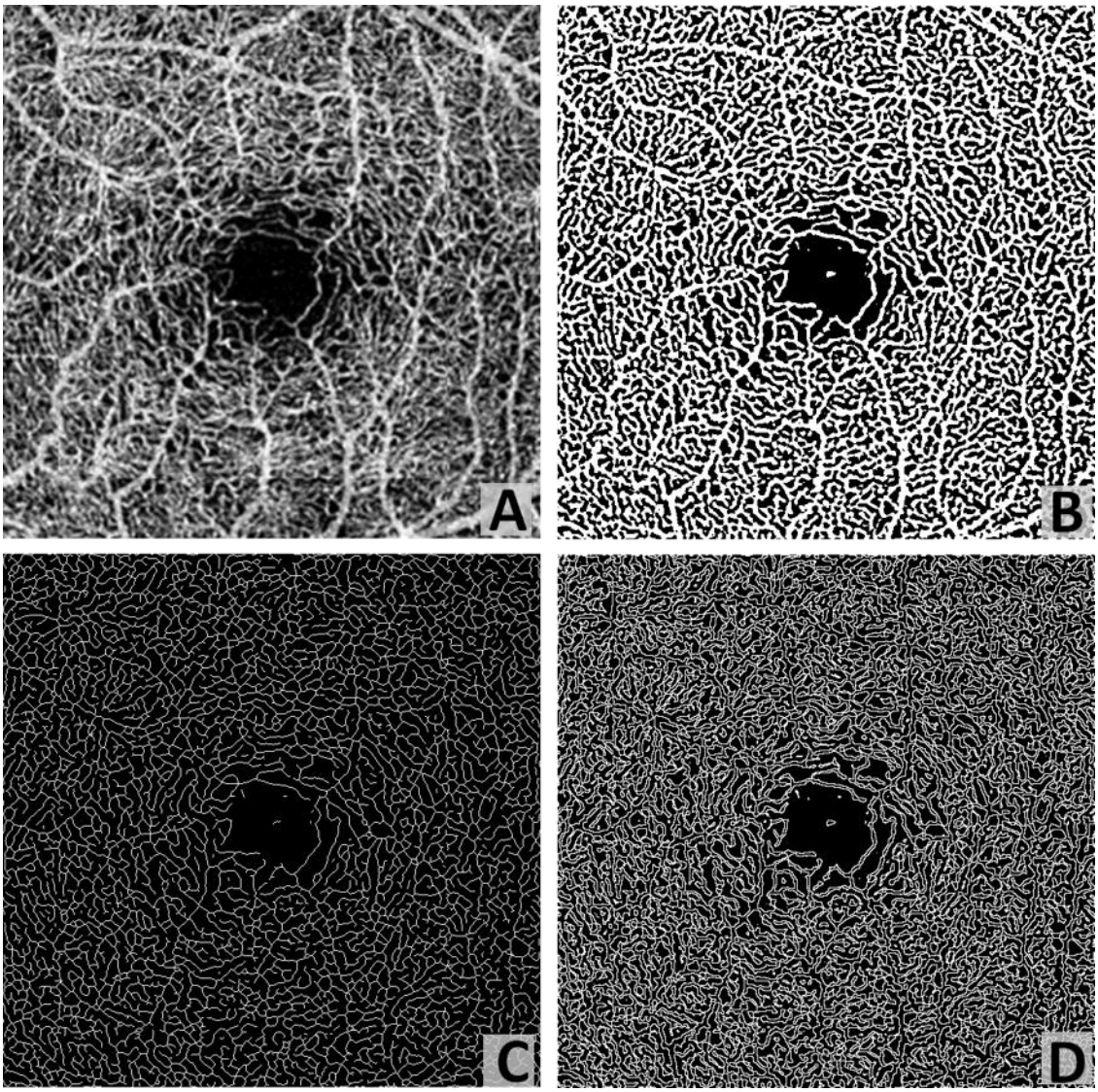


Figure 2.2. Representative OMAG images to illustrate the quantitative analysis algorithm. (A) Original en face OMAG image. (B) Vessel area map, a binarized vasculature image using hessian filter and adaptive threshold. This image is used for vessel area density, vessel diameter index and vessel complexity index quantification. (C) Vessel skeleton map, which is obtained by iteratively deleting the pixels in the outer boundary of the vessel area map until one pixel remained along the width direction of the vessels. This image is used for vessel skeleton density and vessel diameter index quantification. (D)Vessel perimeter map, which is obtain by detecting the edge of vessels in the vessel area map and deleting pixels that are not on the edge of vessels. This image is used for vessel perimeter index and vessel complexity index quantification.

VAD is calculated as a unitless ratio of the total image area occupied by the vasculature to the total image area in the binary vessel maps:

$$VAD = \frac{\sum_{i=1,j=1}^{n} A_{(i,j)}}{\sum_{i=1,j=1}^{n} X_{(i,j)}} \quad (1)$$

Where *A(i, j)* represents the pixels occupied by vessel area (white pixels on Figure2.2B) and *X(i, j)* all the pixels in the vessel area map (all pixels on Figure2.2B). (*i,j*) are the pixel coordinates in the OCTA image (assuming with a size of *n x n* pixel array). With this definition, VAD provides the best estimate of real vessel density as it takes both vessel length and vessel diameter into consideration. However, a complication would be that VAD remains unchanged when there are decreased perfusion and vessel dilation happening at the same time, potentially resulting in false negatives on the vascular abnormality. Furthermore, other than computing a single VAD for the whole OCT angiogram, we could also produce a spatially resolved VAD map. A down sampled block map was generated with 25x25 (pixels) block size, the map was resized to original size and Gaussian filtered with a 3x3 (pixels) kernel. All maps were generated in the same fashion.

VSD is calculated as the ratio of the length occupied by the blood vessels to the total area in the skeletonized vessel map:

$$VSD = \frac{\sum_{i=1,j=1}^{n} S_{(i,j)}}{\sum_{i=1,j=1}^{n} X_{(i,j)}} \quad (2)$$

Where *S(i, j)* represents the pixels registered as vessel length (white pixels on Figure2.2C) and *X(i, j)* represents all the pixels in the skeletonized vessel map (all pixels on Figure 2.2C). The unit for VSD is pixel/pixel$^2$. VSD quantifies the vessel density by only considering whether or not the vessel exists, which is simply an assessment of the vessel length density regardless of the vessel diameters. Since every vessel is presented as a single pixel line,

large vessels and small capillaries contribute equally to the VSD quantification. Consequently, compared to VAD, VSD would be more sensitive to the perfusion changes at the capillary levels.

VDI is calculated using both the vessel area map and the skeletonized vessel map to yield the averaged vessel caliber as follows:

$$VDI = \frac{\sum_{i=1,j=1}^{n} A_{(i,j)}}{\sum_{i=1,j=1}^{n} S_{(i,j)}} \quad (3)$$

Where *A(i, j)* represents all the pixels registered as vessel area (white pixels on Figure2B) and *S(i, j)* represents the pixels registered as vessel length (white pixels on Figure 2.2C). The unit of VDI is pixel and can be converted into micron by multiplying VDI with pixel size, all VDI data in this article has been converted into microns. VDI calculates the averaged vessel caliber within the image, it does not reflect the change in vessel density. VDI presents the vessel size information regardless of the vessel length, therefore it is sensitive to vascular dilation in the OCTA images. With the VDI map, localized vascular dilation would be easily identified and serve as a marker of vascular abnormalities.

VPI is calculated using the vessel perimeter map as the ratio of the vessel perimeter to the total area of the OCTA image:

$$VPI = \frac{\sum_{i=1,j=1}^{n} P}{\sum_{i=1,j=1}^{n} X_{(i,j)}} \quad (4)$$

Where *P(i, j)* represents all the pixels within vessel perimeters (white pixels on Figure 2.2D) and *X(i, j)* represents all the pixels in the vessel perimeter map (Figure 2.2D). The unit for VPI is pixel/pixel$^2$. Contrary to vessel skeleton density, vessel perimeter index uses the perimeter to present every vessel, which includes both the length and the diameter, similar to vessel area density.

VCI is calculated using both the vessel perimeter map and the vessel area map, defined as:

$$VCI = \frac{(\sum_{i=1,j=1}^{n} P_{(i,j)})^2}{4\pi \sum_{i=1,j=1}^{n} X_{(i,j)}} \quad (5)$$

Where *P(i, j)* represents all the pixels enclosed by vessel perimeters (white pixels on Figure 2.2D) and *A(i, j)* represents all the pixels of the vessel area (white pixels on Figure 2.2B). VCI is also a unit less parameter and derived from the digital image processing discipline [34]. With the vessel complexity map, specific locations where the vascular morphology is less complicated could be identified. In most cases, decreased perfusion would result in less complex vasculature. To the best of our knowledge, this is the first time vessel complexity index has been introduced to quantify morphological characteristics of the retinal vasculature, though fractal dimension has been previously used to describe vascular tortuosity [28]. To better illustrate the concept of VCI, an example study was conducted to test the robustness of this quantitative parameter. As shown in Figure 2. 3, five images were selected as examples for the calculation of VCI. Both binary area images and perimeter images are shown in Figs. 3A-J, and the VCI results for each image are plotted in 3K, with the exact values denoted above each data point. We find a positive relationship between VCI and its visual complexity; as VCI increases, the visual complexity of the image also increases. Theoretically the VCI value should be 1 for a circle, however due to the discrete nature of computing, computed VCI value for a circle would always be larger than 1, depends on sampling rate. All computed VCIs have been normalized according to this 1.5711 to 1 ratio.

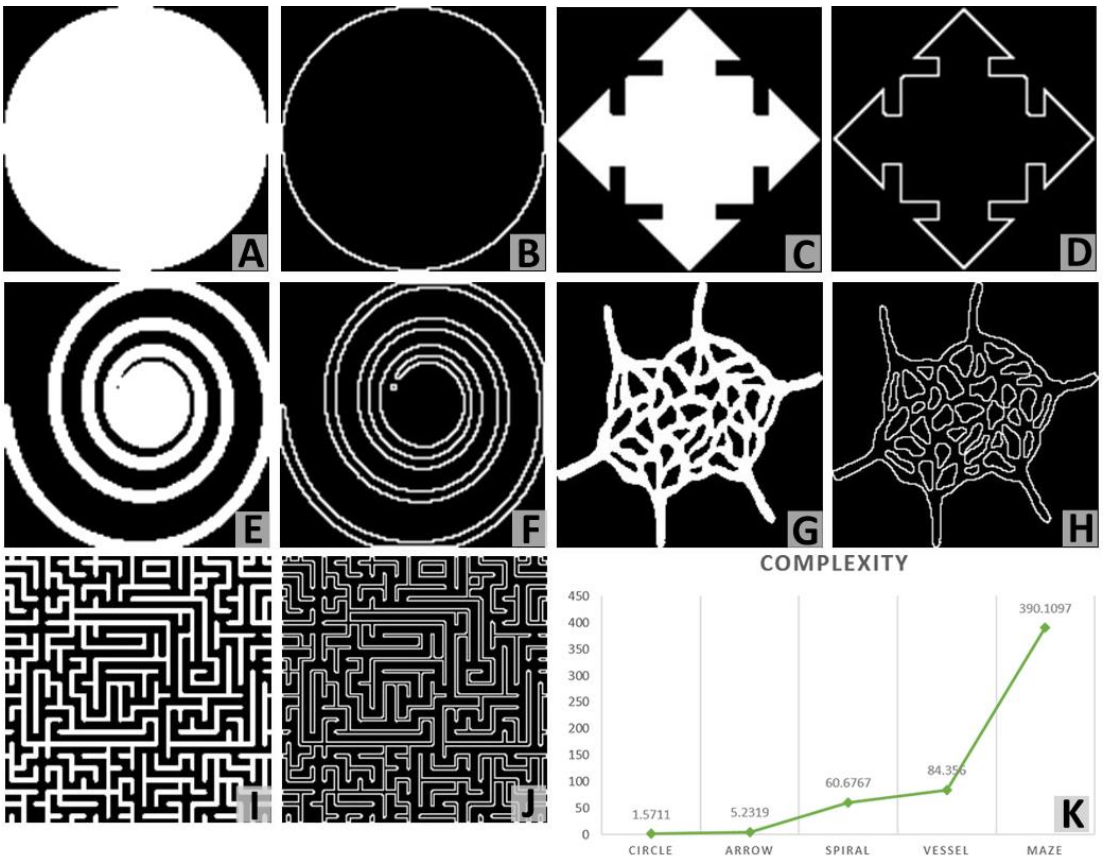


Figure 2.3. Demonstration of vessel complexity index quantification.
(A-J) are area images (A, C, E, G, I) and perimeter images (B, D, F, H, J), with increasing visual complexity. Plot (K) shows their corresponding quantification of vessel complexity index.

## 2.3 RESULTS

Five illustrative cases are shown to demonstrate the usefulness of all the quantitative metrics that we propose.

### 2.3.1 *Retinal vasculature and quantitative maps in normal case*

The three dimensional (3D) nature of OCT allows for segmentation of vascular plexi located at different physiological depths within the retina. Using a validated semi-automatic segmentation software [32], we separated the retinal microvasculature into three distinct physiological layers: the superficial vascular network encompassing from ganglion cell layer to

inner plexiform layer, the deep vascular network including the outer plexiform layer, and the avascular outer retinal layer extending from outer nuclear layer to retinal pigment epithelium as shown in Figure 2. 4B. We excluded the retinal nerve fiber layer in the following examples since the vasculature in this layer is morphologically different from the vasculature in the deeper retinal layers, especially for large FOV OCTA scans [35]. However, this layer can be included in the analysis if needed. Figure 2. 4A shows the *en face* OCTA image with maximum projection, with the color scheme for segmented vascular plexus shown in Figure 2. 4B.The vessel density map, vessel diameter map and vessel complexity map are shown in Figure 2. 4C-E. Figure 2.s 4F-H were obtained by combining Figure 2.s 4C-E with the vessel map (Figure 2. 2B), which would make it easier to localize the particular vessels of interests. Good correlations can be observed in these three maps with the anatomic features of the retinal vasculature. For both vessel density map and vessel diameter map, large vessels in the superficial layer appear red, which represents higher density/diameter; in the vessel complexity map, large vessels are blue since they are less complex in morphology compared to capillaries. Figure 2. 4H shows the overlay of vessel complexity map and deep retinal vascular layer *en face* maximum projection image, where we have observed that the red regions in the vessel complexity map correspond to the radial fan-like capillaries that originate from vertical anastomosis connecting superficial and deep network.

With the algorithm, VAD, VSD, VPI, VDI and VCI can all be quantified from the OMAG images. For illustrative purposes, an example of five quantitative indices has been given in Table 1 based on the entire retinal image (Figure 2.4A). We also see provided the higher resolution overlaid images in attached Supplementary Figure for more information.

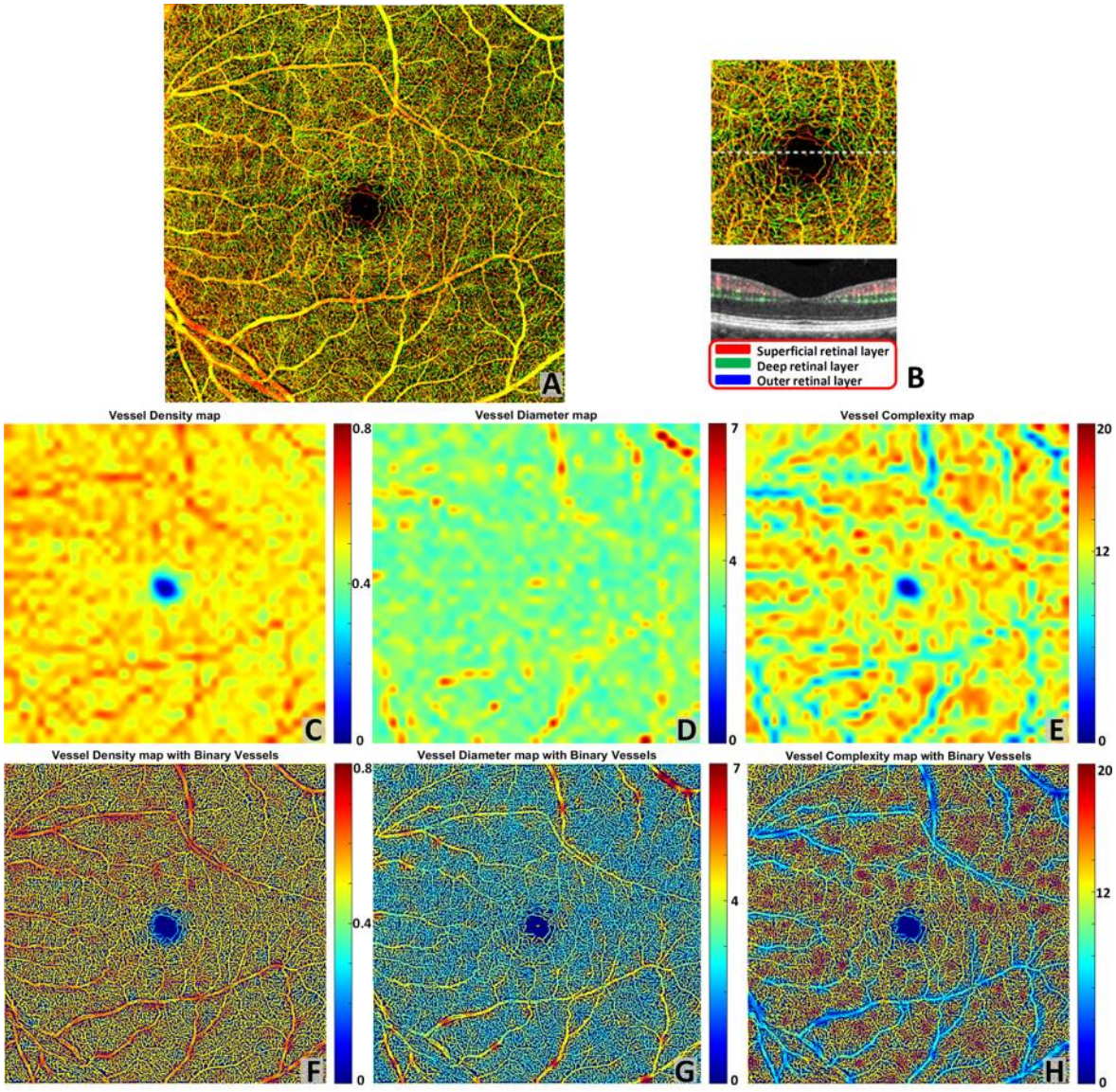


Figure 2.4. Quantitative OMAG on a normal case.

(A) OMAG en face image with montage scanning protocol, 9 smaller cubes are stitched together to achieve a 6.72 mm × 6.72 mm FOV. (B) Illustration of segmentation and color code strategy. Retinal vasculature was segmented into superficial slab, deep slab and the avascular outer retina slab. Red represents superficial plexus, green represents deep plexus and blue for outer retinal slab. All three slabs were integrated together and represented in a color image in (A), excluding retinal nerve fiber layer. (C) Vessel density map. This map shows the vessel area density of image (A), calculated using a kernel moving across the entire OMAG image. (D) Vessel diameter map. This map shows the local averaged vessel diameter index using the same calculation method as (C). (E) Vessel complexity map. This map shows the local averaged vessel

complexity index using the same calculation method as (C). (F-H) Integration of quantitative maps (C-E) with binary vessel area map (Figure 2.4 B).

### 2.3.2 *Microvascular abnormality and flow impairment in diabetic retinopathy*

Quantitative OMAG analysis of an eye with non-proliferative diabetic retinopathy (NPDR) is shown in Figure 2. 5. A late phase fluorescein angiographic image shown in Figure 2. 5A corresponds well to the OMAG image shown in Figure 2. 5B. The areas of flow impairment are automatically detected according to our vessel skeleton map and superimposed onto OMAG *en face* image in green (Figure 2. 5C). In doing so for this example, the negation of the vessel skeleton map was first obtained, and then the morphological operations were conducted to close smaller unconnected regions (600 pixels) that come naturally between vessels. The size of this region was determined according to normal OCTA scans, and might differ among different OCT systems. Lastly, a Gaussian filter (with a kernel size of 3 pixel * 3 pixel) was used to smooth the edges of the detected regions of flow impairment. Vessel density, diameter, and complexity maps have been quantified as shown in Figs. 5D-F. Figs. 5G-I show the results by overlying the quantitative maps onto binary vessel area map. It can be observed from the quantitative maps that the regions of capillary flow impairment are often associated with an increase of vessel diameter and a decrease in vessel area density and vessel complexity, which agrees well with clinical features observed from DR patients. Specific quantitative results are shown in Table 1.

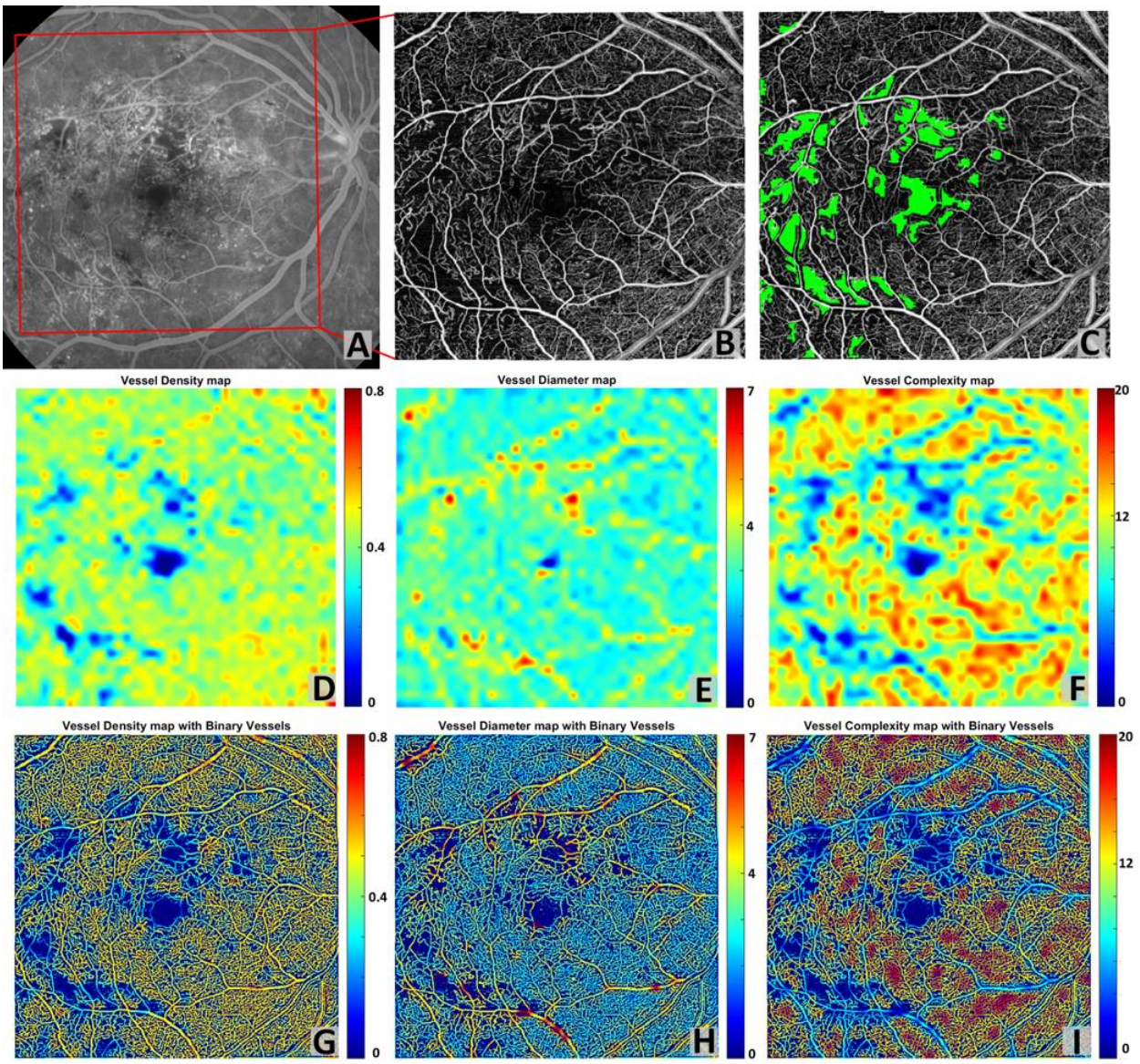


Figure 2.5. Quantitative OMAG on a NPDR case.

(A) FA image. (B) Whole retina OMAG image, correspond to the red rectangular region in the FA image. Scanning area is 6.72 mm × 6.72 mm. (C) Flow impairment zone quantification. Capillary drop out region was detected from vessel skeleton image and presented in green color, superimposed on (B). (D) Vessel density map. (E) Vessel diameter map. (F) Vessel complexity map. (G-I) Integration of quantitative maps (D-F) with binary vessel area map.

Table 2.1. Quantitative analysis of a Normal case and a NPDR case.

| Indices | Vessel Diameter Index | Vessel Area Density | Vessel Skeleton Density | Vessel Perimeter Index | Vessel Complexity Index | Flow Impairment Zone ($mm^2$) |
|---|---|---|---|---|---|---|
| Normal | 24.421 | 0.518 | 0.146 | 0.349 | 17838.540 | 0.264 |
| DR | 24.665 | 0.370 | 0.101 | 0.245 | 12954.770 | 3.450 |

### 2.3.3 *Repeatability of quantitative OMAG*

Figure 2. 6 shows a side-by-side comparison of two scans from the same subject diagnosed with BRVO, but scanned at time points one month apart. This case was clinically diagnosed as stable over the time period as judged by fundus examination, FA and visual acuity. OMAG results demonstrated that the detailed characteristics of BRVO such as vascular dilation and capillary non-perfusion are repeatable between these two scans. Quantitative maps (Figure 2. 6 G-L) also show great repeatability, where the increase in vessel diameter and decrease in vessel density and vessel complexity are present in regions of the vein occlusion in both scans. VAD, VSD, VDI, VPI and VCI have also been quantified on two scans. Results show high repeatability as the coefficients of variance are all smaller than 0.031 (Table 2). In doing so, each map was resized to 100 superpixels and repeatability between different scans was quantified based on these 100 samples.

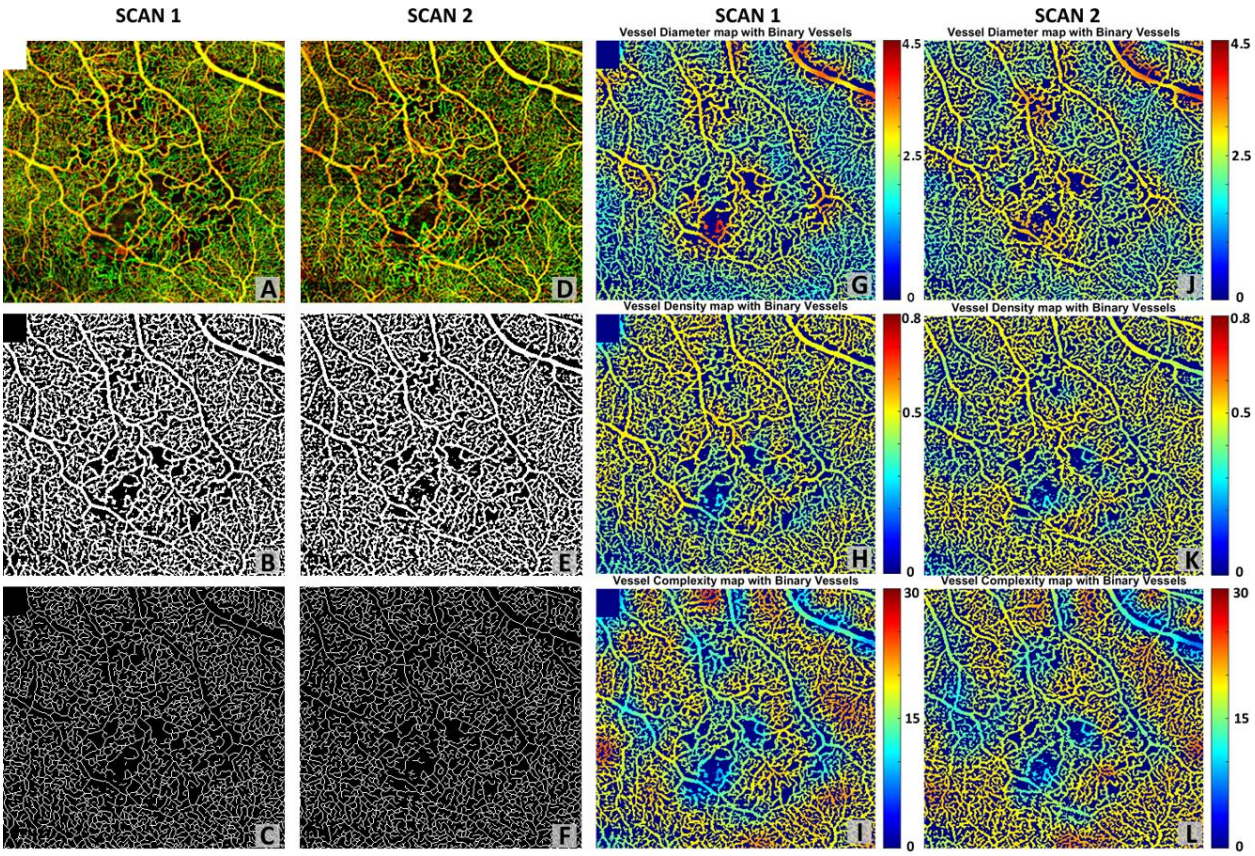


Figure 2.6. Quantitative OMAG analysis of a BRVO case with repeated scans. (A, D) OMAG image of occluded region, covering a FoV of 4.3 mm × 4.6 mm. (B, E) Vessel area map. (C, F) Vessel skeleton map. (G, J) Vessel density map integrated with vessel area map. (H, K) Vessel diameter map integrated with vessel area map. (I, L) Vessel complexity map integrated with vessel area map.

Table 2.2. Quantitative analysis and repeatability test of a BRVO case for two repeated scans.

| | Vessel Diameter Index | Vessel Area Density | Vessel Skeleton Density | Vessel Perimeter Index | Vessel Complexity Index |
|---|---|---|---|---|---|
| Scan 1 | 35.300 | 0.449 | 0.175 | 0.395 | 2862.719 |
| Scan 2 | 34.196 | 0.451 | 0.182 | 0.393 | 2827.102 |

Similarly, two repeated scans of a normal subject (Figure 2. 7) show great repeatability of not only the OMAG *en face* images, but also three quantitative maps. Coefficients of variance have also been quantified for five quantitative indices and all are no greater than 0.021 (Table 3). Therefore, our OCTA quantification algorithm should be useful for monitoring disease progression and treatment response.

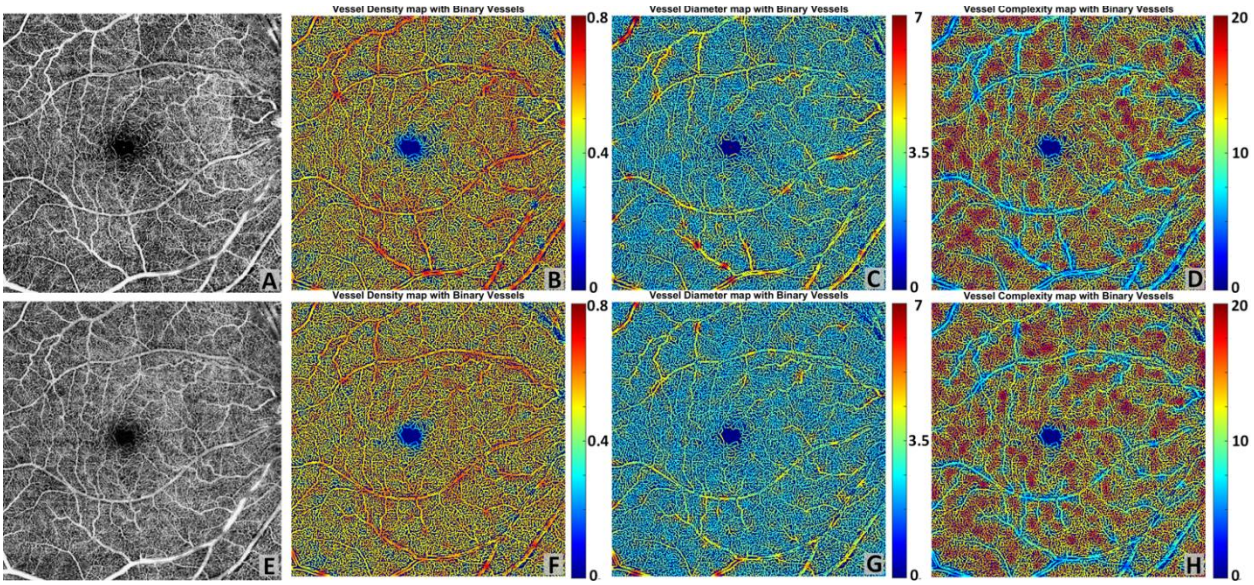


Figure 2.7. Repeatability of Quantitative OMAG on a normal case.

(A) Whole retina OMAG image of a normal case, covering an area of 6.72 mm × 6.72 mm. (E) Repeated scan of the same subject at same location, whole retina OMAG image. (B, F) Vessel density map integrated with the binary vessel area map. (C, G) Vessel diameter map integrated with the binary vessel area map. (D, H) Vessel complexity map integrated with the binary vessel area map.

Table 2.3. Repeatability test of a normal case.

| | Vessel Diameter Index | Vessel Area Density | Vessel Skeleton Density | Vessel Perimeter Index | Vessel Complexity Index |
|---|---|---|---|---|---|

| | | | | | |
|---|---|---|---|---|---|
| Scan 1 | 23.206 | 0.511 | 0.151 | 0.353 | 19282.771 |
| Scan 2 | 23.619 | 0.512 | 0.149 | 0.351 | 18979.230 |
| Coefficient of Variance | 0.018 | 0.009 | 0.021 | 0.011 | 0.017 |

Moreover, we have implemented this algorithm in a software package where the operator can flexibly select their regions of interest on the *en face* image with the following options of e.g., a rectangle, circle, ring, or ellipse. Figure 2. 8 shows an example of our ROI selection, Figure 2. 8A is the original OMAG *en face* image, Figure 2. 8B shows the quadratic analysis with a ring ROI and Figure 2. 8C-F shows the circle, rectangle, ellipse and circle ROI selection respectively. Table 4 shows the specific quantitative values when different ROIs are selected. If the selection is a ring, it can divided into four quadrants to enable quadrant specific quantification. Table 5 shows results of quadratic analysis of this BRVO case. Noted that in the scans centered at fovea, the operator can choose to center their ring ROI at the fovea centralis.

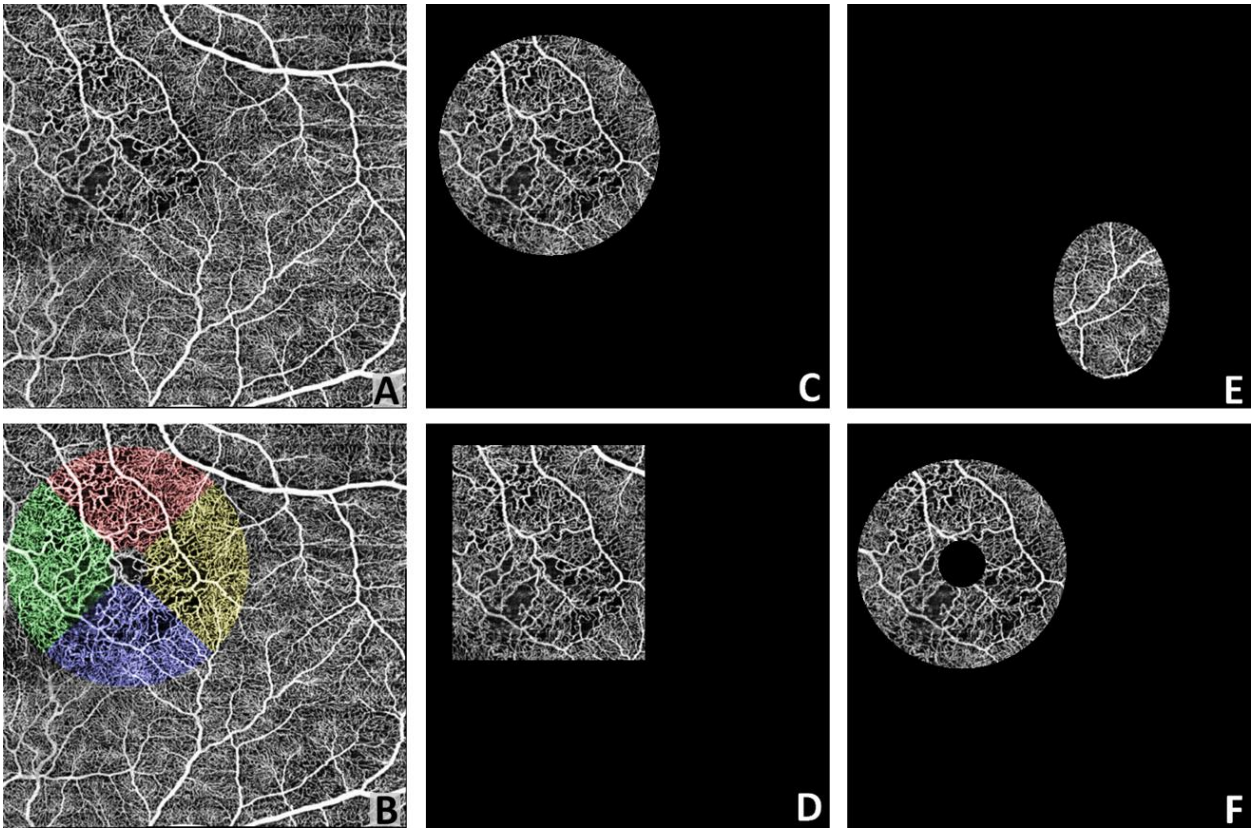


Figure 2.8. Illustration of region of interest selection.

An original OCTA image with a FOV of 6.72 mm × 6.72 mm. B Illustration of quadratic analysis. Red represents superior quadrant, green represents nasal quadrant, blue represents in inferior quadrant and yellow represents temporal quadrant. C ROI selection example of a circle. D ROI selection example of a rectangle. E ROI selection example of an ellipse. F ROI selection example of a circle.

Table 2.4. Quantitative analysis of a BRVO case with different choice of region of interest.

| | Vessel Area Density | Vessel Skeleton Density | Vessel Perimeter Index | Vessel Diameter Index | Vessel Complexity Index | ROI Size (mm*mm) |
|---|---|---|---|---|---|---|
| Whole Image | 0.493 | 0.200 | 0.419 | 32.554 | 7234.772 | 44.890 |
| Circle | 0.491 | 0.195 | 0.418 | 33.272 | 396.946 | 10.521 |

| | | | | | | |
|---|---|---|---|---|---|---|
| Rectangle | 0.491 | 0.193 | 0.415 | 33.633 | 457.660 | 11.389 |
| Ellipse | 0.519 | 0.220 | 0.454 | 31.28575 | 62.690 | 3.964 |
| Ring | 0.494 | 0.193 | 0.416 | 33.812 | 285.845 | 8.987 |

Table 2.5. Quadratic quantitative analysis of a BRVO case.

| | Vessel Area Density | Vessel Skeleton Density | Vessel Perimeter Index | Vessel Diameter Index | Vessel Complexity Index | ROI Size (mm*mm) |
|---|---|---|---|---|---|---|
| Superior | 0.493 | 0.197 | 0.411 | 33.942 | 239.2756 | 6.0934 |
| Inferior | 0.473 | 0.202 | 0.424 | 32.034 | 257.6289 | 6.0934 |
| Nasal | 0.478 | 0.200 | 0.424 | 32.838 | 251.9077 | 6.0934 |
| Temporal | 0.489 | 0.194 | 0.413 | 34.292 | 237.8684 | 6.0934 |
| Whole Image | 0.493 | 0.200 | 0.419 | 32.554 | 7234.772 | 44.890 |

### 2.3.4 *Vascular dilation in macular telangiectasia type 2*

Figure 2. 9 shows an example of an early stage MacTel2 case, where the FA image (Figure 2. 9A) shows the signature juxtafoveal leakage that is more prominent temporally than nasally. The *en face* OMAG image and quantitative maps are given for the entire retina and deep capillary plexus in Figure 2.s 9B-E and 9F-I, respectively. The vessel diameter map and vessel complexity map demonstrate good accordance with the dye leakage on FA, and all demonstrate the telangiectatic changes in the microvasculature. With the dilation of the juxtafoveal microvasculature, local vessel diameter increases and the local vessel complexity decreases significantly, when compared to the relatively normal regions. The comparison between the entire retinal vasculature and deep capillary plexus also validates that the early telangiectatic

changes mainly happen in deep capillary plexus [36] as the quantitative maps manifest more obvious changes. With the segmentation strategy and high resolution OMAG images, a detailed depiction of the deep retinal microvasculature can be produced, as shown in Figure 2.s 9G-I, which cannot be achieved using traditional FA. Good correlations can be observed between the leaking regions on FA and the abnormal regions on the vessel diameter map and the vessel complexity map on the OMAG images. This observation maybe clinically important because if true, then quantitative OMAG may present the ability not only to detect the same vascular abnormalities as FA, but also to provide information about the areas of potential leakage without the need for FA. Additional patients are needed to validate this observation.

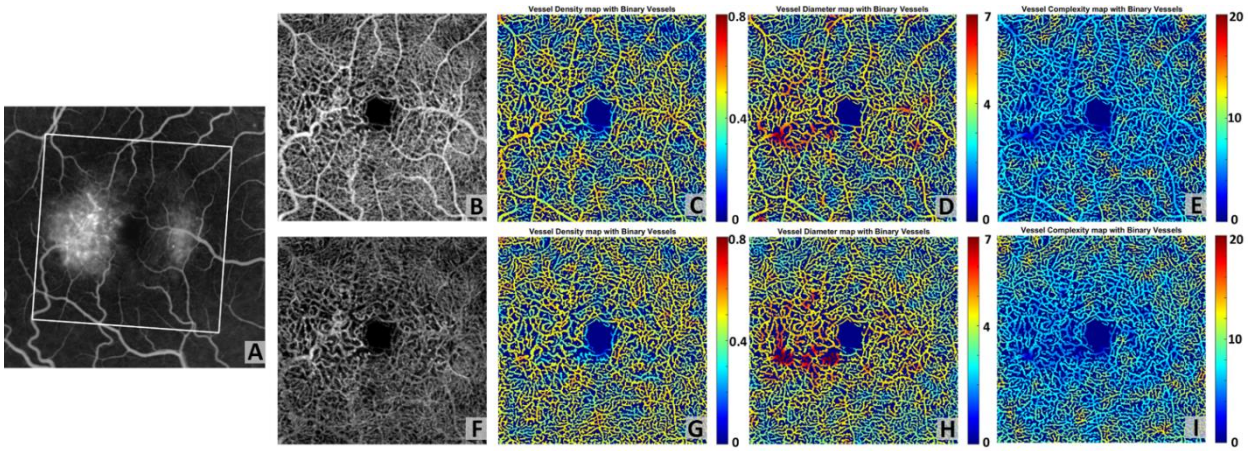


Figure 2.9. Quantitative OMAG analysis of a MacTel2 case.

(A) FA image of the MacTel2 subject. (B) SS-OCT OMAG image of the whole retina, covering 3 mm × 3 mm area, corresponding to the white rectangular region in FA image. (C) Vessel density map integrated with vessel area map on the whole retina. (D) Vessel diameter map integrated with vessel area map on the whole retina. (E) Vessel complexity map integrated with vessel area map on the whole retina. (F) OMAG image of the deep capillary plexus. (G) Vessel density map integrated with vessel area map of the deep capillary plexus. (D) Vessel diameter map integrated with vessel area map of the deep capillary plexus. (E) Vessel complexity map integrated with vessel area map of the deep capillary plexus.

Figure 2. 10 shows the side-by-side comparison of a normal subject and the MacTel2 subject. Subtle differences can be noticed in the vessel density maps as the MacTel2 case shows a lower global vessel area density. Distinct differences can be found on both vessel diameter maps and vessel complexity maps. The MacTel2 case also shows a significantly increased value in the juxtafoveal temporal and nasal regions on the vessel diameter map when compared with the normal case and an extensively decreased vessel complexity value when compared with the normal eye in the same regions of interest.

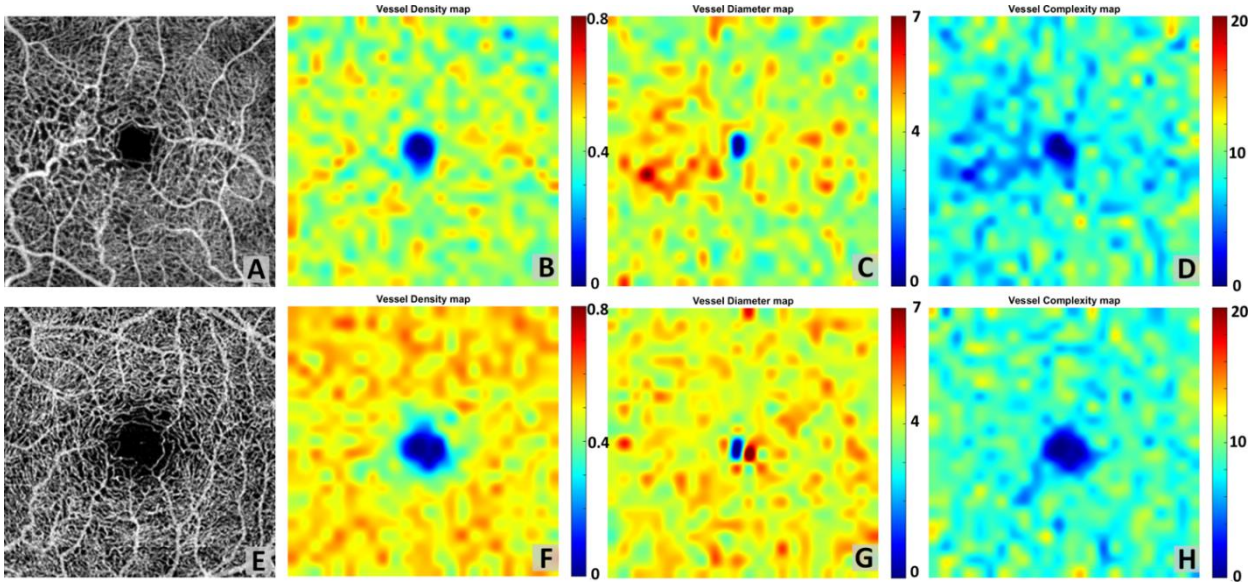


Figure 2.10. Quantitative OMAG comparison between the MacTel2 and normal cases. (A) 3 mm × 3 mm OMAG image of the whole retina of a MacTel2 subject. (B) Vessel density map. (C) Vessel diameter map. (D) Vessel complexity map. (E) 3 mm × 3 mm OMAG image of the whole retina of a normal subject. (F) Vessel density map. (G) Vessel diameter map. (H) Vessel complexity map.

Moreover, our five-index quantitative analysis may be useful in the treatment monitoring. Figure 2. 11 shows results from a patient who received monthly injections of a vascular endothelial growth factor (VEGF) inhibitor from January 2015 to March 2015. OCTA scans

were performed at each visit with the first scan before treatment and the subsequent two scans performed one month after each treatment. OCTA volume data were segmented into superficial retinal layer, deep retinal layer, and outer retinal layer. *En face* images were generated for each layer using maximum projection for all three scans. A1-C1 are the superficial retinal layer, deep retinal layer, and outer retinal layer OCT angiograms, respectively, for the first visit before treatment; A2-C2 are for the second visit one month after the first treatment; and A3-C3 are for the third visit one month after the second treatment. For each visit, the deep retinal layer angiograms were chosen for the quantification of vessel density maps, vessel diameter maps, and vessel complexity maps, which are shown in D1-D3, E1-E3 and F1-F3, respectively. By observing these quantitative maps after the first injection, we found that the VDI decreased between the first and second visits, and the VCI has increased. In order to test whether our quantitative analysis has the ability to monitor the changes in vascular abnormalities after treatment, we performed quadrant-specific statistical analysis on this case for all three visits. A 2-mm circle was selected for statistical analysis as showed in Figure 2. 12, and superior, inferior, temporal and nasal quadrants are labeled in different colors. In each quadrants, all data points were equally divided into ten subsets and the averaged values were used to represent each subsets. Therefore, we have ten samples of each quantitative index for each quadrants. The averaged value of each quadrants for each index are shown in Table 6. ANOVA was performed and the VDI showed significant decrease in superior, temporal and inferior quadrants after treatment while VCI were found significantly increased in temporal and inferior quadrants after treatment. No significant differences were found in any quadrants for VAD, VSD or VPI. FA was only performed at the first visit therefore we do not have all three corresponding FA images to compare with OCTA images. While these results are intriguing, a larger study is clearly

needed to fully validate the usefulness of our quantitative analysis for monitoring treatment response after anti-VEGF therapy.

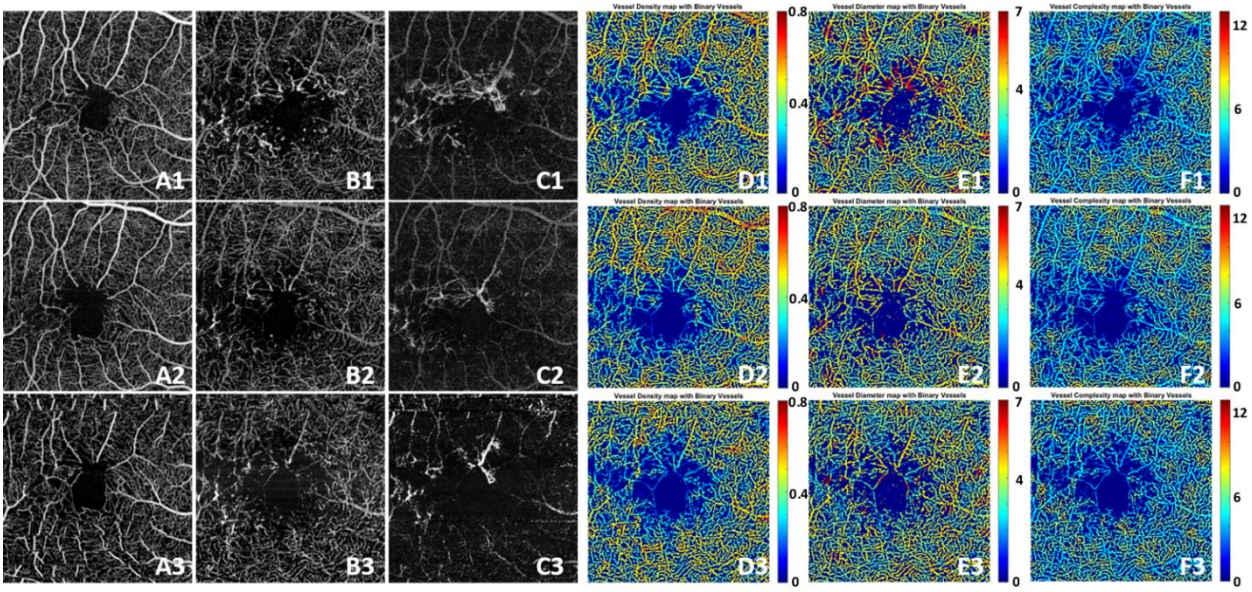


Figure 2.11. Three OCTA scans of a patient with MacTel2 monthly apart.

A1-A3 shows the superficial retina for the first, second and third scans respectively. B1-B3 shows the deep retina for three scans respectively. C1-C3 shows the outer retina for three scans respectively. D1-D3 shows the vessel density map for three scans respectively and E1-E3 shows the vessel diameter maps for three visits while F1-F3 shows the vessel complexity maps for all three visits.

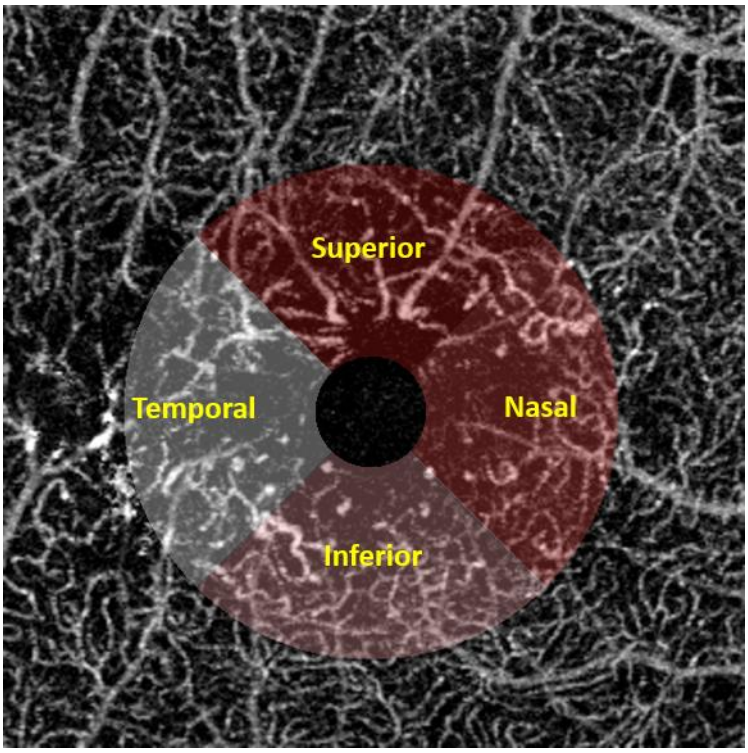


Figure 2.12. Illustration of the quadratic analysis.
2mm circle is selected excluding the FAZ. Superior, inferior, temporal and nasal quadrants are labeled in different colors as showed in text.

Table 2.6. Quantitative analysis of a MacTel2 case receiving anti-VEGF treatment.

| Indices | Quadrant | 1/9/2015 | 2/5/2015 | 3/31/2015 |
|---|---|---|---|---|
| Vessel Diameter Index | Superior* | 21.397 | 19.704 | 18.995 |
| | Temporal* | 20.228 | 18.857 | 18.063 |
| | Inferior* | 19.901 | 19.082 | 18.268 |
| | Nasal | 19.441 | 18.916 | 19.228 |
| Vessel Area Density | Superior | 0.391 | 0.368 | 0.341 |
| | Temporal | 0.364 | 0.322 | 0.340 |
| | Inferior | 0.401 | 0.378 | 0.395 |
| | Nasal | 0.388 | 0.374 | 0.361 |

| | | | | |
|---|---|---|---|---|
| Vessel Complexity Index | Superior | 4.615 | 4.952 | 4.852 |
| | Temporal* | 4.840 | 4.726 | 5.307 |
| | Inferior* | 5.313 | 5.378 | 5.830 |
| | Nasal | 5.112 | 5.371 | 5.329 |
| Vessel Skeleton Density | Superior | 0.097 | 0.095 | 0.092 |
| | Temporal | 0.092 | 0.086 | 0.096 |
| | Inferior | 0.105 | 0.103 | 0.107 |
| | Nasal | 0.097 | 0.098 | 0.094 |
| Vessel Perimeter Index | Superior | 0.225 | 0.221 | 0.213 |
| | Temporal | 0.236 | 0.221 | 0.241 |
| | Inferior | 0.264 | 0.257 | 0.271 |
| | Nasal | 0.250 | 0.254 | 0.248 |

* indicates $p<0.05$ in ANOVA test

### 2.3.5 *Building database for normal subjects*

Looking forward, we are in the process of building a normal OCTA database for quantification. We have currently enrolled five normal subjects (age matched) and obtained 6.72 mm × 6.72 mm montage OCTA scans from each of them. OMAG en face images have been produced and used for quantification. Descriptive statistics of normal subjects are shown in Table 7. With the establishment of a normal database, future studies that compare diseased cases with normal cases or that determine disease progression or classification would be feasible.

Table 2.7. Statistics of quantitative indices for normal subjects.

| | Mean | Standard Deviation | Lower 95% | Upper 95% |
|---|---|---|---|---|
| Vessel Diameter Index | 24.073 | 0.640 | 23.454 | 25.036 |
| Vessel Area Density | 0.505 | 0.010 | 0.493 | 0.518 |
| Vessel Skeleton Density | 0.143 | 0.004 | 0.138 | 0.149 |
| Vessel Perimeter Index | 0.339 | 0.004 | 0.329 | 0.349 |
| Vessel Complexity Index | 17962 | 591 | 17228 | 18696 |

## 2.4 DISCUSSION

In this report, we proposed five metrics, VAD, VSD, VDI, VPI and VCI, for the quantitative assessment of OCT angiograms. There are several important features in our analytical approach. First, the quantitative OCTA analysis using the five metrics is highly repeatable as the repeatability study on the BRVO and normal cases showed coefficients of variance smaller than 0.031, suggesting that the quantitative assessment at follow-up and when used for therapeutic monitoring should provide a high level of accuracy when using OCTA. Second, the quantitative metrics are useful to provide clinicians and physicians with a rapid and comprehensive strategy for interpreting OCT angiograms. Unlike previous studies that only provided a single quantitative index such as vessel area density or skeleton density, our proposed quantitative analysis includes five indices, e.g. VAD, VSD, VDI, VPI and VCI. Along with three quantitative maps, the vessel density map, the vessel diameter map and the vessel complexity

map, the information about vascular abnormalities could be visualized and extracted from OCTA images based on multiple perspectives. Vessel length, size, area, perimeter, and morphological complexity can be all made available in one step of image analysis, potentially helping clinicians understand OCTA images better. For example, in the case that we studied here, the five metrics showed its promise to distinguish BRVO from NPDR. Both of these two cases demonstrate VAD decrease. However, for NPDR, the decrease of vessel area density is dominated by skeleton decline; whereas for NPDR, both VDI and VSD are increased. Third, the quantitative metrics can provide additional information when presented alongside with the qualitative OCTA images.

One commonly acknowledged shortcoming of OCTA is that it is difficult to show hyperpermeability or leakage from abnormal vasculature as seen with FA. This difference between OCTA and FA originates from the fact that OCTA detects the movement of RBCs while FA detects the presence and leakage of a small molecular weight dye that remains mostly unbound to protein and capable of diffusing out from abnormal vessels. Though fluorescein leakage registers as an important marker of a vascular abnormality, it also prevents detailed visualization of microvasculature. In this study, we showed that with our quantitative maps, OMAG might also detect the regions of abnormal microvasculature that might correspond to areas of dye leakage on FA images. This abnormal vasculature possesses many abnormal characteristics that are probably associated with increased permeability, such as vascular dilation, a decrease of vascular complexity, and capillary drop out. While it is the current dogma that OCTA is not able to detect vascular hyper-permeability, this lack of leakage detection may be mitigated to some extent by our quantitative analysis because our results suggest that the regions of vascular dilation or decreasing complexity correlate well with leakages on FA.

However, this finding is based on a limited number clinical cases. Clearly, additional studies with larger sample sizes are needed to confirm this finding.

Moreover, our quantitative analysis is versatile in terms of selecting the region of interests (ROI). In this study, the analysis was reported on the entire image. Our algorithm also allows users to freely select only part of the OCT angiograms as a region of interest with a variety of useful choices, such as rectangle, circle, ring or ellipse regions as shown in Figure 2. 8. This feature may be useful when user wants to compare the same ROI of different scans as the scanned regions might vary. Furthermore, we have also demonstrated the software's ability in conducting quadratic analysis in both a BRVO case and a MacTel2 case. Even though previous studies have shown the quantification of vessel density in normal and DR human subjects [29, 30], to the best of our knowledge, this is the first study that vessel diameter and vessel complexity have been quantified on OCTA images with capillary level resolution. Our three quantitative maps together are useful for providing an integrated analysis on various ocular diseases. In addition, it should also be possible to combine all our quantitative maps together to yield an integrated 'vascular abnormality indicator map'. In order to do so, we would need to complete the normal database, upon which to combine the vessel density map, vessel diameter map and vessel complexity map together, with appropriate weighting factors if necessary, to serve as a quick indicator to locate a region of vascular abnormality from patients' scans.

There are several limitations in our quantitative OMAG technology. First, the OCTA data shows projection artifacts in the deep retinal layers on both cross-sectional images and en face images. When photons interact with moving particles, the phase of the light wave changes as a result of the Doppler Effect. Therefore, when the light travels through blood vessels in living tissue, only part of the light would reflect back during its first interaction with RBCs while the

majority of the photons carry on that are influenced by their first interaction. As a result, OCTA signals in the deeper layers also carry the shadows of blood vessels from the superficial plexus. These projection artifacts from the retinal vasculature projected onto deeper layers of the retina are ubiquitous and difficult to notice unless the OCTA data is segmented into superficial and deep plexus and the superficial signals are removed from the deeper flow signals. The effects of the projection tails in retinal vasculature on quantitative analysis remain underexplored, but the inherent physical characteristics of these artifacts suggest that the effects should be consistent. As a consequence, we did not perform any correction on the projection tails in this study. Zhang et al [25] recently proposed a practical and automatic projection artifact removal algorithm, which has been demonstrated to successfully remove these projection artifacts efficiently for visualizing macular neovascularization. Work is currently in progress to incorporate this projection artifact removal algorithm into our quantification assessment in order to provide more accurate quantification of the retinal microvasculature in the deep retinal layers.

The second limitation of this study is the inherent trade-off between scanning time and sampling density that makes high resolution wide-field OCTA scans more time-consuming. Although there is also a single 6mm × 6mm scanning protocol available with a lower sampling spacing between adjacent A-scans, we chose the montage scan mode over the single scan mode because the montage scan provides a much higher sampling spacing (~10 μm) and would not lose detailed information of the microvasculature. Lastly, we have not performed a reproducibility study on different OCT systems with the same subject. Since some of our quantitative indices are pixel based values, the comparison of different images will require the same pixel size.

In conclusion, we have demonstrated a comprehensive quantitative OCTA analysis package for normal and diseased eyes. Collectively, the vessel area density, vessel skeleton density, vessel perimeter index, vessel diameter index, and vessel complexity index can detect abnormal microvasculature and also provide repeatable quantitative results. Our vessel density map, vessel diameter map, and vessel complexity map jointly could be useful for detecting regions with vascular abnormalities that could also leak fluorescein on FA images. Overall, quantitative OCTA has promising future applications in research and clinical management of ocular diseases.

# Chapter 3. COMPLEX SIGNAL-BASED OPTICAL COHERENCE TOMOGRAPHY ANGIOGRAPHY ENABLES IN VIVO VISUALIZATION OF CHORIOCAPILLARIS IN HUMAN CHOROID

## 3.1 INTRODUCTION

The choroid, located between the sclera and retinal pigment epithelium (RPE), is a thin layer consisting predominantly of blood vessels, highly pigmented melanocytes, nerves, and connective tissue. The choroid not only provides blood flow and nutrients to the outer retina, including the photoreceptors, but also is important for the metabolic exchange within the foveal avascular zone. Not surprisingly, changes in choroidal circulation are associated with several ocular diseases, such as age-related macular degeneration (AMD) [37, 38], uveitis [39], diabetic retinopathy (DR) [40], and central serous chorioretinopathy (CSC) [41]. The choriocapillaris (CC) [42-44], located along the inner portion of the choroid, is a thin, but dense, planar capillary bed that is composed of polygonal vascular units called lobules. The CC is supplied by the feeding arterioles of the deeper choroid, which enter perpendicularly with round open connecting points, and is drained by venules, which are orientated circumferentially around the lobules. Histopathological studies [45-47] have shown that abnormalities or absence of the CC have been associated with the loss of RPE in geographic atrophy (GA) and drusen formation, and these changes in the CC may contribute to the formation of macular neovascularization [46]. Additionally, eyes with DR were found to have a reduced vessel density within the CC when compared with eyes from healthy subjects [40, 48]. However, a high resolution *in vivo* method to visualize the structural and blood flow changes occurring within the CC is needed to better understand the role of the CC in the pathophysiology of these ocular diseases.

Clinically, fluorescein angiography (FA) and indocyanine green angiography (ICGA) have been the gold standards for evaluating the blood flow characteristics of the retina and choroid, but high resolution imaging of the CC with either methods has not been possible [49-51]. Optical coherence tomography (OCT)-based angiography (OCTA) [25, 52-54] is another approach being introduced for *in vivo* three-dimensional (3D) imaging of the CC that does not require the injection of dye. There are multiple variations of OCTA, all of which utilize the phase [55], amplitude [56, 57], or a combination of both the phase and amplitude [26] of the OCT signal to obtain flow data.

As exciting as this technique may be, however, imaging of the CC using OCTA has not been without its challenges. The first issue hindering the study of the CC by OCTA is the fact that it is located under the RPE where a large number of photons get scattered. This subsequently results in the CC signal buried within a large and stochastically scattering background. The second issue is that the CC is a densely vascularized layer, where vessel diameter averages 5 – 20 μm with relatively slow flow speeds of 0.2 – 2 mm/s [58, 59]. Therefore, both high signal-to-noise ratio (SNR) and high flow speed sensitivity are needed in order to successfully image the CC. One strategy to visualize the CC is to combine OCTA with adaptive optics [54, 60-63]. Kurokawa et al. obtained relatively high-resolution images using this combined technique; however, the images were captured through a limited field of view (FoV), typically of <500 x 500 $\mu m^2$. In another paper by Kurokawa et al., adaptive optics was used in combination with the phase information from the OCT signal to successfully image the CC in the macular region of healthy individuals, but this approach also was hindered by a limited FoV (0.65 x 0.33 $mm^2$ ~1.3 x 1.3 degrees) and less-than-ideal acquisition speeds (91 kHz A-line rate) [61]. Braaf et al., again utilizing phase information, installed a second scanning laser ophthalmoscope as the hardware

tracking system and imaged the CC under the fovea of healthy subjects [64]. Utilizing a different approach that utilizes amplitude information, Choi et al. used speckle decorrelation to contrast the CC from the large vessels of the choroid with an in-house built 400 kHz swept source-OCT (SS-OCT) system. However, this specialized laboratory-based system is not accessible by the ophthalmic community [63].

The ability to use of OCTA alone for imaging the CC may lay with optical micro-angiography (OMAG), which is an algorithm previously developed to provide higher sensitivity to slow blood flows compared with other algorithms that uses amplitude or phase information alone to detect blood flow. OMAG has been used for several years to image vascular networks [25, 53, 65-68], and its complex signal-based approach is especially suitable for contrasting capillaries with slow flow velocity, such as the CC. To determine the best decorrelation algorithm for the detection of the CC with its slow flow velocities, we investigated and refined CC imaging and visualization *in vivo* with the use of a commercially available spectral domain-OCT (SD-OCT) system and different OCTA algorithms.

## 3.2 Materials and Methods

### 3.3.1 *OCT system and scanning protocols*

In this study, we chose to use a commercially available OCTA system so that the proposed approach could be accessible by the wider community. In particular, a SD-OCT Cirrus HD 5000 research prototype system, a precursor of the AngioPlex® system (Carl Zeiss Meditec Inc., Dublin, CA, USA) was used to capture the OCTA images from the subjects. The system provided an A-scan imaging speed of 68 kHz with the central wavelength at 840 nm and a bandwidth of 50nm. The axial resolution was ~5 μm while lateral resolution was ~15 μm,

estimated at the fundus surface. With the FastTrac™ motion correction software, this SD-OCT also provided a prototype function: a montaging scanning protocol in addition to the regular 3mm x 3mm and 6mm x 6mm scanning options. In the montage scanning protocol, wide field imaging can be achieved by stitching together smaller image cubes (each cube with a FoV of 2.4mm x 2.4mm in this study). Each cube was acquired with 245 A-scans in the fast scan axis (B-scan) and 245 transverse locations in the slow scan axis (C-scan). A 10% overlap in the scanning area between adjacent cubes was achieved for post-scan montaging of images. With this setup, we acquired 9 mm x 11 mm FoV images from 20 cubes for each healthy individual, centered at the fovea. Scanning was performed in a dark room without pupil dilation. To contrast the moving red blood cells (RBC), four repeated B-scans were acquired at each transverse location before moving to the next transverse location. One cube (volume) scan took ~3.5 s to produce.

Five volunteer subjects without known ocular conditions (aged from 25 to 56 yrs with a mean of 38.2 ± 15.5, 4 females and 1 male) participated in this study. This study was conducted in accordance with a protocol approved by the Institutional Review Board of the University of Washington and informed consent was obtained from all subjects. The study followed the tenets of the Declaration of Helsinki and was conducted in compliance with the Health Insurance Portability and Accountability Act.

### 3.3.2 *Choriocapillaris angiography*

When the OCT beam passes through vascularized biological tissues, it interacts with the RBCs flowing through the blood vessels, resulting in photons being transmitted or scattered. During this process, the velocity of the photons will change, as will their direction of travel; thus, introducing a phase change in the light waves. In addition to the phase change, the number of

photons interacting with the moving RBCs alters the amplitude of the OCT signal. Based on these observations, OMAG measures flow signals using both the phase and amplitude aspects of the complex, i.e. coherent, OCT signal.

This concept is better illustrated in Figure 3. 1. For each voxel in 3D OCT data, the signal comes from the summation of photons backscattered from the focal spot (Fig. 1 (a)). The static tissue signal is represented by the solid black vector in the complex coordinates (Fig. 1 (b)), and is derived from the first B-scan of the repeated B-frame cluster. After a given time interval, the second B-frame is obtained, and the OCT signal from the same focal spot is presented as the dashed dot vectors, assuming there is movement in this voxel (round dot vectors in Fig. 1 (b)). The detectable movement range is represented by the long-dashed circle. It should be noted that the movement range would not be a perfect ring, as the sensitivity for phase and amplitude differences would differ. It would also vary between OCT systems. For the purpose of simplicity, however, it is exemplified as a two dimensional circle here while it is actually an irregular three dimensional shape in reality. The noise floor is illustrated as a gray dashed circle.

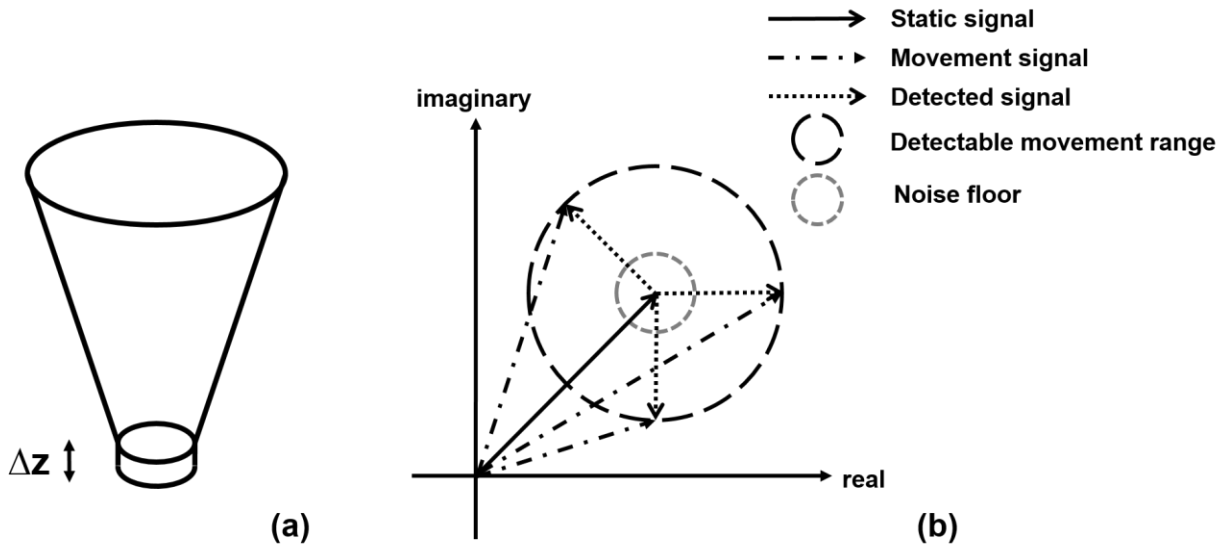


Figure 3.1. Illustration of the OCT signal.

(a) The focal spot of OCT on tissue. (b) The OCT signal represented in complex coordinates.

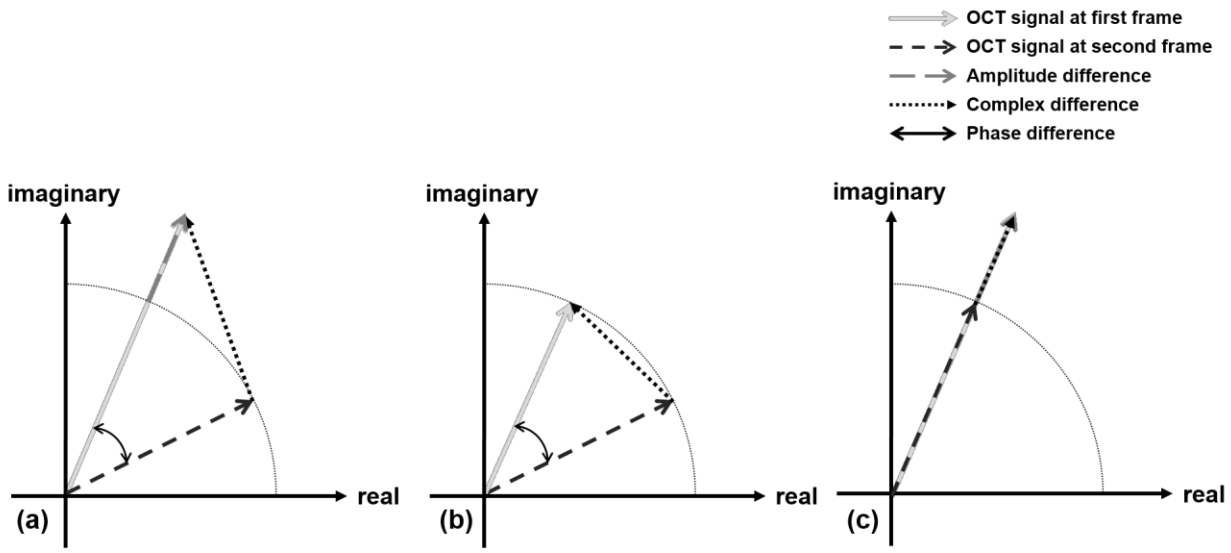


Figure 3.2. Schematic comparison of the phase, amplitude, and complex signal-based approaches.

The diagram present OCT signals captured at the same location within the same a time interval, illustrating different scenarios when a moving particle interacts with the OCT beam for comparing the phase, amplitude, and complex signal-based approaches. (a) typical cases when particle interacts the OCT beam. (b) a special case when the particle moves parallel to the OCT beam. (c) a special case when the particle moves perpendicular to the OCT beam.

As shown in Figure 3. 2, those detectable movement vectors could be categorized into different scenarios. In Figure 3. 2 (a), the phase, amplitude, and complex signal-based differences are illustrated as two headed black arrow, gray dash arrow, and black dot arrow, respectively. In this case, all three approaches, i.e. phase, amplitude and complex, can detect the motion signal, and would be the most common case in real world settings; however, compared to the amplitude approach, the complex approach will result in larger signal differences between two frames, as dictated by the law of triangle inequality. More extreme scenarios are illustrated in (b) and (c). In case (b), the amplitude of both signals is the same but the phase has changed, which would occur when the probe beam is parallel to the blood vessel orientation, for example in the retinal angiomatous proliferation lesion where the anastomotic vessel often runs

perpendicularly from retina to choroid. In case (c), the amplitude has changed, which would occur when the probe beam is perpendicular to the vessel orientation. Realistically, scenarios (b) and (c) seldom exist; however, they do showcase two tendencies for case (a) where the real amplitude or phase differences could be buried under the noise floor.

To clarify, the OCT signal from the first scan can be written as $A_1 e^{-i\varphi_1}$, and the OCT signal from the second can be written as $A_2 e^{-i\varphi_2}$. The OCTA result from the complex approach can be written as:

$$\left|A_1 e^{-i\varphi_1} - A_2 e^{-i\varphi_2}\right| = \sqrt{A_1^2 + A_2^2 - 2A_1 A_2 cos(\Delta\varphi)} \quad (6)$$

When the OMAG signal is normalized to the structural OCT signal, it can be re-written as:

$$\sqrt{\frac{(A_1 - A_2)^2}{A_1^2 + A_2^2} + \frac{2A_1 A_2}{A_1^2 + A_2^2}\left(1 - cos(\Delta\varphi)\right)} \quad (7)$$

where $(A_1 - A_2)^2/(A_1^2 + A_2^2)$ represents the amplitude difference approach (being one of the speckle variants), and the 2nd term in Eq.(2) represents the complex amplitude decorrelations (similar to phase variance approach). Therefore, OMAG takes both the intensity variance and complex decorrelation into consideration and employs all possible motion contrast mechanisms from OCT signals. On the other hand, the phase OCTA [55] and intensity OCTA [56, 57] approaches, when used separately, only detect part of the whole motion signal and fail to utilize all the available information. In the interest of obtaining the entirety of the motion signal, the complex signal-based OCTA approach, i.e. OMAG, was used in this study. OMAG measures the differences between 4 consecutive B-scans by simply subtracting complex signals from those repeated B-scans at the same location [26]:

$$F_{OMAG}(x,z) = \frac{1}{R}\sum_{n=1}^{R-1}|I_{n+1}(x,z) - I_n(x,z)| \quad (8)$$

where $I = Ae^{-i\varphi}$ is the complex OCT signal, *R* is the number of repeated B-scans at one transverse location, *n* is the index of repeated B-scans, and (x, z) correspond to the pixel coordinates in a signal B-scan. Considering that CC is a highly dense vascular layer, SNR is crucial for visualizing the vascular network with an improved contrast between moving RBCs and static tissues. The high scattering property of RPE would make the incoming probing photons heavily scattered before reaching the CC. Such scattering photons would raise the noise floor in the OCTA image of the CC. Because this noise caused by the photon scattering is stochastic in nature, it would be possible to enhance the CC image quality by performing more averaging. Based on this concept, we propose to use combined arithmetic and geometric means (AM and GM) to further enhance the contrast and SNR in the generated CC flow signal:

$$F'_{OMAG}(x,z) = \frac{1}{2}\left[\frac{1}{R}\sum_{n=1}^{R-1}|I_{n+1}(x,z)-I_n(x,z)| + \sqrt[3]{\prod_{n=1}^{R-1}|I_{n+1}(x,z)-I_n(x,z)|}\right] \quad (9)$$

In the Cirrus AngioPlex system used for this study, one A-scan has 1024 pixels corresponding to a scanning range of ~3 mm in air, giving a pixel size of ~2.2 μm in tissue (assuming the refractive index of retinal tissue is 1.35). There are 245 A-scans per B-frame and 245 B-frames correspond to 2.4 mm; thus, the pixel size on the transversal plane is ~7.3 μm in tissue. Because the lateral and axial resolutions were at ~15 μm and ~5.0 μm, respectively, the OCT image gives approximately 2x oversampling on the transversal plane and 2x oversampling in the axial direction. To obtain the CC, we first used a previously described semi-automatic segmentation software [32] to delineate the RPE in the structure image before applying the same segmentation to the blood flow image. By using the RPE as a reference to define CC slab boundaries, we can then choose between numerous layers of various thicknesses to visualize the CC or deeper regions of the choroid, if desired. In this study, CC slab was experimentally

visualized as a 10 – 20 μm thin layer under Bruch's membrane. The results of various locations and thicknesses are showed in later section.

With the contrast mechanism of OCTA relying on the different signals derived from the RBCs at multiple time points, the duration of the time intervals between these OCTA signals can play a significant role in the visualization of ocular vasculature. That is to say, the longer the time interval, the narrower the velocity range of visible blood vessels. This is within reason of course, as longer time intervals would naturally increase the scan time required per patient, which is not clinically desirable for ophthalmology. The idea of variable time intervals within OCT imaging was first introduced by Lei *et al*., who showed that variations in time intervals correspond with a detectable velocity range in Doppler OCT [69]. Similarly, in OCTA, if we increase the time interval, an increased number of blood vessels with slower velocities can be detected [70]. For this study, four consecutive B-scans were taken at the same location with a time interval of 4.5 ms. Similar to previously reported choroidal imaging studies [70], we also examined the effects of increasing inter scan time-interval by using the differences between frames 1 and 3, as well as frames 2 and 4; thus, increasing the time interval to 9 ms.

## 3.3 RESULTS

The OCT raw datasets were obtained from 5 subjects according to the OCTA protocol described in Section 2.1. In total, there were about 100 OCTA cube scans (~20 scans per subject, with no failed scans). The raw datasets were post-processed using algorithms described above to obtain the final OCTA results of the CC. Representative results are presented below.

The CC is a thin layer below the Bruch's membrane, only 10 – 20 μm in depth. Therefore, after proper segmentation of the RPE layer, the corresponding number of pixels was taken below the Bruch's membrane for *en face* visualization, as shown in Figure 3. 3. Figure 3. 3

(a) – (d) shows the CC from different depths below the Bruch's membrane, ranging from 2.2 to 17.6 µm. At the increasing depths, i.e. an 11 µm-thick region 20 µm under the Bruch's membrane (e), and an 11 µm-thick region 30 µm under the Bruch's membrane (f), larger choroidal vessels are visible. Interestingly, in contrast to large retinal vessels, deep choroidal vessels appear to be dark in OCT and OCTA images. The thickness of CC varies at different locations, thicker under the fovea and thinner peripherally, ranging from 10 µm ~ 20 µm [42, 43]. Among all subjects imaged in this study, a thicker slab (17.6 µm) was used for CC under the fovea (central 4 cubes under the fovea covering a 5mm x 5mm region) and a thinner slab (11 µm) was used for CC everywhere else. Both correct location and thickness of the CC slab are essential for optimal visualization of the CC with OCTA.

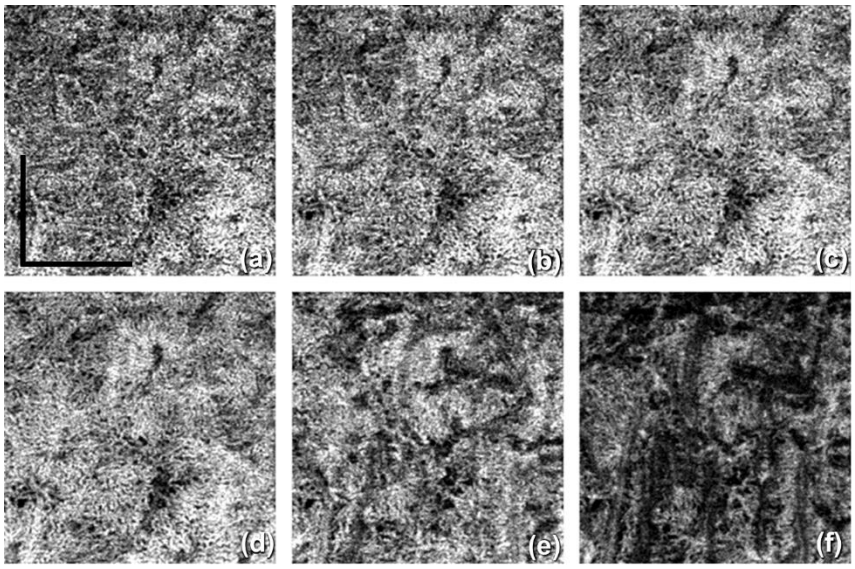


Figure 3.3 The visualization of CC obtained from OCTA projection from a slab with varied thicknesses measured below the Bruch's membrane along the z depth.

(a) A 2.2 µm thick slab under Bruch's membrane. (b) A 6.6 µm thick slab under Bruch's membrane. (c) A 11 µm thick slab under Bruch's membrane. (d) A 17.6 µm thick slab under Bruch's membrane. (e) A 11 µm thick slab, 20 µm under the Bruch's membrane. (f) A 11 µm thick slab, 30 µm under the Bruch's membrane. Scale bar = 1 mm.

Figure 3. 4 shows a comparison among all Pythagorean mean approaches. The phase OCTA images show the most differences given that the phase differences are generally more susceptible to noise and fluctuations compared to the amplitude signals. Harmonic mean approach is not optimal in visualizing vasculature in CC and was then not adopted. Compared to arithmetic mean approach, geometric mean algorithm provides clearer contrast in vascular patterns in phase OCTA images and almost no horizontal artifacts in structural OCT images. The main reason could be that geometric mean is always equal or smaller than arithmetic mean. When there is little bulk motion noise between different B scans, GM and AM would yield very similar results, but when large motion is present among repeated B-scans, GM would yield smaller values compared to AM, therefore smaller fluctuations in flow signal due to noise. When compared among phase OCTA images, it can be observed that GM algorithm shows clearer vascular patterns compared to AM while all the amplitude OCTA images appear similar. Moreover, using methods reported in [25], quantitative assessment of the image contrast and SNR was conducted between AM and GM approaches as shown in Table 1, where the complex approach is demonstrated with superior performance to that using either the amplitude or phase information alone. This assessment also indicates that if AM is combined with GM, further improvement in image contrast and SNR would result. Therefore, AM+GM approach was adopted for further comparisons and study of CC OCTA in an attempt to boost SNR through more averaging and suppressing motion artifacts, i.e. Eq.(4).

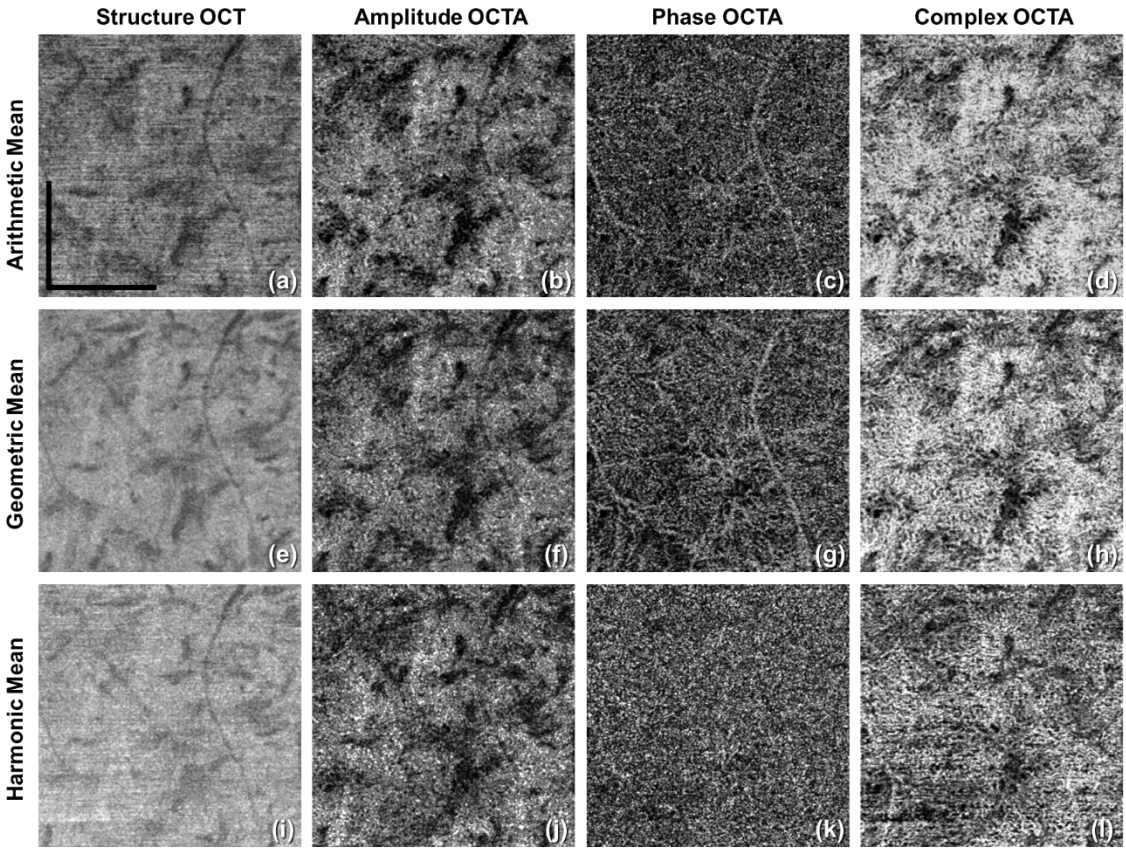


Figure 3.4. Comparison among different Pythagorean mean approaches of CC OCTA in linear display.

(a) – (d) Arithmetic mean approach: structural OCT, amplitude OCTA, phase OCTA and complex OCTA, respectively; (e) – (h) geometric mean approach: structural OCT, amplitude OCTA, phase OCTA and complex OCTA, respectively; (i) – (l) harmonic mean approach: structural OCT, amplitude OCTA, phase OCTA and complex OCTA, respectively. Scale bar = 1 mm.

Table 3.8. Quantitative comparison of image quality between AM and GM approach in terms of image contrast and SNR.

| | Complex | | Amplitude | | Phase | |
|---|---|---|---|---|---|---|
| | AM | GM | AM | GM | AM | GM |
| Contrast | 3.08 | 3.02 | 2.73 | 2.92 | 1.88 | 2.22 |

| | | | | | | |
|---|---|---|---|---|---|---|
| SNR | 3.28 | 3.72 | 3.05 | 3.39 | 1.67 | 2.59 |

As indicated in Equation (4), both the AM and GM are calculated and averaged to boost the SNR and achieve a better contrast for CC vascular imaging. Figure 3. 5 shows the OCT and OCTA *en face* images of CC using this AM/GM combined approach, by employing either amplitude, phase or complex OCT signals. Figure 3. 5 (a) – (d) are linear and (e) – (h) are log displays. Table 2 shows quantitative image quality analysis of Figure 3. 5 (b) – (d). AM+GM approach resulted in higher SNR compared to both AM and GM approach as we expected. As illustrated in Figure 3.s 1 and 2, the amplitude and phase approaches both only use part of the OCT signal and, therefore, fail to utilize the entirety of the OCTA potential. In accordance with our theory, our results prove that OMAG, the complex signal-based OCTA, is superior to both phase and amplitude signal-based OCTA approaches in visualizing the CC.

Observed in Figure 3. 5 is the amplitude signal-based OCTA being highly dependent on the strength of the structure signal; that is, it loses the ability to differentiate moving tissue from static tissue almost completely when the structure signal is low, as indicated by the arrow heads. However, both phase and complex signal-based OCTA are capable of resolving the motion signal where the OCT signal is relatively low. Another observation to be made is that the phase signal-based OCTA is heavily influenced by the tailing artifacts [25]. As indicated by the arrows, the tails of retinal blood vessels are more evident in the phase signal-based OCTA approach. This is so because the tailing artifacts are mainly introduced by the forward scattering photons. When probing photons travel through retinal vessels, they interact with RBCs that is of high anisotropic factor (~0.995), meaning the probability of the photons being scattered forward is much higher than that being backscattered. Therefore, more photons would travel in to deeper tissues where they are scattered back into the detector. In this process, the phase of the light is

changed, i.e. the Doppler shift, but little intensity variation is introduced by the first interaction. Accordingly, the retinal vessels appear dark in the structure and amplitude signal-based OCTA images, as in (a) and (b), but appear bright in the phase signal-based OCTA image, as in (c), because of the Doppler shift introduced by strong forward scattering. Both linear and log displays are illustrated here where log display provides tighter dynamic range and smoother contrast yet linear display shows finer details. Researchers should bear these differences in mind while conducting future studies.

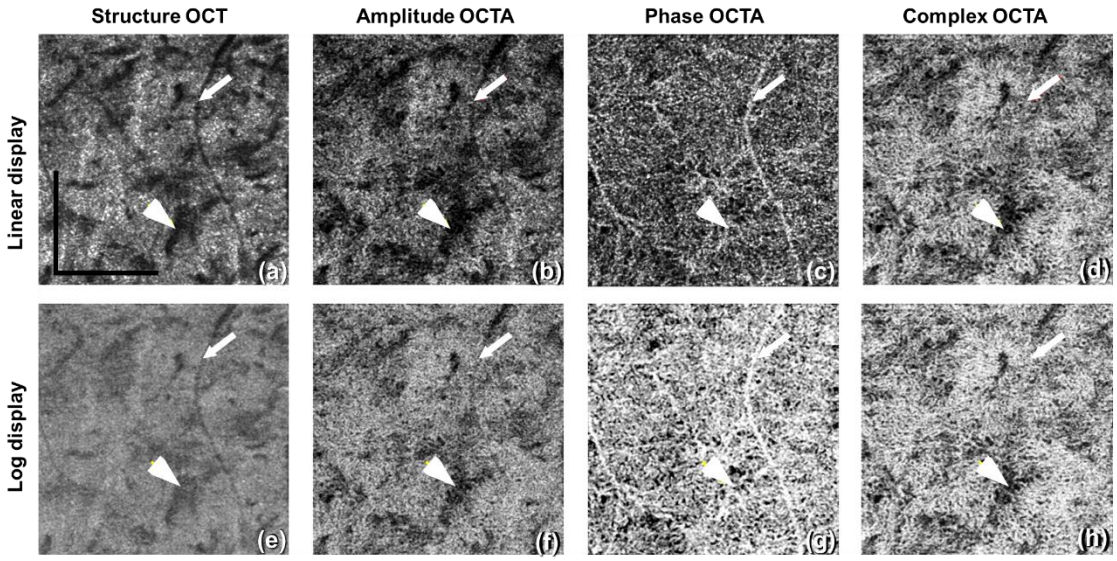


Figure 3.5. Comparison of CC OCTA with AM+GM approach using linear and log display. From left to right column, shown are the results for OCT structure, amplitude OCTA, phase OCTA and complex OCTA, respectively. Arrowheads indicate a region of low structural signal. Arrows indicate the tailing artifact from a retinal vessel. Scale bar = 1 mm.

Table 3.9. Quantitative evaluation of image quality of AM+GM approach.

| | Complex | Amplitude | Phase |
|---|---|---|---|
| | AM+GM | AM+GM | AM+GM |
| Contrast | 3.09 | 2.99 | 2.39 |

| | | | |
|---|---|---|---|
| SNR | 4.15 | 3.46 | 2.84 |

The effect of variable time intervals on CC visualization are shown in Figure 3. 6. Figure 3. 6 (a) – (c) show the CC OCTA images derived from amplitude, phase, and complex signal-based approaches, respectively, with a time interval of 4.5 ms. Figure 3. 6 (d) – (e) show the CC OCTA images derived using the same approaches with a time interval of 9 ms. As explained in the method section, four repeated B-scans were taken at each location to generate OCTA signals. 4.5 ms time interval approach takes the difference between adjacent B-scans (scan 1 and 2; scan 2 and 3; and scan 3 and 4) while 9 ms time interval approach with skipping one (scan 1 and 3; scan 2 and 4). For OCTA imaging with a 4.5 ms time interval, the final results were averaged using three differences, while for OCTA imaging with a 9 ms time interval, the final results were averaged using two differences. For amplitude OCTA and complex OCTA, the increased time interval did not reveal significantly more detailed vasculature in the CC. More differences can be observed in the phase flow image but it's unclear how much is real signal and how much is noise. Overall, the OCTA images with a 9 ms time interval had higher noise floor compared to original OCTA images, i.e. those formed using a 4.5 ms time interval. All images are in linear display to discern detailed changes.

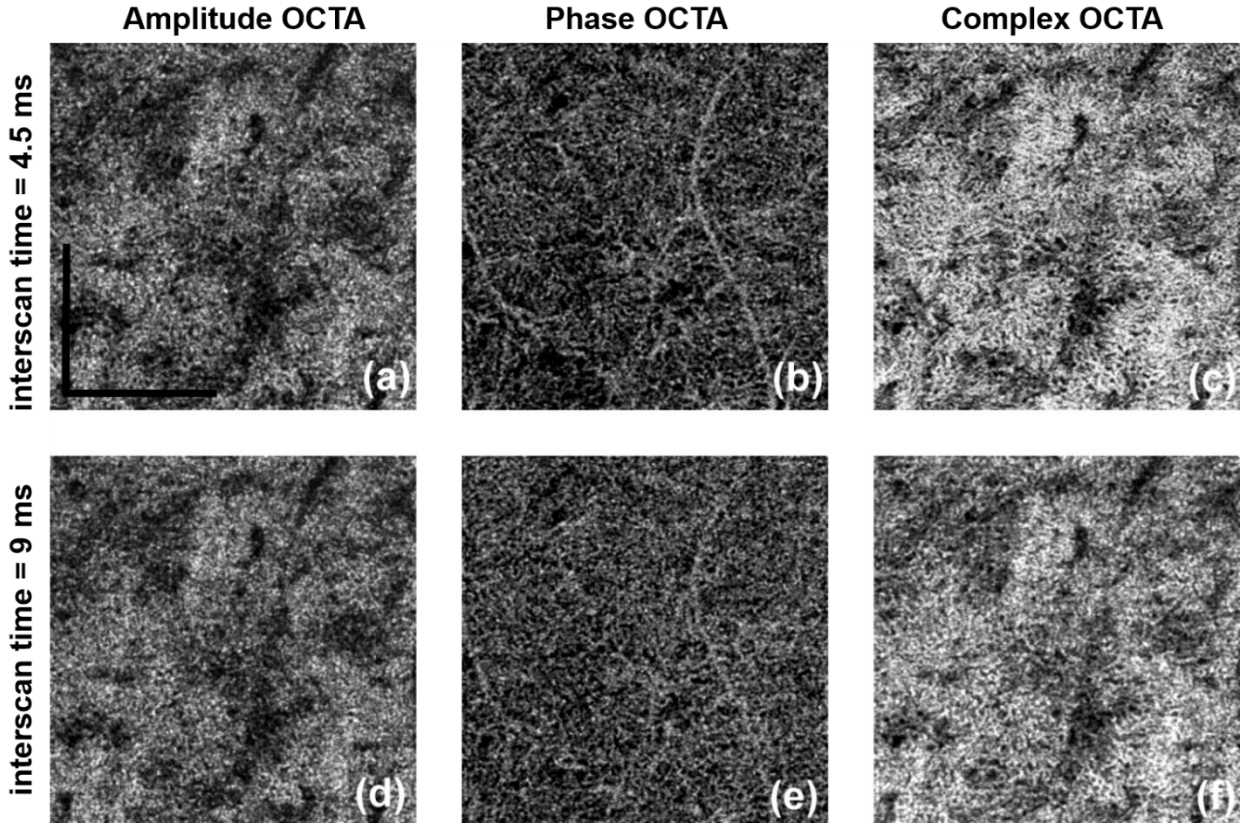


Figure 3.6. Comparing two time intervals for visualization of the CC, linear display. Top row, 4.5 ms time interval, and bottom row, 9 ms time interval. From left to right: amplitude, phase, and complex signal-based OCTA, respectively. Scale bar = 1 mm.

As previously mentioned, the FastTrac™ tracking system specifically designed for use with the AngioPlex system offers an opportunity to provide large FoV montage scanning. Twenty images, 2.4 mm x 2.4 mm each, were stitched together to form a large FoV image of 9 mm x 11 mm as shown in Figure 3. 7, using complex OCTA, GM+AM, log display. CC under the fovea were visualized using 17.6 µm slab while everywhere else were visualized using 11 µm slab, all with 4.5 ms time interval, To the best of our knowledge, this is the first time the CC has been imaged and examined at this large a scale by a commercial SD-OCTA. The varying characteristics of the CC at different locations can be clearly visualized. Consistent with findings reported by histological studies, vessels within the CC under the fovea region are denser and

have smaller vessel diameters. Confined by the lateral resolution of OCT (lateral resolutions of ~15 μm and axial resolution of ~7.5 μm), they appear to be a densely-packed honeycomb vascular network. When moving away from the fovea towards the equator and periphery, the lobular structure of the CC can be recognized more clearly as the vessels become less dense and vessel diameters increase. The CC under the fovea also appears to be dark because the highly scattering RPE is thicker. A longer wavelength light source with higher power can be utilized to improve this limitation.

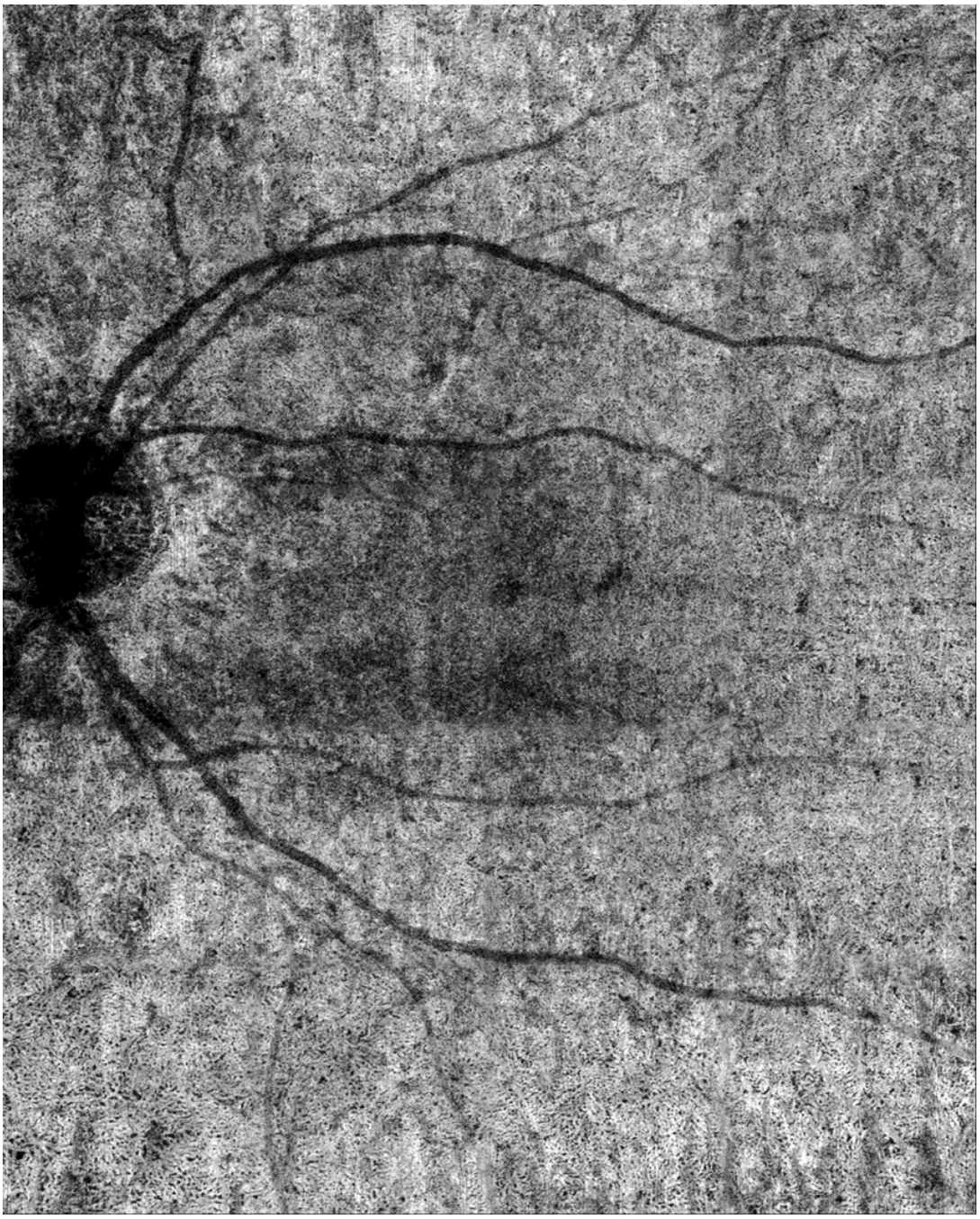

Figure 3.7. Visualization of the CC with a field of view of 9 x 11 $mm^2$ using complex signal-based OMAG in log display.

Figure 3. 8 shows a closer look at the lobular structure of the CC. In each lobule, there is a feeding arteriole from the deeper choroid that travels parallel to the CC plane and inserts perpendicularly into the capillaries lobule via a round opening, which can be observed as the

very small black holes on the OMAG images. In Figure 3. 8, the positions of these openings are highlighted by white arrows. Capillaries connected to this opening are orientated in a radial fashion (also see much higher magnification view in Fig. 9). Such architectural structures can also be seen on the structural OCT *enface* images. Those openings appear darker compared to other natural avascular space between capillaries and could potentially be studied further to see if they can be quantified and represent integrity of a single lobule of CC. Figure 3. 9 shows OCTA images from different depths. The round openings, highlighted by arrows, in (a) is clearly connected to the deeper feeding arteriole seen in (b) and (c). Deeper vessels appear dark since there are few backscattered photons, as explained previously. The draining venules are located at the periphery of the lobules and on the same plane as the CC in the equatorial and peripheral choroid.

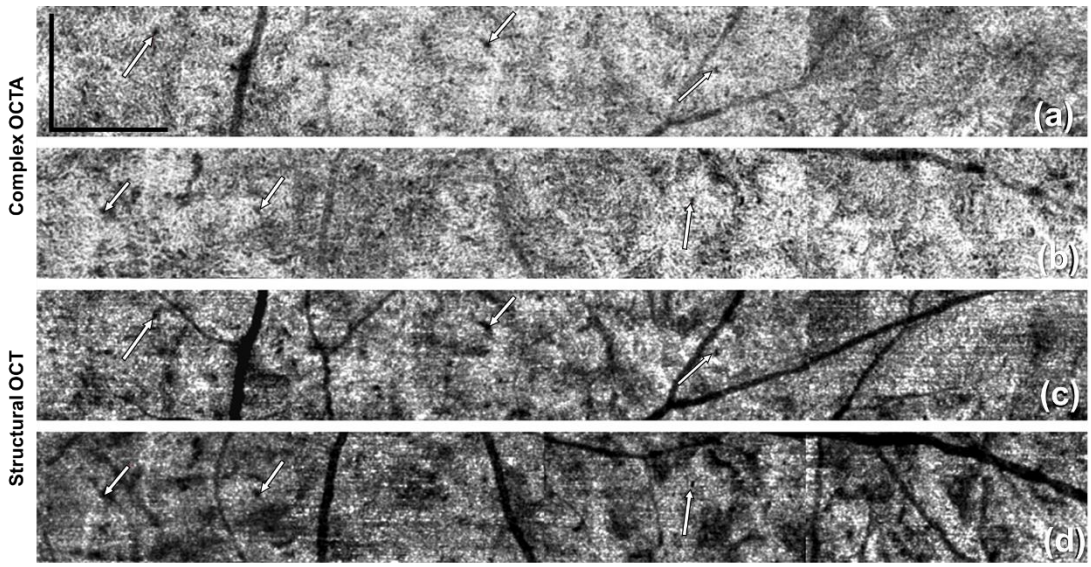


Figure 3.8. Complex signal-based OCTA of the periphery regions, linear display. From (a) superior region and (b) inferior region. (c) & (d) The corresponding structural OCT *enface* images of (a) and (b), respectively. Arrows highlight the insertion points of the feeding arterioles to the CC. Scale bar = 1 mm.

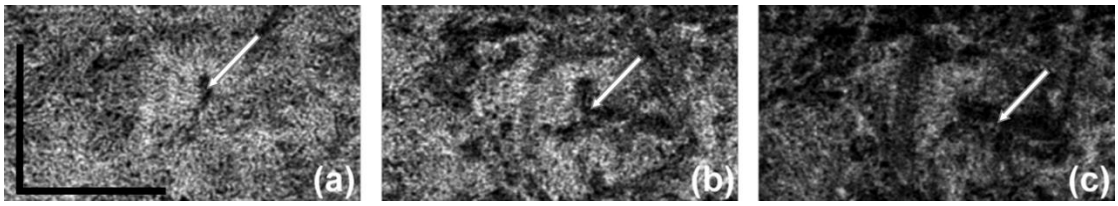


Figure 3.9. Complex signal-based OCTA, linear display.
From (a) a 17.6 μm slab of the CC under Bruch's membrane; (b) a 11 μm thick slab under the preceding slab, and (c) a 11 μm thick slab under (b). Scale bar = 1 mm.

Figure 3. 10 shows the choroidal vessels examined at different depths as they appear to be dark in OCTA images. It is believed that the forward scattering photons that failed to backscatter when interacting with blood still carry information from choroidal vessels and will appear as tailing artifacts in the *enface* projection of the OCTA images of sclera. Our data has shown that the large vessels of the deep choroidal tissue appear dark, as in Figure 3. 10 (b) and (c), and the sclera appears bright due to the tailing artifacts. To show the correspondence more clearly, four vessels have been manually outlined in red.

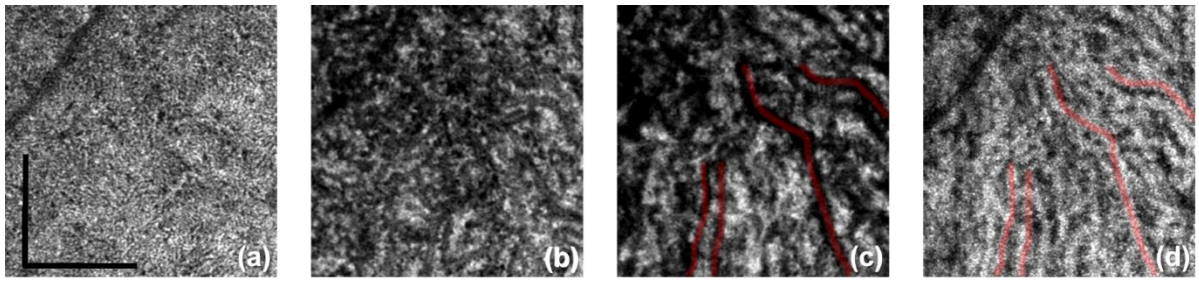


Figure 3.10. OCTA of choroidal vascular networks at different depths.
(a) The CC layer, 11 μm thick slab under Bruch's membrane. (b) Sattler's layer,70.4 μm thick slab under CC. (c) Haller's layer, 81.4 μm under Bruch's membrane to the boundary of choroid and sclera. (d) The sclera layer with projected tailing artifacts. Scale bar = 1mm.

## 3.4 DISCUSSION

We showed that OMAG, a specific complex signal-based OCTA approach initially developed in our lab, is better suited to resolve more detailed lobular vascular network of the CC

than other conventional OCTA approaches, i.e. amplitude and phase signal-based OCTA. The comparison between each approach illustrated that the complex signal-based approach preserved the entirety of the original OCT signal by combining and utilizing the attributes of both other approaches; that is, the amplitude approach contributed most of the OCTA signal strength with the phase approach, providing a useful addition to sensitivity for slow flow. Another key aspect in visualizing the CC is correct segmentation. Instead of using the automatic segmentation technique provided by the imaging devices, we opted for a previously reported semi-automatic segmentation approach [32], which introduced greater flexibility in slab definition. Figure 3. 3 shows that misplacement of slabs could cost researchers dearly when trying to visualize the CC. Additionally, we introduced a geometrical mean approach to boost the SNR in an attempt to compensate for the limited OCTA resolution in resolving detailed CC flow. Our results suggest that GM approach is especially more beneficial in reducing noises in OCTA phase signals. As GM would always yield smaller values comparing to AM, it introduces less fluctuation, thus, AM and GM combined results in higher SNR.

One study [70] has shown that with a 400 kHz SS-OCT, variable interscan time analysis is capable of resolving more CC and choroidal vessels, with the assumption that longer interscan time reveals slower flows at CC and choroid. However, the use of similar tactics in this study did not lead to significant increase in the visualization of vessels within the CC. This discrepancy is most likely a result of the fact that the 68 kHz light source of the AngioPlex produces a very longer interscan time (4.5 ms), whereas the 400 kHz source used by Choi *et al*. has a shorter interscan time (~1.5 ms). Therefore, we believe that slower commercial OCT system provides enough capacity to visualize CC yet faster lab-built system would offer more flexibility.

Our results showed good correlation with previous histological findings. Previous histological studies [43] have shown that the capillaries are tightly organized and separated by septa, the feeding vessels for which can be observed as the very small black holes on OMAG images as shown in Figure 3.s 8 and 9. We have also observed the radial capillary pattern as previously described [43]. To the best of our knowledge, this is the first time this feature has been observed by OCT complex angiograms using commercially available OCTA systems. When moving to a deeper depth as shown in Figure 3. 9, we observed larger dark choroidal vessels that seem to be feeding arterioles of CC as well as surrounding draining venules around the CC lobules. By showing that OCTA can visualize such structures, future studies on further examination and quantification of CC may provide more insights on whether the loss of CC in certain disease can be observed with changes in those small black holes as feeding arterioles. In our study, no obvious inter-subject variations were observed. The distribution of CC follows the "dense under macula, more sparse in the peripheral" pattern in all the subjects examined. We also observed a trend of less dense CC overall in older subjects compared to younger ones. However, our sample size (N=5) is way too small to draw any conclusions here. As explained earlier, the deeper vessels of the choroid appear dark because of the weak back scattered signals. As the anisotropic factor of RBCs is around 0.998 [71], the majority of the interacting photons will scatter forward in blood vessels with only the minority scattering backwards. From those backscattered photons, very few penetrate through the RPE once more time to interfere with the lights from the reference arm. For this reason, the blood vessels in deep choroidal tissues presented in OCTA images are relatively dark instead of white. Figure 3. 10 showed that even though these large vessels are dark in choroid slab, the tailing artifacts of them in sclera appear to

be bright. These tailing artifacts might be useful as an indicator of choroidal vessels as they are notoriously difficult to visualize with OCTA, but further studies are needed for validation.

It should be noted, however, that our study is not without limitations. The first of which is light penetration. Whilst we have shown that with a commercially available SD-OCT, it is possible to observe lobular structures in the periphery, the smaller vessel diameter, increased vessel density of the CC and thicker RPE under the fovea make in-depth visualization more difficult in this region. To overcome this, a swept-source (SS)-OCTA with higher power and better penetration may be required to provide reliable imaging of the CC for the improved ability of visualization and quantification. The second limitation resides the tradeoff between imaging FoV and pixel spacing. Current scanning speeds limit the acquisition of large, high resolution FoV images of the CC, particularly in clinical settings, and whilst our employment of a montage scanning protocol to achieve both high resolution and large FoV overcame this limitation, it did so at the cost of scanning time. It is suspected, however, that future technological advances might resolve this issue. One last limitation is that the image processing strategies to contrast the CC as proposed here is not yet available in the commercial OCTA systems at the time this study was performed. Further studies are clearly needed for this type of additional post-processing and to confirm the algorithm's reliability, repeatability, and applicability in imaging the CC that can provide clinically relevant information.

Despite these limitations, our approach has demonstrated commercially available SD-OCT's capacity in visualizing CC. We have also demonstrated that it is possible to identify the feeding arterioles of the CC, which could be instrumental in improving our understanding of the role played by the choroidal circulation in the pathological processes of ocular diseases. If implemented in the commercial systems, such a technique could potentially serve as a tool for

the early diagnosis of CC malfunction or atrophy, which could subsequently aid in our comprehension of RPE impairment and choroidal circulation.

## 3.5 CONCLUSION

In this study, we demonstrated *in vivo* imaging of the CC of healthy individuals using an AngioPlex SD-OCT (Carl Zeiss Meditec Inc., Dublin, CA, USA) with a 68 kHz A-line acquisition speed and an 840-nm central wavelength. Complex signal-based OMAG was used to visualize architectural morphology of the CC with our results corroborating previous histological and electron micrograph corrosion casting findings. Lobular vascular networks were seen alongside feeding arterioles being identified and confirmed by 3D vascular network information. The ability to visualize the CC with a commercialized system is promising that future extensive clinical imaging studies can examine the role of the CC in ocular diseases, such as diabetic retinopathy, age-related macular degeneration or retinitis pigmentosa. With the capacity of 3D imaging of the whole posterior segment of the eye, OCTA promises to advance our current understanding of pathogenesis, early diagnosis and treatment monitoring of ocular diseases, and could potentially revolutionize the way clinicians manage patients.

# Chapter 4. IMPROVING VISUALIZATION AND QUANTITATIVE ASSESSMENT OF CHORIOCAPILLARIS WITH SWEPT SOURCE OCTA THROUGH REGISTRATION AND AVERAGING APPLICABLE TO CLINICAL SYSTEMS

## 4.1 INTRODUCTION

Choriocapillaris (CC) is a thin physiological layer permeated with dense capillary networks, located at the inner choroid between Bruch's membrane and Sattler's layer. Previous studies [37, 38, 40, 72] have reported close correlation between abnormal CC circulation and multiple retinal/choroidal diseases such as age-related macular degeneration (AMD), diabetic retinopathy (DR), glaucoma etc. Therefore, improving the visualization of CC and its quantitative assessment is of great importance for advancing our understanding of diseases' pathology, early diagnosis and treatment monitoring.

The microvascular network in CC has distinguishing morphologies at different regions. Histological studies [43, 73-75] have shown that CC appears as a dense honeycomb pattern of freely interconnected capillaries separated by septa within the submacular region, while in posterior pole, equatorial and peripheral regions, CC shows a lobular pattern where feeding arterioles and draining venules from deeper choroid join the segment from either the center or on the periphery of lobule [75]. The CC vessel diameter was measured to be 16-20 μm under the macular [73, 75]. Dye-based angiography such as fluorescein angiography and indocyanine green angiography have been used to evaluate CC and observed similar patterns to histological images, but their limited resolution and effects of dye leakage prevent us from visualizing the CC at microscopic level [76].

As a non-invasive imaging technology that uses repeated B-scans to contrast blood flow motions in tissue, optical coherence tomography (OCT) based angiography (OCTA) [53, 77, 78] has drawn increasing attention recently for CC imaging [23, 63, 79-89]. Kurokawa et al. [60] reported successful CC imaging using adaptive optics OCT (AO-OCT) with a 2.4 μm lateral resolution. Their home-built system achieved 0.75 and 1.5 μm/A-scan sampling rate along slow and fast scan direction respectively. Moreover, Gorczynska et al [79]also demonstrated CC imaging using a 1.7 MHz swept source OCT (SS-OCT) with a 14 μm lateral resolution. This high-speed system enabled high lateral sampling rate (4 μm/pixel) and large number of repeated B-scans (10 repeats). Such designs successfully suppressed the noise caused by multiple scattering due to retinal pigmented epithelium (RPE) in CC imaging. However, most commercially available OCTA systems have lower lateral resolution (15-20 μm), larger pixel sampling rate (>=10 μm/pixel) and fewer repeated B-scans (2-4 repeats). Such system specifications have demonstrated satisfactory abilities for retinal vasculature imaging, but fall short of reliable visualization and quantification of the CC.

Within the confinement of commercial OCTA systems, post-processing technologies could be helpful to improve the quality of CC imaging. Recently, several studies [85, 90, 91] have demonstrated that registering and averaging multiple *en face* OCTA images could significantly improve image quality in both retina and CC with SD-OCT, yet the reported method requires a large number of repeated scans and relies on the integrity of normal retinal vasculature. Due to the complexity of CC vasculature, flow deficit (FD) area density has been used as an index to quantify CC with SS-OCT and was found to be closely correlated to diseases [83, 85, 92, 93]. Zhang et al used a normal database to assist the quantification of CC FD, while this approach is plausible, collecting such comprehensive database among multi-centers globally remains time consuming

and challenging. Al-Sheikh et al used Phansalkar's local thresholding to segment CC vasculature from flow deficits, yet their segmented image seems to underestimate vasculature and overestimate FDs. Moreover, more indices for quantitative assessment of CC are in demand for clinical studies and evaluation of treatments.

In this study, we propose a novel approach to compensate the motion pattern of OCT systems with a three-step registration including translational registration, affine registration and B-spline registration, followed with averaging. This will largely improve the image quality of CC for better visualization. For CC quantitative assessment, we also propose several reliable indices based on the resulting *en face* OCTA images of the CC. These indices include FD density, number, size, complexity index and aspect ratio index, and also with which to generate additional functional maps of FD binary map, perimeter map, length map, aspect ratio map, complexity map and size map. We hope these assessments will be of great help to quantitative analysis on the CC vasculature and its correlation with various diseases.

## 4.2 METHODS

This cross-sectional, observational case series was approved by the Institutional Review Board at the University of Washington and was conducted following the tenets of the Declaration of Helsinki and the Health Insurance Portability and Accountability Act of 1996 regulations. Informed consents were obtained from all subjects before participation.

### 4.3.1 *SS-OCTA imaging and CC slab generation*

SS-OCT data were obtained using a PLEX® Elite 9000 (Carl Zeiss Meditec, Dublin, California) with a 1060 nm central wavelength and a bandwidth of 100 nm. This system provides an axial resolution of ~5.5 μm in retinal tissue and a lateral resolution of ~20 μm estimated at the

retinal surface[94]. 3mm x 3mm scanning protocol was used for imaging, with 300 A-lines per B-scan and 300 B-scans repeated 4 time each location per volume. This provides a 10 μm/pixel sampling rate transversally. Recruited subjects were scanned at the fovea and in the equatorial region just outside of infero-temporal arcade. Complex optical microangiography (OMAG$^{c}$) algorithm [26] was used to generate OCTA volume and a semi-automated segmentation algorithm [32] was used to perform layer segmentation with necessary manual correction when needed. CC slab was defined as a 15 μm thick slab, starting 16 μm under the RPE [79, 80]. *En face* CC OCTA images were generated using sum projection and linear display[80]. Standard image pre-processing was applied such as local illumination normalization [95] to compensate for uneven illumination caused by overlaying anatomy such as RPE, floaters or vitreous opacity.

### 4.3.2 *Registration and averaging*

Due to inevitable subject movement, repeated volume scans are required to be registered before averaging. Intensity based registration can be described as a convex optimization problem:

$$\hat{T} = argmin\ C(T_\mu; I_F, I_M) \tag{10}$$

Where $I_F$ is the reference (fixed) image and $I_M$ is the moving image to be registered. $T_\mu$ represents the registration transformation function with parameters $\mu$. $C$ is the mutual information cost function that quantifies the joint entropy of variables, and measures the difference between the fixed and registered images. The goal of optimization is to find the optimal transformation coordinate parameters $\mu$, that can minimize the difference between the reference image and moving image.

To compensate the motion pattern of OCT scans, we adopted a three-step registration approach that includes translational registration, affine registration and B-spline registration. This

software is completely automatic and developed in house (R2016b; MathWorks, Inc, Natick, Massachusetts, USA). Translational registration roughly eliminates large horizontal and vertical misplacement of two OCTA CC images. Then, affine transformation was performed to compensate for geometric distortions such as scaling rotation and shearing between two CC images. Lastly, non-rigid B-spline registration was performed to further refine the registration within the sub sectional images.

Once the images were registered, averaging can be performed to improve CC image quality for further quantification. For each subject, we acquired single scan image, 2-scan averaged image, 3-scan averaged image, 4-scan averaged image and 5-scan averaged image. The computational process is described in Figure 4. 1. Parameters of global entropy [96], global standard deviation, local texture correlation [97] and peak signal to noise ratio (PSNR) [98] were used to evaluate the improvement of registration and averaging algorithm.

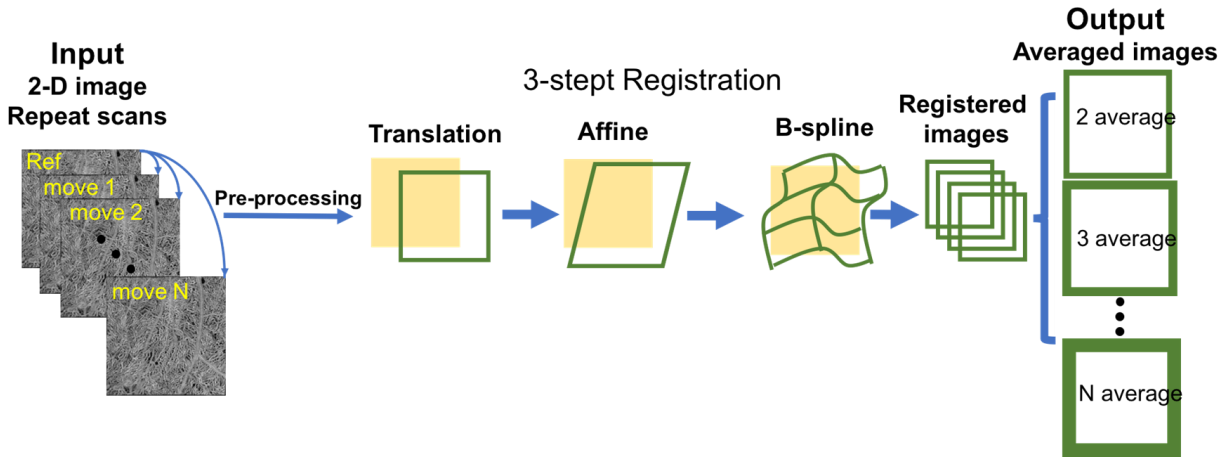


Figure 4.1. Illustration of the registration and averaging method to improve the image quality of the choriocapillaris.

A series of repeat projection images were successively performed translation, affine and B-spline registration with the reference to the first scan, to eliminate the deformation and motion between images. The averaged images enhanced the contrast of CC and decreased the speckle noise level.

### 4.3.3 *Intercapillary distance measurement*

Power spectrum analysis has been widely used to determine collagen fiber orientation[99], this method has also been adopted to assess average CC lumen spacing with both AO-OCTA and SS-OCTA[60, 79]. Here, we used it to measure intercapillary distance (ICD) in macular CC and equatorial CC. Multiple areas of 650μm x 650μm region with clear CC vasculature and no motion artifacts were selected from three subjects in macular, posterior pole and equatorial regions. A two-dimensional power spectrum was generated and radially averaged. The cusp in the radially averaged plot represents the most prevalent spacing, which is the averaged intercapillary distance in the CC image.

### 4.3.4 *Fuzzy c-means clustering for CC segmentation*

After registration and averaging, OCTA *en face* images of CC (Figure 4. 2A) were used for further quantitative assessment. Note that for better illustration purposes, we used scans from a patient diagnosed with chronic birdshot chorioretinopathy. We adopted a fuzzy clustering approach, Fuzzy c-means (FCM) to segment vasculature and FDs in CC, for its widely tested and validated efficiency in medical image segmentation, flexibility in membership determination, and practical spatial constraints [100, 101]. This approach adjusts initial clusters based on partial membership of each site to other clusters to form final clusters that meet the criteria of homogeneity. Elbow method was applied to determine the optimal number of memberships for clusters [102]. That is, to increase the number of clusters until the variance between clusters explained over 99% of total variances (Figure 4. 2B). In the resulting membership map (Figure 4. 2C), each pixel's value was optimized from their original intensity to represent their membership (1-5 in this case) and was

color-coded according to their membership number. CC FD map is generated by segmenting the first membership (Figure 4. 2D). After removing the projection artifacts [25], this binary CC FD map is used for further quantifications.

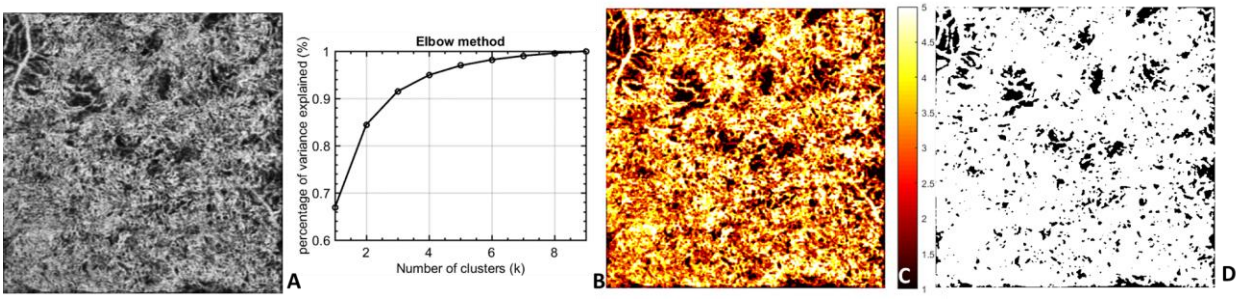


Figure 4.2. Illustration of the CC FV segmentation.

A: averaged OCTA CC image; B: elbow method to determine appropriate number of clusters; C: fuzzy c-means membership map of original CC images, all pixels were assigned into 5 different memberships based on fuzzy logic; D: segmented CC FV pixels presented in black.

### 4.3.5 *Quantitative indices for CC assessment*

We designed a series of quantitative indices specifically for CC with an emphasis on FD. Similar to previously reported study [103], we have generated binary CC FD map, CC FD perimeter map and CC FD skeleton map as shown in Figure 4. 3A, B and C. Additionally, we have calculated the size, aspect ratio and complexity index of individual CC FDs and color coded the values of each CC FD onto the binary CC FD map (Figure 4. 3D, E and F). Correspondingly, we defined a series of quantitative indices calculated from these six maps.

Flow deficit density (FDD) is defined as a unit-less ratio of the image area occupied by CC FDs to the total image area in the CC FD binary map:

$$FDD = \frac{\sum_{i=1,j=1}^{n} A_{(i,j)}}{\sum_{i=1,j=1}^{n} X_{(i,j)}} \quad (11)$$

Where $A_{(i,j)}$ represents white pixels in the binary CC FD map (Figure 4. 3A) and $X_{(i,j)}$ represents all pixels in the binary CC FD map. (i,j) are the pixel coordinates in the OCTA image (assuming a n x n pixel array). A higher FDD value corresponds to more severe CC vasculature loss. We believe this parameter would be useful in most diseases.

Flow deficit aspect ratio index (FDARI) is defined as the average of all individual FD aspect ratios of major axis length to minor axis length.

$$FDARI = \frac{\sum_{i=1}^{x} \frac{M_{(i)}}{N_{(i)}}}{x} \tag{12}$$

Here, $M_{(i)}$ represents the estimated major axis length of each individual FD and $N_{(i)}$ represents the estimated minor axis length. $i$ represents all individual FDs and x is the total number of FDs. FDARI can be used to represent the geometric shape of FDs and therefore contains morphological information. FDARI is similar to the axis ratio in quantifying foveal avascular zone (FAZ) [104], and this index represents the irregularity and acircularity of CC FDs.

Flow deficit complexity index (FDCI) describes the morphological complexity of detected FDs, defined as:

$$FDCI = \frac{\sum_{i=1}^{x} \frac{{P_{(i)}}^2}{4\pi A_{(i)}}}{x} \tag{13}$$

Where $P_{(i)}$ represents the perimeter of each individual FD and $A_{(i)}$ represents the area of each individual FD. $i$ represents all individual FDs and x is the total number of FDs. FDCI describes the morphological complexity of FDs with an emphasis on the boundaries. A higher FDCI value corresponds to a more complicated shape of CC FDs.

Flow deficit number (FDN) is defined as the total number of FDs detected and Flow deficit size (FDS) is defined as the averaged FD size of all FDs detected:

$$FDS = \frac{\sum_{i=1,j=1}^{n} A_{(i,j)}}{FDN} \quad (14)$$

Where $A_{(i,j)}$ represents white pixels in the binary CC FD map (Figure 4. 3A). (i,j) are the pixel coordinates in the OCTA image (assuming n x n pixel array ). An increase in FDN and FDS may indicate increasing number and expansion of non-perfusion areas or FDs. FDN and FDS together can resolve the differences between either a small number of large FDs indicating centralized and localized CC loss, or a large number of small FDs indicating scattered global CC loss, and hence provide more detail than FDD alone.

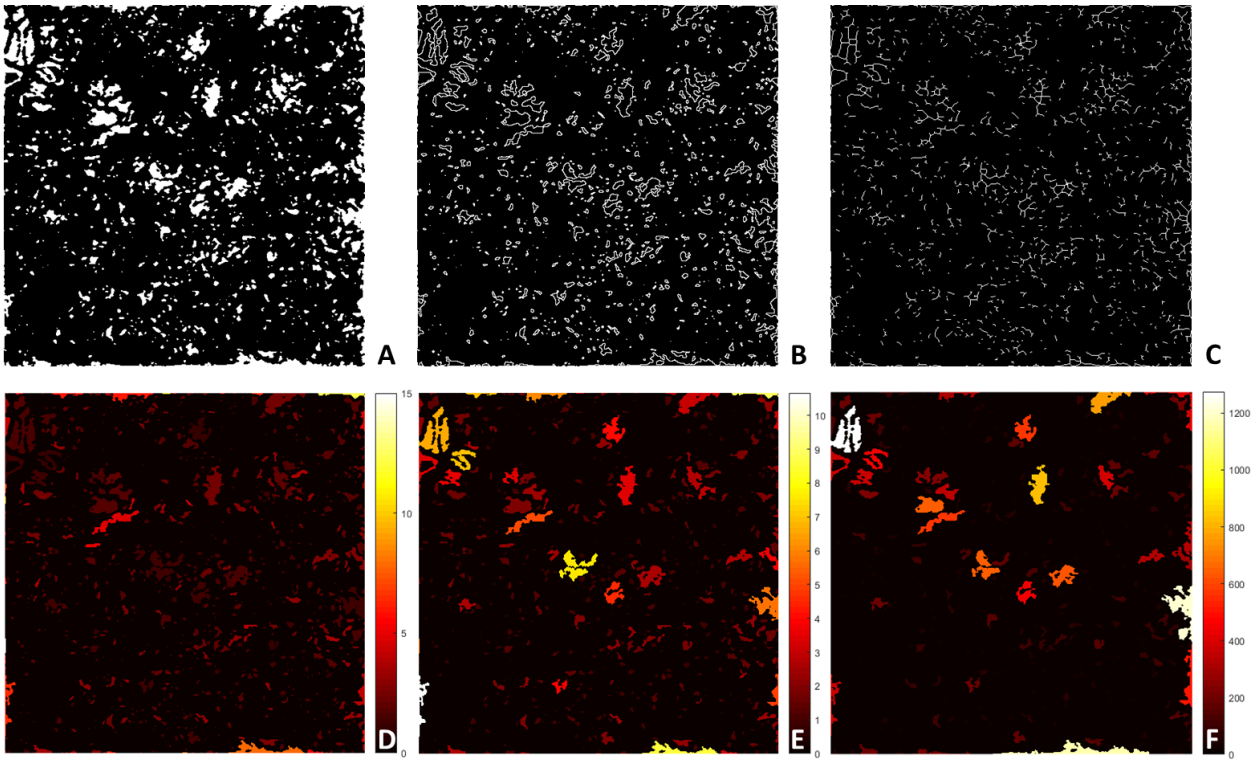


Figure 4.3. Visual illustration of quantification maps.
A: binary CC FV map; B: CC FV perimeter map; C: CC FV length map; D: CC FV aspect ratio map; E: CC FV complexity map; F: CC FV size map.

### 4.3.6 *Statistical analysis*

Statistical analyses were performed using MATLAB (R2016b; MathWorks, Inc, Natick, Massachusetts, USA). Results were expressed using mean and 95% confidence interval (CI). Paired t-test were used to compare the FD measurements from different number of averages and two sample t-test was used to compare the FD measurements of macular CC and equatorial CC. Pearson correlation was used for correlation tests and Bland-Altman analysis was used for agreement tests.

## 4.3 RESULTS

Eleven eyes from six normal subjects (age: 26-67, 4 males, 2 females) were recruited in this study. Each subject was scanned at several locations from the fovea to the equatorial region and with five repeated volume scans.

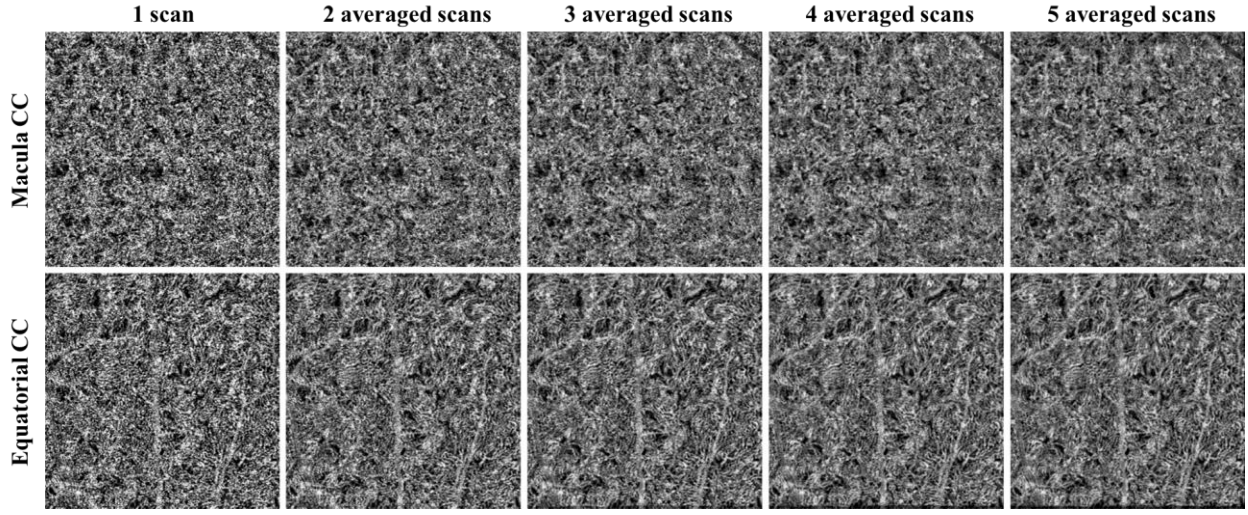


Figure 4.4. Improved visualization of macular CC and equatorial CC with registration and averaging algorithm.

The CC images were acquired at central macular region (Top row) and at equatorial region (Bottom row), respectively.

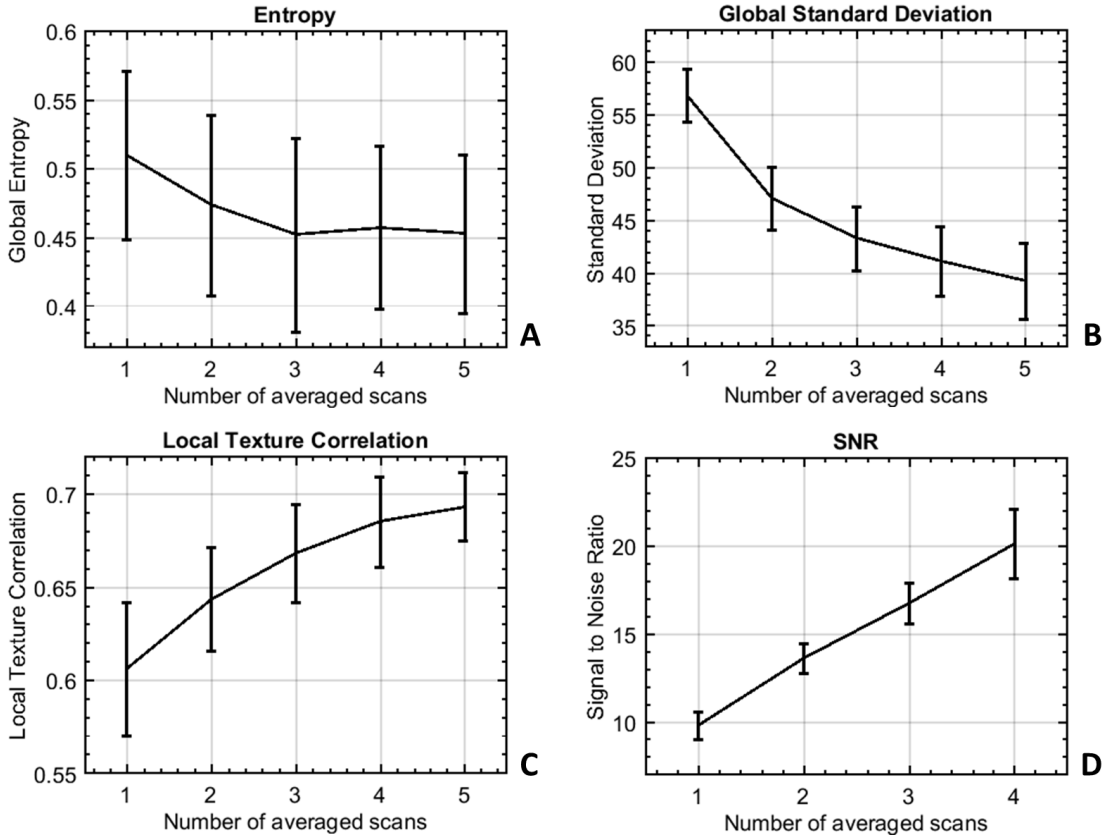


Figure 4.5. Performance evaluation of registration and averaging algorithm against the number of averaged scans.

(A) Global entropy (0–1); (B) global standard deviation (y-axis ranging from 0–255); (C) local texture correlation (y-axis ranging from 0–1); (D) PSNR using five averages as reference.

### 4.3.1 *Improving visualization of CC with registration and averaging algorithm*

Representative averaging effects on OCTA images of macular and equatorial CC were shown in Figure 4. 4. Increasing averaging numbers largely improved the continuity of blood vessels and the overall contrast of the whole image. Furthermore, parameters of global entropy, global standard deviation, local texture correlation and PSNR confirmed the improvement from registration and averaging algorithm (Figure 4. 5). With increasing number of repeats, the global standard deviation decreases as CC images become smoother. Similarly, local texture correlation and PSNR also

increase with the increase of repeated scans. On the other hand, global entropy, a statistical measurement of the randomness, decreases with the increase of repeated scans.

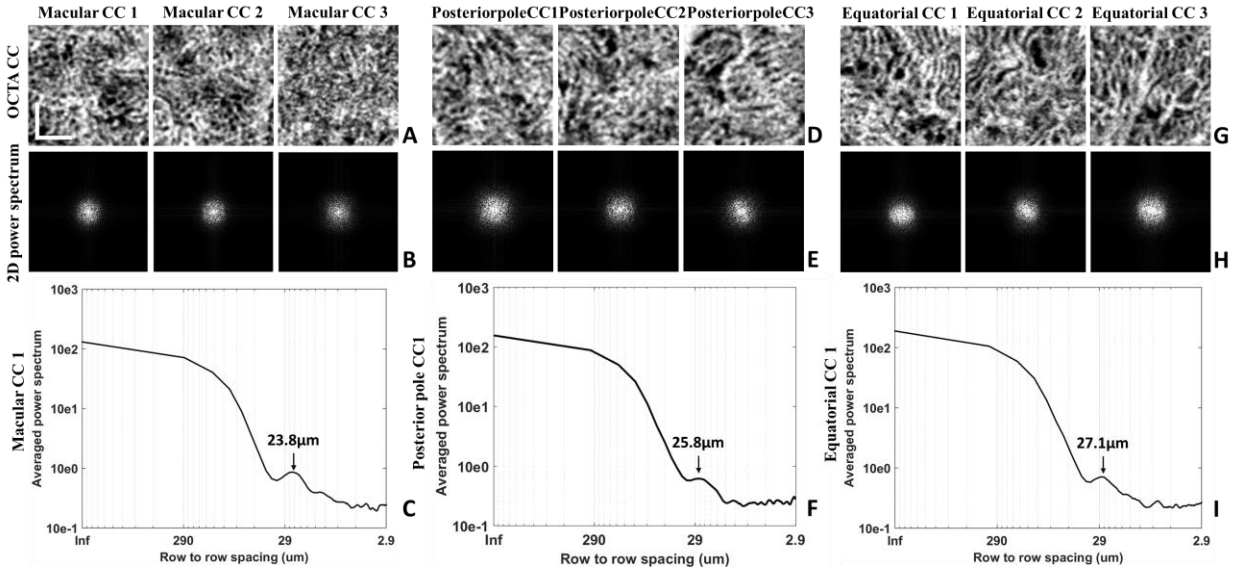


Figure 4.6. Power spectrum analysis of the inter-capillary distance for macular CC, posterior pole CC and equatorial CC, respectively.

Three selected 650 μm *650 μm regions of macular CC; (B) 2D power spectrum of macular CC in A; (C) example radially averaged power spectrum plot of macular CC. (D) Three selected 650 μm ∗ 650 μm regions of posterior pole CC (~4 mm away from fovea); (E) 2D power spectrum of macular CC in D; (F) example radially averaged power spectrum plot of posterior pole CC. (G) Three selected 650 μm ∗ 650 μm regions of equatorial CC; (H) 2D power spectrum of equatorial CC in G; (I) example radially averaged power spectrum plot of equatorial CC. Scale bar represent 200 μm.

Intercapillary distance is a key parameter to evaluate the normality of CC. An improved visualization of CC will result in more accurate measurement of ICD. OCTA images of three selected scans in macular, posterior pole and equatorial segments showed the distinguishing morphologies of CC (Figure 4. 6). This observation was consistent with previous histological anatomies[43, 73]. Averaged ICD of CC was 22.2 μm, 23.5 μm and 23.8 μm for the three scans in macular, 23.2 μm, 23.8 μm and 25.8 μm in posterior pole, and 25.1 μm, 26.2 μm and 27.1 μm in

equatorial regions. Corresponding 95% confidence intervals were reported in Table 1. Polynomial curve fitting was then applied for ICD along macular, posterior pole and equatorial locations. The ICD is around 24 μm in macular regions and become larger toward equatorial regions as indicated by power spectrum analysis (Figure 4. 7).

Table 4.10. Descriptive statistics of CC lumens spacing using spatial power spectrum analysis.

| | Value (95% CI) | | |
|---|---|---|---|
| | **Macular CC** | **Posterior pole CC** | **Equatorial CC** |
| **CC lumens spacing** | 23.17 (21.05 - 25.28) | 24.60 (21.97 - 27.22) | 26.14 (23.64 - 28.62 ) |

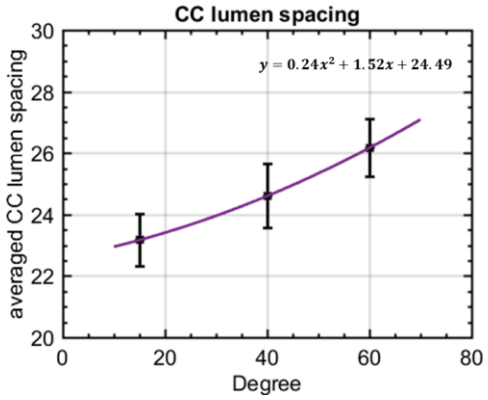


Figure 4.7. Polynomial curve fitting plot of averaged CC lumens spacing along different locations. X-axis indicates the relative locations.

### 4.3.2 *Quantitative indices with multiple averaging*

We further evaluated the quantitative indices with multiple averaging on macular CC and equatorial CC. Figure 4. 8 and Figure 4. 9 show a series of representative averaged CC images, CC vasculature and detected FDs in macular and equatorial CC, respectively. Projection artifacts were removed as colored in yellow. Averaging multiple scans helped smoothing CC vasculature

and increased the continuity of blood vessels. For FD detection, averaged scans reduced speckle noises which resulted in less FDs.

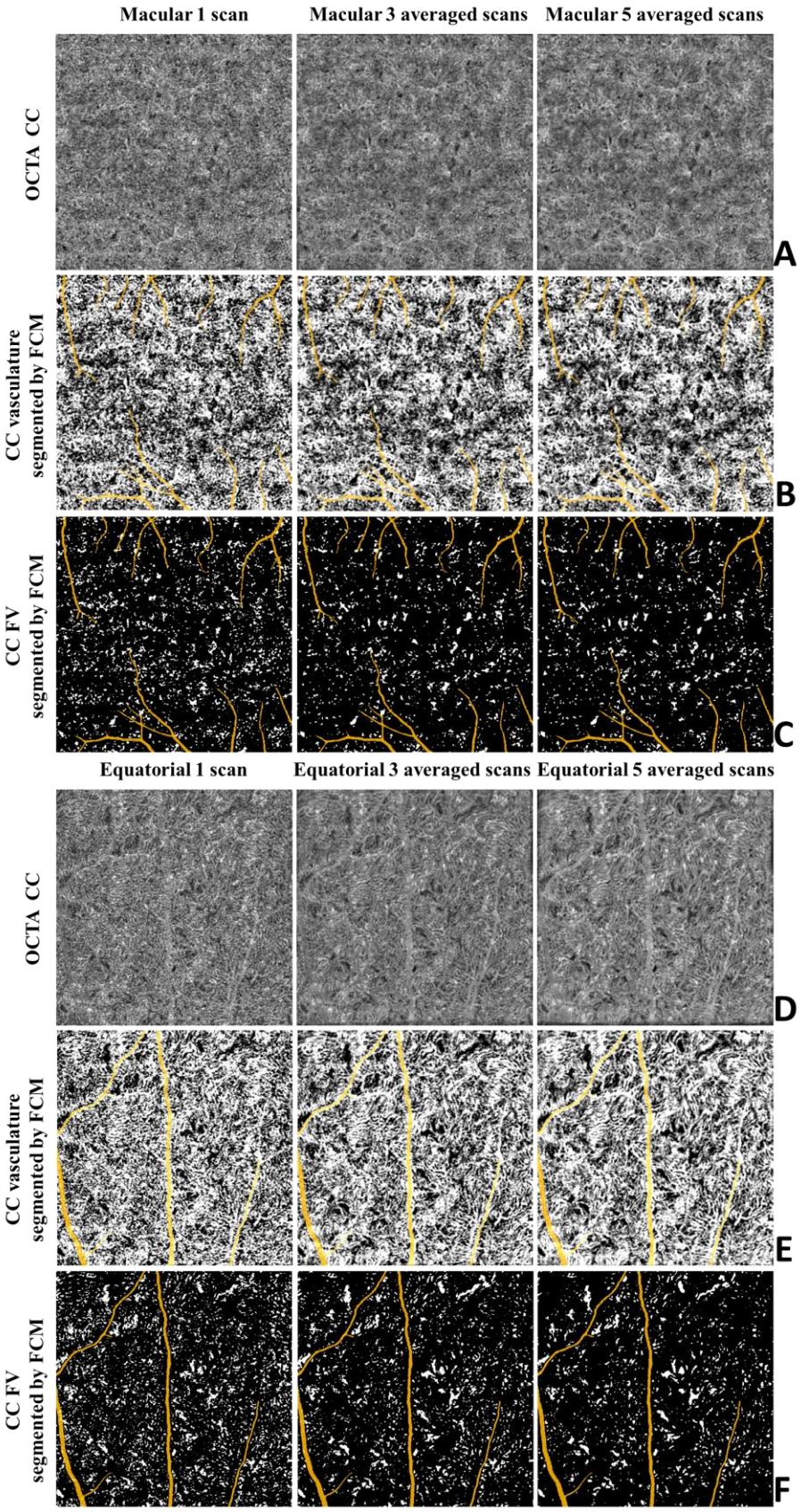
Macular 1 scan
Macular 3 averaged scans
Macular 5 averaged scans
OCTA CC
A
CC vasculature segmented by FCM
B
CC FV segmented by FCM
C
Equatorial 1 scan
Equatorial 3 averaged scans
Equatorial 5 averaged scans
OCTA CC
D
CC vasculature segmented by FCM
E
CC FV segmented by FCM
F

Figure 4.8. Visual illustration of CC FV detection with averaging.
A: macular CC OCTA images with single scan, three scans averaged and five scans averaged; B: macular CC vasculature segmented by fuzzy c-means with single scan, three scans averaged and five scans averaged; C: segmented macular CC FV with single scan, three scans averaged and five scans averaged; E: equatorial CC OCTA images with single scan, three scans averaged and five scans averaged; E: equatorial CC vasculature segmented by fuzzy c-means with single scan, three scans averaged and five scans averaged; F: segmented equatorial CC FV with single scan, three scans averaged and five scans averaged. Projection artifacts were removed as colored in yellow.

FDD, FDN, FDCI, FDN and FDARI were calculated using single-scan OCTA images of CC as well as averaged OCTA images with averaging number of up to five (Figure 4. 10). Significant paired t test results were denoted with *($p<0.05$), ** ($p<0.01$) and *** ($p<0.001$) on corresponding plots. For FDD and FDCI, we found that each time of adding one more scan to register and average decreased significantly until four averaged scans were reached. Five-scan averaged CC OCTA images did not yield to significant difference in FDD or FDCI compared to four-scan averaged ones. FDN and FDS showed significant difference every time we increased the number of repeated scans for averaging. We did not find any significant differences in

FDARI with the increased number of the repeated scans for averaging (data not shown).

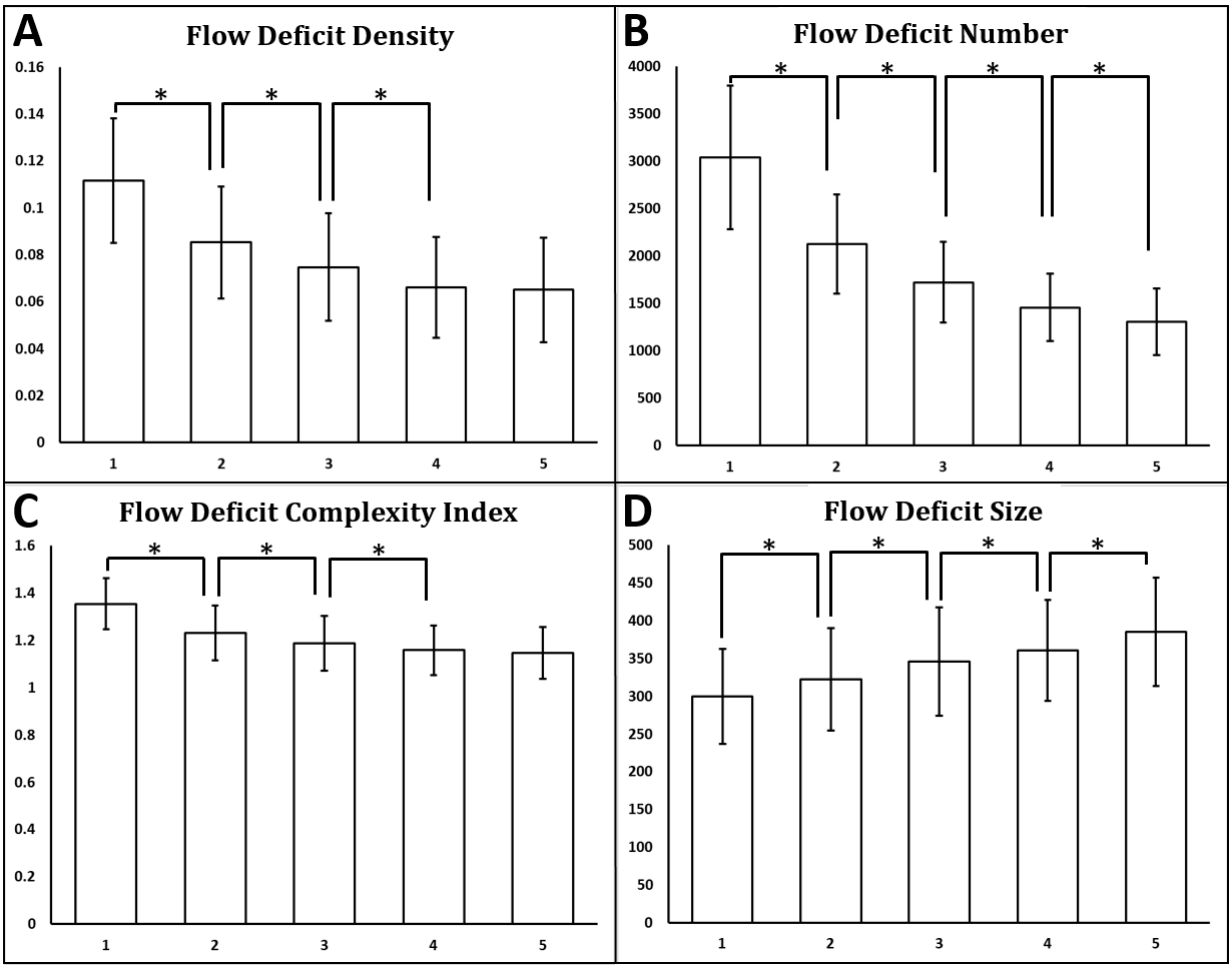


Figure 4.9. Quantitative analysis of CC FDs with multiply averaged OCTA images. X-axis represents number of images averaged. Y-axis in (A) Flow deficits density; (B) Flow deficits number; (C) Flow deficits complexity index; and (D) Flow deficits size. *Denotes $p < 0.05$, **Denotes $p < 0.01$ and ***Denotes $p < 0.001$.

For FDD, which is currently widely used in the literature for CC evaluation, correlation and Bland-Altman agreement plots were produced with increasing numbers of repeated scans for averaging (Figure 4. 11). Five-scan averaged CC were used as a reference for comparison. Correlation was good between single scan and five-scan averages ($R^2$=0.77), with a mean difference of ~0.046 and limit of agreement of 0.021-0.070. Registration and averaging largely

improved the correlation, with $R^2$ increased to 0.95, 0.97 and 1.00 for two, three and four averages, respectively.

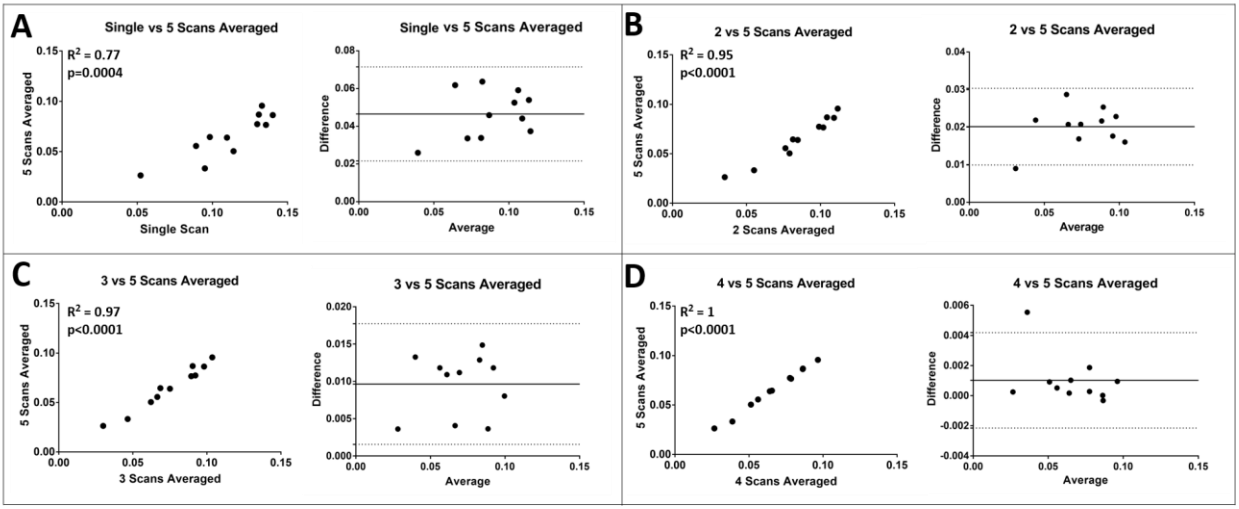


Figure 4.10. Correlation and Bland-Altman plots of CC FDD with multiple averaged scans. (A) Comparing single scan CC FDD results with 5 scans averaged CC FDD results; (B) comparing 2 scans averaged CC FDD results with 5 scans averaged CC FDD results; (C) comparing 3 scans averaged CC FDD results with 5 scans averaged CC FDD results; (D) comparing 4 scans averaged CC FDD results with 5 scans averaged CC FDD results.

### 4.3.3 *Quantitative assessment of macular CC and equatorial CC*

CC under macular and CC in the equatorial regions have been reported to have different vasculature patterns [75] and this was also confirmed in visual presentations and measured ICDs discussed above. Quantitative assessment of CC provides more details of the differences in the two locations (Table 2). For FDD, we found that macular CC has a significantly lower FDD compared to equatorial CC (5.35% vs 8.45%, p=0.002). Equatorial CC were found to have larger FDS than macular CC (432.20 $um^2$ vs 358.96 $um^2$, p<0.0001). No significant difference was found in FDN between equatorial CC and macular CC. Moreover, for the morphology comparisons, equatorial CC showed a higher FDARI than macular CC (2.16 vs 1.95, p=0.01). This indicates that the FDs

are more elongated in equatorial regions which agrees with histological observations[43, 73, 74]. FDCI also yielded to a higher value in equatorial CC than macular CC (1.22 vs 1.11, p=0.02).

Table 4.11. Descriptive stats of quantitative comparison of CC FVs in macular and equatorial regions.

| **Quantitative indices** | **Value (95%)** | |
|---|---|---|
| | **Macular CC (n=5)** | **Equatorial CC (n=5)** |
| **FVD (%)*** | 5.35 (3.76 – 6.94) | 8.45 (7.48 - 9.42 ) |
| **FVS(μm$^2$) *** | 358.96 (277.45 - 440.46) | 432.20 (371.48 - 492.91) |
| **FVN** | 1191 (760 - 1622) | 1538 (1374 - 1704) |
| **FVARI*** | 1.95 (1.90 – 1.99) | 2.16 (1.97 - 2.33) |
| **FVCI*** | 1.11 (1.03 - 1.19) | 1.22 (1.15 - 1.29) |

* denotes p<0.05.

## 4.4 DISCUSSION

In this study, we introduced and validated a novel approach of registration and averaging to improve the visualization of CC, and provided multiple indices for quantitative assessment of CC using SS-OCTA. Our results showed that more averages produce better quality CC images and more distinct features of CC vasculature, and are in accordance with previous histology reports[43, 73, 74]. ICD was measured to be around 24 μm under macula and increasing toward equatorial regions. Our five metrics for CC quantification were validated with multiple averaging and showed significant differences of CC under macula and in equatorial regions.

Unlike prior studies [90] that relied on retinal vasculature for registration and averaging, we performed registration directly on CC vasculature. Since intact retinal vasculature is not required to perform averaging, our method can be applied in various diseased subjects such as DR subjects with severe vasculature loss, subjects with artery or vein occlusions and so on. This is illustrated with the BSCR patient (Figure 4. 2). Moreover, we can register and average CC under the FAZ,

which could be of great importance to study AMD, whereas registration based on retinal vasculature cannot achieve this due to the avascular property of the FAZ.

Limited lateral resolution and sampling rate as well as speckle noises are the major challenges of commercial OCTA systems in imaging CC *in vivo*. In this study, we were able to improve the visualization of CC by registering and averaging multiple OCTA scans. Even though this does not improve the system's lateral resolution, it is very successful in reducing speckle noises that are prevalent in single scan images. We have demonstrated that registering and averaging multiple scans is a practical tool to improve CC imaging on commercial OCTA systems. According to the correlation and agreement analysis, multiple-scan averaged CC images are more ideal than single scan CC images. However, single-scan CC images could still be meaningful in clinical studies where multiple averages are difficult to collect, since CC quantification based on single-scan image correlates well with CC quantification based on 5-scan averaged images ($R^2$=0.77), yet with a mean bias of ~4.5%.

In this study, we have also designed a series of quantitative indices to describe CC FDs: FDD, FDN, FDS, FDARI and FDCI. FDD is the density of FDs that has been applied in previous studies of CC quantification. FDN is the number of total FDs detected while FDS is the averaged size of FDs detected. When two cases have the same FDD, FDS and FDN together can tell the differences between centralized and localized CC loss from scattered global CC loss. FDARI describes the aspect ratio of CC FDs, and similar concepts have been successfully used to detect abnormal FAZ in retina [104]. FDCI described the morphological complexity of FDs, with an emphasis on the boundaries. FDARI and FDCI together could indicate the shape and circularity of FDs. These indices could be useful to study the loss of CC in diseased cases as well as to longitudinally monitor the changes of CC in treatment monitoring and patient follow up.

Encouragingly, our CC quantitative indices showed significant differences between macular CC and equatorial CC. This demonstrates that our quantification can detect the subtle difference in different CC vascular networks, indicating that it is highly possible that our quantitative analysis would be capable of detecting CC abnormalities in diseased cases too.

There are also limitations in our study. Firstly, our sample size is small (6 subjects). To rigorously validate our method a larger sample size will be needed for implementation in clinical settings. Secondly, we have not applied our analysis on diseased subjects clinically on a large scale. There could be potential downsides of averaging. For example, averaging might reduce low speed and intermittent CC blood flow that has a similar pattern as speckle noises. Generally speaking, averaging multiple CC scans would increase the specificity of detecting CC vasculature and decrease the sensitivity. It is unlikely such potential downside would play a significant role in quantitative analysis but future studies on different pathological cases are warranted for further proof.

## 4.5 CONCLUSION

We have shown that the three-step registering, and averaging algorithm based on multiple OCTA *en face* images of CC can largely improve the visualization of CC vasculature. The designed five indices of quantitative assessment of CC as well as the corresponding functional maps demonstrated their capacity in detecting subtle differences in CC vascular networks at different locations. Overall, this technique hold promises for future quantitative assessment of CC in normal and diseased human eyes *in vivo*.

# Chapter 5. QUANTITATIVE ANALYSIS OF THE CHORIOCAPILLARIS IN UVEITIS USING SWEPT SOURCE OPTICAL COHERENCE TOMOGRAPHY ANGIOGRAPHY

## 5.1 INTRODUCTION

Optical coherence tomography angiography (OCTA) is a non-invasive imaging modality that has demonstrated utility in studies of retinal vasculature disease.[16, 36, 103, 105-110] In patients with uveitis, including intermediate, posterior and panuveitis, spectral domain OCTA (SD-OCTA) has identified both qualitative and quantitative retinal vasculature flow abnormalities.[107, 109, 111-114] However, in certain types of uveitis, such as birdshot chorioretinopathy or punctate inner choroidopathy, pathology may also involve or be entirely limited to the choroid and choriocapillaris (CC). [107, 109, 111, 115-119] While case reports and case series using SD-OCTA have identified CC flow abnormalities in patients with some forms of posterior uveitis, the vascular beds below the retinal pigmented epithelium (RPE) complex are not thoroughly investigated and quantitative analysis of CC abnormalities is limited.[83, 86, 92]

The emergence of swept-source OCTA (SS-OCTA) technology allows for more in-depth characterization of choroidal blood flow in healthy and diseased eyes. SS-OCT imaging is better method for visualizing blood flow in the choroid and choriocapillaris due to better depth penetration through the RPE complex and lower sensitivity roll-off when compared to SD-OCT systems.[13] Additionally, acquisition speeds in the 100 Khz range facilitate wide angle imaging,[120] a feature important for diseases like uveitis that frequently manifest extramacular lesions. Finally, segmentation of the SS-OCTA data into choroidal or choriocapillaris *en face* slabs is showing promise for detection of inflammatory disease activity without the need for

fluorescein or indocyanine green based angiography.[116, 121-123] Ultimately, SS-OCTA will provide the maximum clinical utility when image acquisition is coupled with automated image analysis for the rapid and reliable detection of disease activity.

In this study, we apply an automated algorithm to the analysis *en face* SS-OCTA CC images to identify and quantify flow deficits (FDs) in patients with uveitis. This approach was applied to both 3x3 mm and 6x6 mm CC slabs obtained for each patient. For each image, three quantitative values, total FD number (FDN), mean FD size (MFDS), and FD density (FDD), were measured and used to compare images from uveitis patients and normal controls. We show this analysis method is reliable with a low coefficient of variation (CV), and that patients with uveitis have larger MFDS and higher FDD than normal controls. Furthermore, we identify there is a strong correlation between quantitative metrics obtained from 3x3 mm and 6x6 mm scans indicating the robustness of the algorithm despite the varying resolution provided by different scanning protocols. Ultimately, this automated approach will be valuable for quantitative analysis of a wide range of ocular diseases that impact blood flow in the CC.

## 5.2 METHODS

This single-institution retrospective, cross-sectional, observational case series was approved by the Institutional Review Board at the University of Washington and written informed consent was obtained for all subjects. This study was performed in accordance with the tenets of the Declaration of Helsinki and the Health Insurance Portability and Accountability Act of 1996.

### 5.3.1 *Study Population*

Patients 18 years or older, diagnosed with anterior, intermediate, posterior, or panuveitis, or retinal vasculitis were recruited for SS-OCTA imaging between August 2016 and July 2018 at the University of Washington Harborview Medical Center Eye institute. Upon entry in the study, subject data including gender, age, uveitis diagnosis, and involvement of one or both eyes were collected.

### 5.3.2 *Image acquisition and scanning protocols*

Imaging was performed on a 100kHz SS-OCTA PLEX® Elite 9000 (Carl Zeiss Meditec, Dublin, CA), with a central wavelength of 1060 nm, a bandwidth of 100 nm, axial resolution of ~6 μm and lateral resolution of ~16 μm in retinal tissue.[94] FastTrac motion correction software was used during all scans to minimize possible motion artifacts during imaging. 3x3 mm and 6x6 mm volume scans centered on the fovea were obtained for both eyes of all subjects. For each subject the eye with the highest signal strength was selected for further analysis. If both eyes were equal in signal strength, then the right eye was used. Images with severe motion artifacts or signal strength lower than seven were excluded from further analysis.[124]

The CC was defined as the region from 16-31 μm below the RPE. [79] The RPE best fit line was determined using the automatic segmentation software provided in PLEX® Elite, manual corrections were performed when necessary. The complex optical microangiography (OMAG$^{c}$) algorithm [68] was used to generate OCTA volumes and maximum projection was applied to the segmented CC OCTA volumes to generate the *en face* images. A previously published compensation strategy using structural OCT information was also applied to correct the OCTA flow in the CC images for signal attenuation. [93]

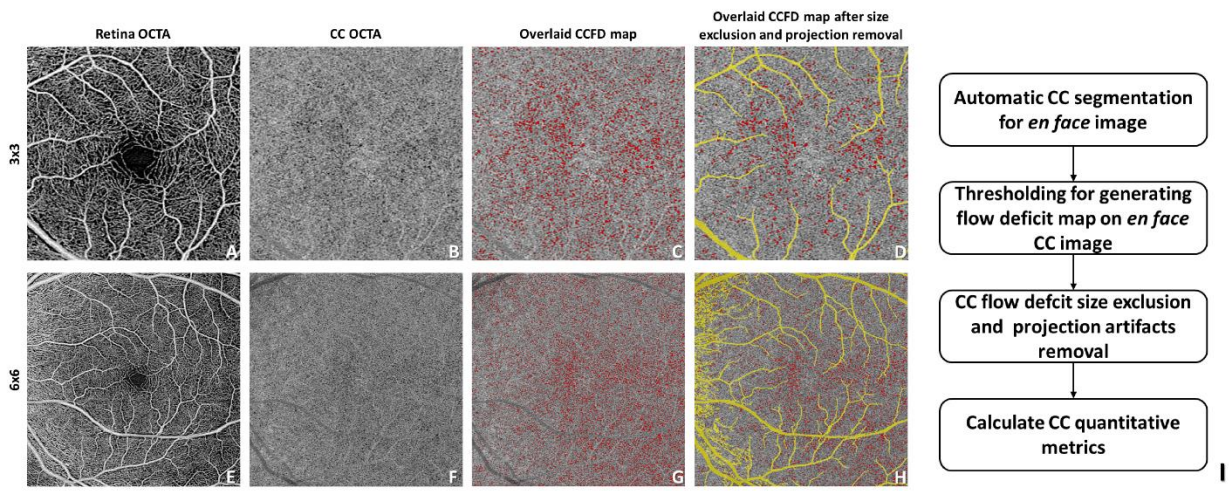


Figure 5.1. Automated detection and quantification of choriocapillaris flow deficits from en face swept-source optical coherence tomography based angiography images.
The diagram shows an example of our proposed CC analysis in a normal patient with both 3x3 mm (A-D) and 6x6 mm (E-H) scans. I: flow chart of the proposed CC analysis.

### 5.3.3 *Definition and quantification of choriocapillaris flow deficits*

In this study the term “flow deficit (FD)” is used to describe areas of no detectable flow signal in the CC slab. In normal controls, these areas are believed to represent the CC vascular walls and intercapillary spaces. In disease states, these areas are believed to represent choroidal non-perfusion,or the presence of choroidal infiltrates leading to blood flow below the OCTA detection sensitivity. The term flow void has also been used in other reports [125, 126] and have been well-described in the literature.[127] FDs were defined on each *en face* image using a custom algorithm employing a comprehensive thresholding strategy.[128] This method is summarized in Figure 5. 1. In brief, for each *en face* CC slab, a complex thresholding algorithm that utilizes fuzzy C-means clustering is applied. Pixels that self-cluster into the lowest intensity group are segmented as the initial FDs. The image is then binarized such that areas of CC flow are bright and the areas of absent flow (FDs) are dark (Figure 5. 1B and F). The final corrected

FD map is generated after masking out areas of projection artifact from overlying retinal vasculature, and removal of FDs that are sub-physiologic in size, i.e. less than the normal intercapillary distance (Figure 5. 1C, G).[128] Finally, quantitative analysis is performed on the corrected map.

Three quantitative metrics were defined for each image: FDN, MFDS and FDD (Figure 5. 1J). FDN is defined as the total number of all individual FDs identified per image, and MFDS is defined as the mean size ($\mu m^2$) of all individual FDs identified per image. FDD is defined as a unit-less ratio of the total area occupied by CC FDs divided by the total image area (minus projection artifacts).

### 5.3.4 *Determination of coefficient of variation*

Five control subjects and five subjects with posterior uveitis were scanned three times at the same visit using both the 3x3 mm and the 6x6 mm scans. Three of the posterior uveitis patients had the diagnosis of birdshot chorioretinopathy and the other two had the diagnosis of serpiginous choroiditis. Repeatability was calculated for each quantitative metric, FDN, MFDS, FDD and reported as the CV.[129]

### 5.3.5 *Statistical analysis*

Statistical analyses were performed using MATLAB (R2016b; MathWorks, Inc, Natick, Massachusetts, USA) and Prism (GRAPHPAD software, San Diego, CA, USA). Cohort data are expressed using the median and interquartile range (IQR). Mann-Whitney U-test and Kruskal-Wallis test with Bonferroni correction were used to compare control and uveitis cohorts. Non-parametric Spearman correlation was used for correlation testing of groups with non-normal

distributions. The receiver operating characteristic (ROC) curve was plotted and the area under the curve (AUC) was calculated to compare the diagnostic power of each metric.

## 5.3 RESULTS

Both eyes of 111 subjects, 73 uveitis patients and 38 controls, were imaged using the PLEX® Elite. One eye per subject was selected for further analysis as described in methods. The average age of uveitis patients was 49 years and the majority were women (71%). Similar age and gender distribution were present in the control group (Table 1). In the uveitis group, the majority of patients were diagnosed with posterior uveitis (n=40, 54.8%), but patients with anterior uveitis (n=20, 27.4%), intermediate (n=8, 11.0%) and panuveitis (n=5, 6.8%) were also represented.

Table 5.12. Increase in the cost of power quality problems in the United States

| | Control | Uveitis | | P value |
|---|---|---|---|---|
| Number | 38 | 73 | | NA |
| Age | 54±22 (32-76) | 49±15 (22-75) | | 0.221 |
| Female percentage | 53% | 71% | | 0.057 |
| Anatomic classification | | Anterior | 20 | NA |
| | | Intermediate | 8 | NA |
| | | Posterior | 40 | NA |
| | | Panuveitis | 5 | NA |

### 5.3.1 *Choriocapillaris Flow Deficit Analysis in Uveitis and Healthy Controls*

222 *en face* CC images were generated from the 3x3 mm and 6x6 mm scans of the 111 study eyes. Representative CC *en face* slabs from control and uveitis subjects are shown in Figure 5. 2. The FD maps for control subjects reveal numerous, small, relatively evenly spaced FDs throughout the macula. Images from uveitis patients demonstrate a range of findings. For

example, images from patients with anterior and idiopathic intermediate uveitis lack qualitative lesions, and appear similar to controls (Figure 5. 2E-H). In contrast, in patients with posterior uveitis, abnormalities of the FD map are grossly apparent. In a patient with Vogt-Koyanagi-Harada disease (VKH), multiple enlarged FDs can be appreciated on both the 3x3mm and 6 x6mm images (Figure 5. 2I-L). An additional example is provided by a patient with multifocal choroiditis that demonstrates large areas of abnormal flow signal loss consistent with widespread loss of the CC (Figure 5. 2M-P).

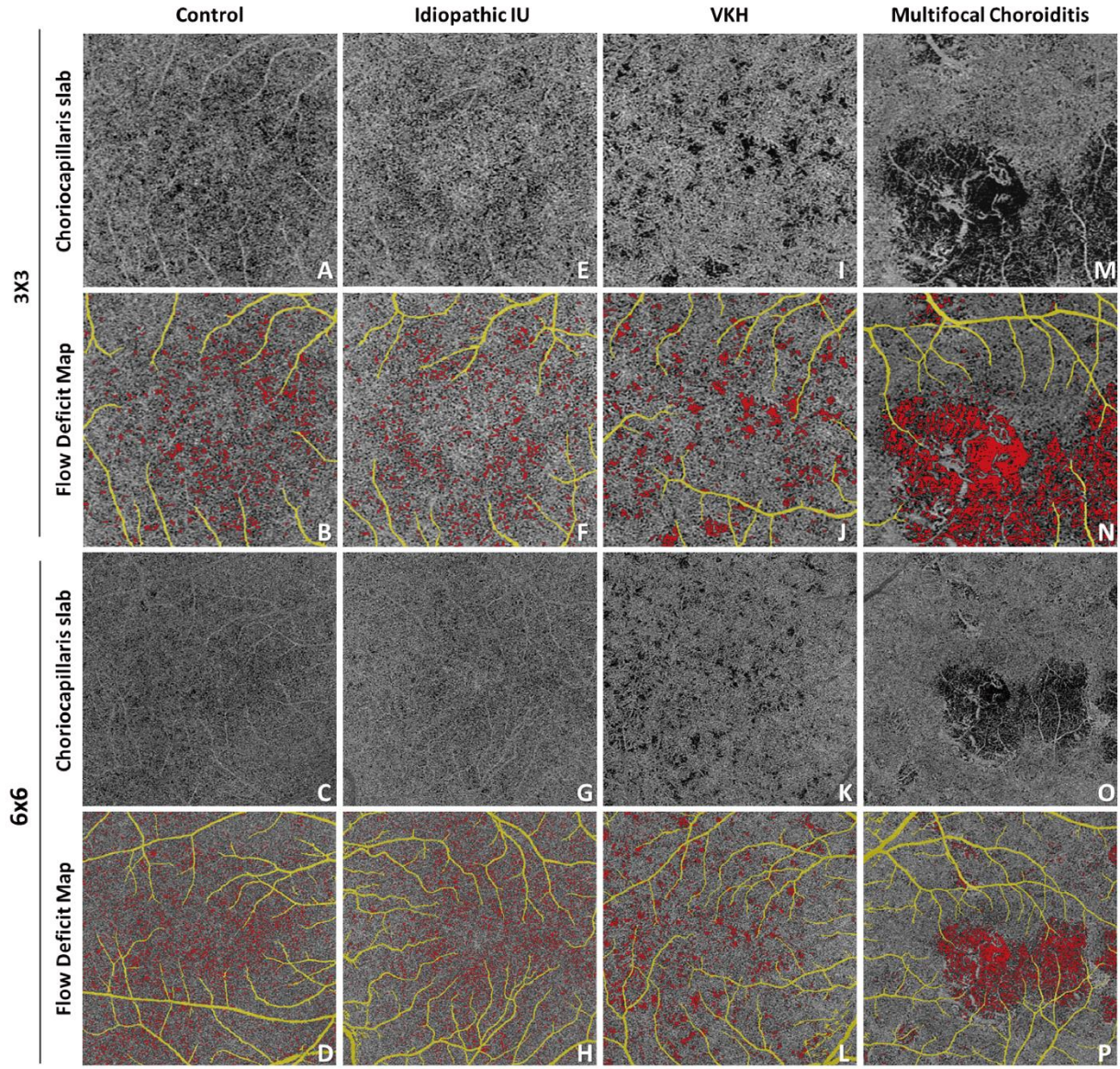


Figure 5.2. Automated detection of flow deficits (FDs) in control and uveitis.

For uveitis, examples are idiopathic intermediate uveitis, Vogt-Koyanagi-Harada disease and multifocal choroiditis. A, E, I, M: OCTA CC slab in 3x3 mm scans; B, F, J, N: computed FD map in 3x3 mm scans, with FDs color coded in red, retinal projection artifacts color coded in yellow; C, C, K, O: OCTA CC slab in 6x6 mm scans; D, H, L, P: computed FD map in 6x6 mm scans, with FDs color coded in red, retinal projection artifacts color coded in yellow;

Table 5.13. Intra-visit repeatability of proposed choriocapillaris analysis.

| CV | FDN | MFDS ($\mu m^2$) | FDD |
|---|---|---|---|

| | | | |
|---|---|---|---|
| **3x3 mm Control** | 5.06% | 2.58% | 4.17% |
| **3x3 mm Uveitis** | 6.57% | 5.57% | 6.65% |
| **6x6 mm Control** | 3.85% | 1.29% | 3.79% |
| **6x6 mm Uveitis** | 5.00% | 4.29% | 4.72% |

Abbreviations: CV, coefficient of variation; FDN, flow deficit number; MFDS, mean flow deficit size; FDD, flow deficit density.

To determine the differences between control and uveitic eyes quantitatively, the three CC flow metrics, FDN, MFDS and FDD, were compared between the control and uveitis groups. Prior to intergroup comparisons, metric repeatability was established using a subset of both controls and uveitis images. CVs ranged from 1.29% to 6.65% (Table 2), with MFDS having the lowest CV among the three metrics (Table 2). The summary of the results for each metric in the uveitis and normal controls are presented in Table 3. In controls, the median FDN per 3x3 mm image is 417 (IQR: 123) and 2365 (IQR: 681) per 6x6 mm image. No significant difference in FDN was identified between control and uveitis patients. In controls, the median MFDS per 3x3mm image is 751.7 $\mu m^2$ (IQR: 69.6 $\mu m^2$) and 802.0 $\mu m^2$ (IQR: 42.1 $\mu m^2$) per 6x6 mm image. The difference in MFDS between uveitis and control eyes is significant on both sized images: 3x3 mm (median: 838.4 $\mu m^2$, IQR: 310.2 $\mu m^2$, $p<0.0001$) and 6x6 mm (median: 870.9 $\mu m^2$, IQR: 274.1 $\mu m^2$, $p<0.0001$). Uveitis patients also demonstrated a significantly higher FDD when compared to controls (3x3 mm: $p=0.0002$, 6x6 mm: $p=0.0076$). Thus, our analysis revealed that CC FDs were larger and more densely clustered in the uveitis patients than in controls.

Table 5.14. Quantitative analysis of choriocapillaris flow metrics in uveitis and controls.

| Median (IQR) | 3x3 | | | 6x6 | | |
|---|---|---|---|---|---|---|
| | FDN | MFDS ($\mu m^2$) | FDD | FDN | MFDS ($\mu m^2$) | FDD |
| Control | 417 (123) | 751.74 (69.64) | 0.037 (0.008) | 2365 (681) | 802.02 (42.13) | 0.058 (0.013) |

| | | | | | | | |
|---|---|---|---|---|---|---|---|
| Uveitis | 442 | (141) | 838.36 (310.25) | 0.042 (0.023) | 2323 (829) | 870.93 (274.14) | 0.063 (0.018) |
| Mann-Whitney U-test | p=0.1061 | | p<0.0001* | p=0.0002* | p=0.6917 | p<0.0001* | p=0.0076* |

Abbreviations: IQR, interquartile range; FDN, flow deficit number; MFDS, mean flow deficit size; FDD, flow deficit density.

### 5.3.2 *Uveitis Subgroup Analysis*

While the quantitative analysis found that as a group, all patients with uveitis have a different size and density of FDs when compared to controls, the qualitative review of images suggested the existence of two populations in the uveitis cohort. We hypothesized that the results from patients with diseases known to involve the choroid could be responsible for the majority of the differences in the quantitative results when compared to normal controls. To test this hypothesis, the uveitis cohort was subdivided into two groups; group A (N=42) without choroidal involvement and group B (N=31) with choroidal involvement (Table 4). [130-133] Group A included diagnoses such as idiopathic anterior uveitis, HLA-B27 associated anterior uveitis, Fuch's heterochromic iridocyclitis, Possner-Schlossman syndrome, Susac's syndrome, idiopathic retinal vasculitis, sarcoid associated intermediate uveitis, and autoimmune retinopathy. Group B included the diagnoses with choroidal involvement such as birdshot chorioretinopathy, multifocal choroiditis with and without panuveitis, punctate inner choroiditis, relentless choroiditis, serpiginous choroiditis, and VKH. Both uveitis groups, A and B, were compared to each other and to normal controls.

Table 5.15. Uveitis diagnosis and grouping for quantitative analysis.

| | Uveitis without choroidal involvement | | Uveitis with choroidal involvement | |
|---|---|---|---|---|
| Number | 42 | | 31 | |
| | Idiopathic AU | 13 | Birdshot Chorioretinopathy | 13 |

| | | | |
|---|---|---|---|
| Retinal vasculitis | 9 | Multifocal Choroiditis | 5 |
| Idiopathic IU | 7 | Serpiginous Choroiditis | 4 |
| HLA-B27 | 5 | Multifocal Choroiditis and Panuveitis | 4 |
| Susac's Syndrome | 3 | Ampiginous Choroiditis | 2 |
| Autoimmune Retinopathy | 2 | Punctate Inner Choroiditis | 2 |
| Sarcoidosis | 1 | Vogt Koyanagi Harada Disease | 1 |
| Fuch's iriodcyclitiis | 1 | | |
| Posner-Schlossman Syndrome | 1 | | |

Table 5.16. Quantitative analysis of choriocapillaris flow metrics in patients with uveitis subgroups and controls.

| Median (IQR) | | 3x3 | | | 6x6 | | |
|---|---|---|---|---|---|---|---|
| | | FDN | MFDS ($\mu m^2$) | FDD | FDN | MFDS ($\mu m^2$) | FDD |
| Normal | | 417 (123) | 751.7 (69.6) | 0.037 (0.008) | 2365 (681) | 802.0 (42.1) | 0.058 (0.013) |
| Uveitis Group A | | 446 (111) | 784.6 (51.1) | 0.040 (0.008) | 2391 (737) | 820.9 (55.7) | 0.059 (0.015) |
| Uveitis Group B | | 438 (234) | 1108.4 (258.4) | 0.060 (0.045) | 2284 (1251) | 1104.5 (328.1) | 0.072 (0.020) |
| Kruskal-Wallis Test (a = 0.05) | | p=0.2666 | p<0.0001* | p<0.0001* | p=0.4680 | p<0.0001* | p<0.0001* |
| Mann-Whitney U-test (a= 0.017) | Control: Uveitis Group A | p=0.2041 | p=0.0339 | p=0.1428 | p=0.9144 | p=0.0239 | p=0.9357 |
| | Control: Uveitis Group B | p=0.4366 | p<0.0001* | p<0.0001* | p=0.2348 | p<0.0001* | p<0.0001* |
| | Uveitis Group A: Uveitis Group B | p=0.9608 | p<0.0001* | p<0.0001* | p=0.2028 | p<0.0001* | p<0.0001* |

Abbreviations: IQR, interquartile range; FDN, flow deficit number; MFDS, mean flow deficit size; FDD, flow deficit density.

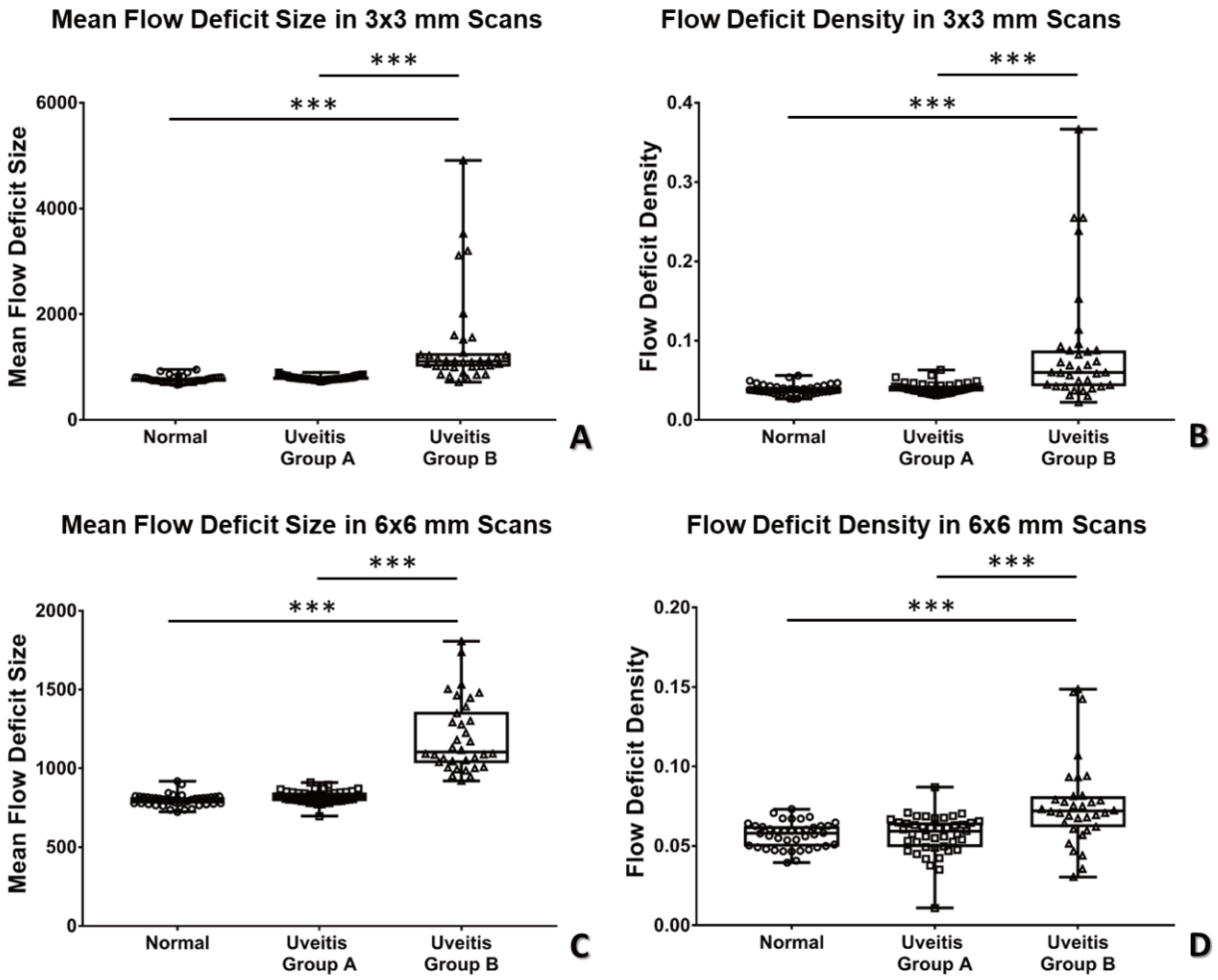


Figure 5.3. Scatter plot of flow deficit density (FDD) and mean flow deficit size (MFDS) in uveitis subgroups and controls in both 3x3 mm and 6x6 mm scans.

A: MFDS in 3x3 mm scans; B: FDD in 3x3 mm scans; C: MFDS in 6x6 mm scans, D: FDD in 6x6 mm scans.

After splitting the uveitis patients into two groups, the quantitative values for the subgroups changed relative to those originally obtained for the whole uveitis cohort. For example, in uveitis group B, the median MFDS increased by ~300 $\mu m^2$, changing from 838 $\mu m^2$ to 1108 $\mu m^2$ on 3x3 mm images and from 871 $\mu m^2$ to 1104 $\mu m^2$ on 6x6 mm images, remained

significantly larger than normal controls (Table 5). Conversely, the MFDS decreased in Uveitis group A and were no longer significantly different from controls. 784 $\mu m^2$ from 838 $\mu m^2$ on 3x3 mm images and to 820 $\mu m^2$ from 871 $\mu m^2$ for 6x6 mm images. For both uveitis groups and controls, no significant differences were identified for FDN. The individual values for MFDS and FDD for each group are shown in Figure 5. 3. These plots highlight the significantly larger FDD (Figure 5. 3A and 3C) and MFDS (Figure 5. 3B, and 3D) seen in uveitis group B when compared to normal controls and uveitis group A.

In summary, these data show that uveitis patients with choroidal involvement have FDs that are both larger and more densely clustered than uveitis patients without choroidal involvement and normal controls.

### 5.3.3 *The impact of scanning window size on quantitative choriocapillaris analysis*

In this study we used two scanning window sizes, 3x3 mm and 6x6 mm. For each window size there is a different digital resolution and signal to noise ratio (SNR) which has the potential to impact the quantitative results. The 3x3 mm scans provide a higher SNR (3x3 mm uses 4 repeated B-scans) and scanning density (10μm/pixel), and may be more sensitive to small variations in FD size. The 6x6 mm scans provide access to larger regions of the posterior pole, but at the cost of digital resolution (12μm/pixel) and SNR (6x6 mm uses 2 repeated B-scans). To determine which scanning size and quantitative parameter has the best ability to differentiate uveitis group B from controls, we assessed the area under the curve generated by the receiver operating curve for each possible combination of test and scan window (Figure 5. 4). In both 3x3 mm and 6x6 mm images, MFDS could best differentiate uveitis group B from controls (3x3, AUC = 0.9480; 6x6, AUC = 0.9714). FDD also demonstrated good discrimination ability in both windows, (3x3 AUC = 0.8505 and 6x6, AUC = 0.8093). FDN was not able to differentiate

uveitis group B from controls in either 3x3 mm (fail, AUC 0.5733) or 6x6 mm (fail, AUC = 0.4429) images.

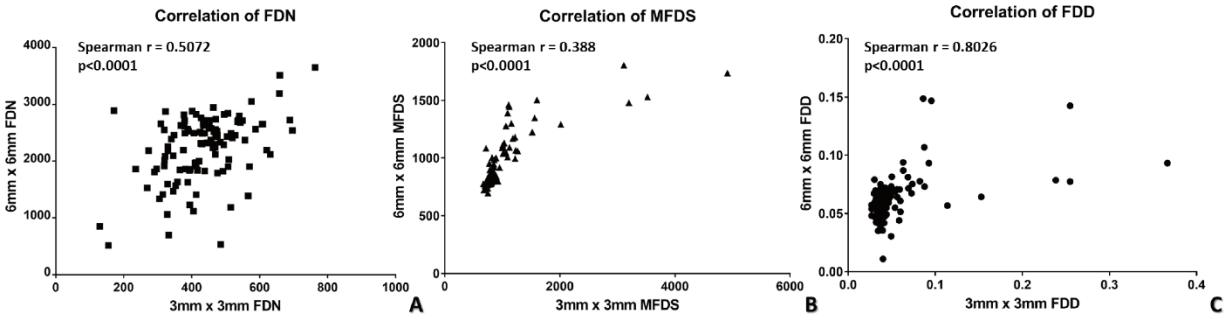


Figure 5.4. Nonparametric Spearman correlation of 3x3 mm and 6x6 mm scans for quantitative choriocapillaris metrics.

A: Spearman correlation of 3x3 mm and 6x6 mm scans with flow deficit number; B: Spearman correlation of 3x3 mm and 6x6 mm scans with mean flow deficit size; C: Spearman correlation of 3x3 mm and 6x6 mm scans with flow deficit density.

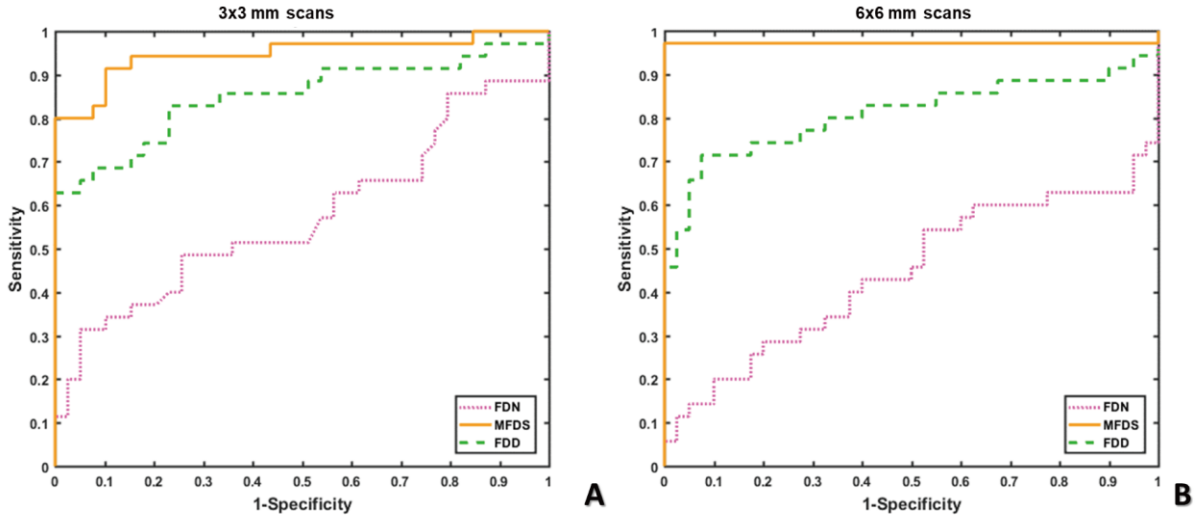


Figure 5.5. Receiver operating characteristic (ROC) curves of all choriocapillaris (CC) quantitative metrics.

A: ROC curves of all CC quantitative metrics in 3x3 mm scans; B: ROC curves of all CC quantitative metrics in 6x6 mm scans; (flow deficit number = FDN, mean flow deficit size = MFDS and flow deficifit density = FDD).

To further investigate the relationship between quantitative CC analyses in the two scanning sizes, we conducted non-parametric Spearman correlation for all three FD metrics (Figure 5. 5). Significant correlation (all $p<0.0001$) was observed in all three metrics, with MFDS demonstrating the strongest correlation among all (Figure 5. 5C, $r = 0.8026$), followed by FDD (Figure 5. 5A, $r = 0.5072$) and FDN (Figure 5. 5B, $r = 0.388$). These results indicate that even though 3x3 mm and 6x6 mm scans have different diagnostic powers as demonstrated by the ROC data, each of the FD measurements are still significantly correlated and are good at identifying uveitis group B from controls.

## 5.4 DISCUSSION

In this study, we have utilized a novel automated algorithm to perform a quantitative analysis of *en face* SS-OCTA CC slabs from patients with uveitis and from normal controls. Using this unbiased, objective approach, we show that the FDs in patients with uveitis are larger in size and occur at a higher density than FDs of normal controls. However, uveitis includes a large and heterogenous group of diseases, many of which would not be expected to manifest pathology of the CC. Therefore, to test the hypothesis that only diseases with choroidal involvement are responsible for these differences, we subdivided the uveitis cohort into two groups based on the anatomic location of their inflammation. This subgroup analysis confirmed that the number, size, and density of FDs in patients with anterior uveitis, intermediate uveitis or isolated retinal vasculitis, are not significantly different than controls. In contrast, the patients with posterior or panuveitis have significantly larger and denser CC FDs than both normal controls as well as patients with anterior segment inflammation.

Quantitative analysis of CC blood flow presents different challenges than similar analyses of retinal vascular blood flow.[134] Moving from SD-OCTA to SS-OCTA has made

choroidal anatomy more accessible and improved the quality of images for quantitative analysis. However, challenges remain including the complicated OCT signal attenuation and scattering though the RPE complex, the high degree of lateral resolution required to accurately resolve CC structure. To address the resolution obstacle, we utilized a combination of image processing steps that included a complex thresholding approach sensitive to the intrinsic histogram of each image,[135] elimination of sub-physiologic size FDs, [128] structural compensation for possible signal attenuation due to RPE,[93] and removal of projection artifacts.[136] Our results here indicate that this approach is useful and can produce results with high repeatability.

One of the benefits of quantitative image analysis is that it can provide an accurate measurement of clinically relevant parameters of choroidal blood flood for diagnostic applications and longitudinal monitoring. Quantitative metrics of the retinal vasculature have been developed that describe the length, density, or branching patterns of the vessels, and these metrics have been used to define characteristics of the retinal vasculature in healthy and diseased eyes.[81, 106-108, 137] In contrast to the approach used to define retinal blood flow, terms defining CC blood flow have been developed that describe the areas without blood flow. This convention was adopted partially because normal CC vasculature cannot be completely resolved by commercial OCTA systems. Common OCTA lateral resolution (~15-20 μm) is larger than common CC inter-capillary distance (ICD) in the posterior pole (5-20 μm),[74] but smaller than the ICD in retina (71.30 ± 5.17 μm).[138] Therefore, the most striking features in CC in a normal eye are the small dark spots that represent the absence of detectable flow rather than detailed CC vasculature. In eyes with posterior segment pathology, the dark spots tend to match areas of visible pathology. [116, 121] The terminology for these dark spots has not been firmly established, but they have been termed FDs, flow voids, and flow signal voids.[93, 128, 139-141]

We favor the term FD as the OMAG algorithm used to generate flow data is based on the movement of red blood cells. Thus, the absence of a flow signal is most likely to represent a *deficit* of red blood cell *flow*.

We chose to use three previously published quantitative metrics to summarize and compare the images in this study: total FDN, MFDS, and FDD. We found that patients with posterior uveitis have significantly larger MFDS and higher FDD when compared to both normal controls and uveitis patients without posterior involvement. Furthermore, this pattern held true for images from both the 3x3 mm and 6x6 mm scans. Such quantitative metrics that are robust when applied to high resolution foveal scans as well as larger size scanning windows will be important for use in diseases such as uveitis that often have pathology extending throughout and beyond the central macula. 3x3 mm scans use four repeated B-scans to generate OCTA data and have a lateral spacing of 10 μm/pixel. In contrast, 6x6 mm scans use two repeated B-scans to generate OCTA data have a lateral spacing of 12 μm/pixel. Thus, 3x3 mm scans have higher digital resolution and higher SNR than 6x6 scans. Despite these differences, we were able to detect significant differences between our study groups in both scanning sizes. Furthermore, the ROC analysis suggests that even though the 3x3 mm scans outperform the 6x6 mm scans using FDD (3x3 mm: AUC = 0.8505, 6x6 mm: AUC = 0.8093), the 6x6 mm scans are better than the 3x3 mm scan for detecting pathology in patients with uveitis using MFDS (3x3 mm: AUC = 0.9480, 6x6 mm: AUC = 0.9714). While the clinical exam will almost always be sufficient for making this distinction, there are forms of posterior uveitis that mimic age-related macular degeneration, and it is possible that differences in MFDS could be used to differentiate diseases like posterior placoid choroiditis or choroidal neovascular membranes from punctate inner choroiditis from these more common diseases.

There are a number of limitations to our automated approach. Most importantly, signal strength has a strong impact on reproducibility of FD identification. We used a highly curated data set here that represents images with a signal strength of 8 or higher. Media opacity generated by active inflammation in the vitreous or anterior chamber can significantly decrease image quality, and thus automated analysis may not be able to be performed in certain patients. Additionally, patients with active macular edema were excluded from this study due to significant signal alterations in the CC in areas under large intraretinal fluid. Further algorithm development will be required to mitigate the aberrations generated prior to quantitative FD determination. We also had a relatively limited sample size for each specific uveitic diagnosis, making it difficult to pursue an etiology-based CC analysis. Despite these limitations, our study demonstrated a novel and reliable quantitative CC assessment using SS-OCTA in a rapid and automated fashion. Our approach can be applied to a variety diagnosis of uveitis and may be potentially useful in clinical settings to assess disease severity and to monitor disease progression or activity.

# Chapter 6. QUANTIFICATION OF CHORIOCAPILLARIS WITH OCTA: A COMPARISON STUDY

## 6.1 INTRODUCTION

Choriocapillaris (CC) is a thin but dense vascular monolayer located beneath Bruch's membrane (BM) in the inner choroid. Multiple histopathological reports have shown that there are correlations between CC integrity and ocular diseases such as age-related macular degeneration (AMD), diabetic retinopathy, and uveitis[37, 38, 40, 118]. While the ability to perform *in vivo* quantitative imaging of the CC would be of great clinical value, only recently has the advent optical coherence tomography (OCT) based angiography (OCTA) made this possible with depth resolved capability and high spatial resolution (~15-20 μm laterally, ~6 μm axially), which permits vasculature quantification.[53, 78] Many researchers have reported useful quantitative parameters, for example, vessel area density (VAD), vessel skeleton/length density (VSD/VLD), vessel diameter index (VDI), vessel complexity index and flow impairment zone; all of which may be used to describe retinal vasculature abnormalities in various ocular diseases[29, 103, 106-108, 137, 142, 143]. Such ability to quantify the vasculature is attributed to the power of OCTA to resolve the microvascular networks of the retina because the inter-capillary distances (ICDs) are generally larger (71.30 ± 5.17 μm [138]) than the system's lateral resolution (~15-20 μm). However, we should be aware that if two vessels are separated with a distance similar to or less than the system's lateral resolution, then OCTA would not be able to tell them apart. Unlike the retinal microvasculature, the CC is a much denser capillary network.

Histological studies[43, 73-75] have revealed that the CC vasculature has different morphological appearances in different regions: a dense honeycomb network of freely

interconnected capillaries separated by septa in the submacular region and a polygonal lobular network in the equatorial and peripheral regions. The inter-capillary distance ranges from 5-20 μm in the posterior pole to 20-300 μm in equatorial and peripheral regions. [74] Given the wide range of the CC ICDs, the current commercial OCTA systems would not always be able to resolve the CC vasculature, particularly in the posterior pole region where the CC abnormalities are thought to be closely related to the development of AMD. Consequently, it remains problematic to directly visualize the CC vasculature from OCTA images.

Rather than visualize the CC vasculature directly, many researchers have chosen to segment and quantify CC flow deficits (FDs)[60, 63, 80, 83, 85, 90, 92, 93, 128, 144] , which should indicate an impairment of CC flow or flow that is below the OCTA detection sensitivity. By definition, the flow deficit must have a size that is larger than the normal ICD, which may be within the capability of OCT system to resolve. Several different algorithms for CC FD segmentation have been reported. Al-Sheikh et al. (2017) reported a method of segmenting the CC FDs using Otsu's global thresholding[90]. However, the assumption of Otsu's method is that the image histogram should follow a bimodal distribution[145], which unfortunately is not the case for OCTA CC images. Nesper et al. (2017) and Borrelli et al. (2018) reported a method of segmenting the CC FDs using the mean pixel value in the outer retinal layer (ORL) as a global threshold[146, 147]. This approach relies on the assumption that the ORL and CC layer share the same systemic noise characteristics, but this is not the case because the CC lies under the retinal pigment epithelium (RPE) complex, which raises the noise floor due to its high scattering nature. Carnevali et al. (2017) reported CC FD segmentation using the mean pixel value in the CC layer as a global threshold[148]. This approach is problematic because the CC vasculature is extremely dense, and it is almost impossible to use the mean pixel value as the cutoff threshold between

flow and absence of flow. Moreover, Sugano et al. (2018) used a method commonly seen in retinal vasculature analyses: hessian filter to segment CC vasculature [149]. This approach is also invalid because OCTA cannot resolve the CC vasculature in the posterior pole and there are no tube-like structures for hessian filter to work with.

As a method designed for binarization of low contrast images[150], Phansalkar's local thresholding method in Image J (National Institutes of Health, Bethesda, Maryland, USA) has become one of the most popular methods for the CC FD segmentation[83, 90, 92, 124, 125, 151-154]. Most researchers have chosen a 15-pixel radius in the analysis, regardless of the actual properties (i.e. actual pixel size) of different OCTA CC images. For example, Spaide et al. first reported in 2016 the use of a 15-pixel radius (~148 μm) with 304x304 pixel 3x3 mm OCTA images[92] but later in 2018 reported the use of the same 15-pixel radius (~88 μm) with 512x512 pixel 3x3 mm OCTA images[155]. Other researchers have reported using the same 15-pixel radius with 1024x1024 pixel 3x3 mm OCTA images[153] (~44 μm) as well as 1024x1024 pixel 6x6 mm OCTA images[124, 153](~88 μm). The lack of consistency in the physical dimensions of the radius could affect the application of the Phansalkar method and lead to discrepancies in CC FD measurements.

Recently, a more reliable method, based on a fuzzy C-means self-clustering algorithm, has been reported to segment the CC FDs[128]. This method automatically assigns all pixels in an OCTA CC image into different clusters based on histogram distribution. It also utilizes localized information to remove noise after clustering. The cluster with the lowest intensity is then identified as the FDs while other clusters are identified by the region occupied by the CC vasculature. This approach was used to measure the average ICD in the macular CC of subjects with normal eyes, which was found to be around 24 μm using power spectrum analysis[128].

Given the increasing interests in quantitative studies of the CC, there is a pressing need to investigate and understand how CC quantification can be conducted in a thoughtful and reproducible way. Several factors could potentially greatly affect CC quantification, such as scan signal intensity, correct CC slab segmentation, effective CC FD segmentation and appropriate selection of CC quantitative parameters. In this study, we compare the results of different CC FD segmentation algorithms on 3x3 mm and 6x6 mm OCTA scans of both normal eyes and eyes with drusen as the basis to discuss the necessary steps and precautions for proper CC quantification.

## 6.2 METHODS

This retrospective, cross-sectional study was performed at the University of Miami and the University of Washington. The Institutional Review Board of the University of Miami Miller School of Medicine and the Institutional Review Board of Medical Sciences Subcommittee at the University of Washington, Seattle, approved this study. The tenets of the Declaration of Helsinki and the Health Insurance Portability and Accountability Act of 1996 regulations were followed. Written informed consents were obtained from all subjects before participation. Six subjects with a normal ocular history, no visual complains, and no identified optic disc, retinal, or choroidal pathologies on examination and six subjects with drusen secondary to AMD were enrolled in the study from January 2017 to March 2017.

### 6.3.1 *Imaging acquisition*

All subjects were scanned in both eyes using the PLEX® Elite 9000 (Carl Zeiss Meditec, Dublin, CA), a swept-source OCTA (SS-OCTA) instrument that employed a 100 kHz light source with a 1060 nm central wavelength and a 100 nm bandwidth, providing an axial

resolution of ~ 5.5μm and a lateral resolution of ~20 μm estimated at the retinal surface[94]. For each eye, both 3x3 mm and 6x6 mm scans centered at the fovea were repeated three times, yielding 6 scans in total. The right eyes were selected for the analysis unless low signal strength (<7) or severe motion artifacts were present. For the 3x3 mm scans, 300 A-lines were acquired for each B-scan and 300 sets of 4 repeated B-scans were acquired for each C-scan, yielding a digital resolution of 10 μm/pixel. For the 6x6 mm scans, 500 A-lines were acquired for each B-scan and 500 sets of 2 repeated B-scans were acquired for each C-scan, yielding a digital resolution of 12 μm/pixel.

### 6.3.2 *Image processing*

After acquiring volumetric OCTA data, two approaches were used to identify the CC slab for later FD segmentation: a semi-automated segmentation software[32] and the automated segmentation provided by the PLEX® Elite. We employed the semi-automated segmentation software[32] to obtain an accurate segmentation of RPE/BM complex and to extract the CC slabs. In addition, we also produced *en face* CC OCTA images using automated segmentation software on the PLEX® Elite. Automated segmentation does a fair job in segmenting the RPE/BM boundary in normal eyes. However, in diseased eyes, this is more problematic. For example, in eyes with drusen, the RPE is deformed and the RPE-fit segmentation from the automated algorithm on the instrument gives a better approximation of the BM location. Therefore, we used the RPE-fit as the reference boundary to extract the CC slab in these eyes, whereas the RPE boundary was used for the normal eyes. However, segmentation errors could still be present even with our RPE-fit scheme, therefore we have chosen to conduct all our quantitative analysis on images produced by semi-automated segmentation.

The CC slab was defined as a 15 μm thick slab, starting 16 μm under the RPE[60], for both segmentation approaches. *En face* images were produced using a maximum projection and possible signal attenuation caused by the RPE/BM complex was compensated for using a previous reported strategy[93]. Retinal projection artifacts were subsequently removed[25] and the corresponding regions were excluded in further analyses. 3x3 mm images were resized as 600x600 pixels (2x magnification from raw OCTA data) and 6x6 mm images were resized as 1000x1000 pixels (2x magnification from raw OCTA data), yielding a pixel size of 5 μm in 3x3 scans and 6 μm in 6x6 scans. To reduce the variability of the signal strength among the subjects, all the images were normalized to a signal strength of nine before the OCTA maps were processed[136].

CC slabs generated by the semi-automated segmentation approach were selected for further quantification (Figure 5. 1: A, D, G). Two methods were used for CC FD segmentation: our previously published complex thresholding strategy[128] using a fuzzy C-means algorithm (the FCM method) and the Phansalkar's local thresholding method ( the Phansalkar method) provided in Image J. Previous studies utilizing the Phansalkar method had all chosen a 15-pixel radius regardless of image size[83, 90, 92, 124, 125, 151-154]. However, the proper use of this method has to consider the physical dimensions of the image, which involves the size of pixels, rather than the pixel numbers in its radius kernel for segmenting the FDs. In this study, to investigate how the radius size would have an effect on the FD segmentation and quantification, we used four different radius options: in 3x3 mm scans, 2 pixels (10 μm, the digital resolution of 3x3 mm scans), 5 pixels (25 μm, around the normal ICD in macular CC), 12 pixels (60 μm), 15 pixels (75 μm) and 30 pixels (150 μm); in 6x6 mm scans, 2 pixels (12 μm, the digital resolution of 6x6 mm scans), 4 pixels (24 μm, around the normal ICD in macular CC), 10 pixels (60 μm),

15 pixels (90 μm) and 25 pixels (150 μm). After CC FD segmentation (Figure 5. 1: B, E H, the FCM method), FDs with an equivalent diameter smaller than 24 μm were excluded from further analysis[128] (Figure 5. 1: C, F, I, using the FCM method).

After CC FD segmentation and binarization, quantitative metrics to describe FDs were calculated, including FD density (FDD), FD number (FDN), mean FD size (MFDS), ICD and total FD area (FDA). FDD was defined as the percentage of image area of no flow to the total image area. FDD and CC vessel density add up to 1. FDN was defined as the total number of FDs detected and MFDS was defined as the average area of individual FDs ICD was calculated as the average minor axis of the ellipses that have the same normalized second central moments of the detected FDs. FDA was calculated as the total area occupied by FDs. Lengths were always measured in μm and areas in $\mu m^{2.}$

### 6.3.3 *Statistical analysis*

Statistical analyses were performed using MATLAB (R2016b; MathWorks, Inc, Natick, Massachusetts, USA). Descriptive statistics were reported as mean and standard deviation (SD). Repeatability was calculated using 3 repeated scans of each subject on the same visit, in the form of coefficient of variation (CV) with pooled means and variances. ANOVA test was used to compare quantitative CC metrics among different methods. Correlation among different methods were analyzed using Pearson's correlation, both r values and p values were reported. P values smaller than 0.05 were considered statistically significant.

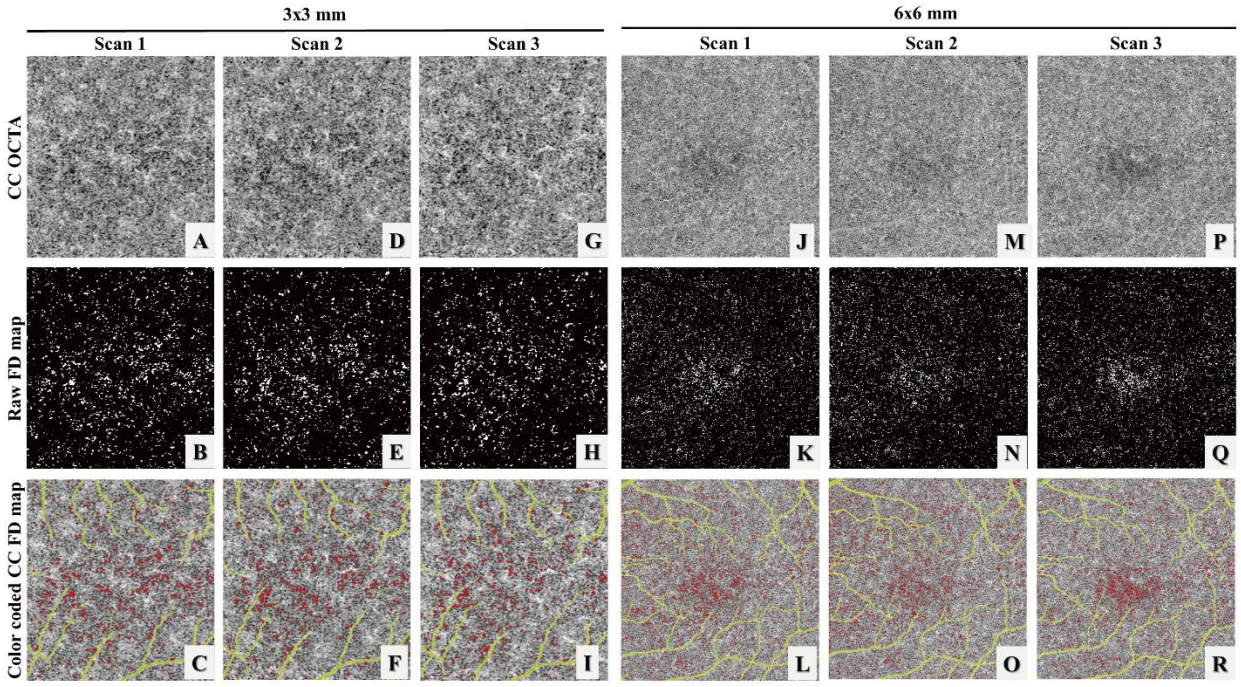


Figure 6.1. Illustration of the choriocapillaris (CC) using three repeated 3x3 mm scans and 6x6 mm scans from a subject with normal eyes.

(A, D, G, J, M, P) Swept source optical coherence tomography angiography (SS-OCTA) CC en face images. (B, E, H, K, N, Q) binary images of segmented CC flow deficits (FDs) (white) using the fuzzy C-means (FCM) method. (C, F, I, L, O, R) color coded CC FD SS-OCTA map (red) after removing FDs below normal inter-capillary distances and projection artifacts (yellow).

## 6.3 RESULTS

The CC is a thin slab beneath the BM and OCTA CC slab appearance can vary significantly if the slab is too close to the RPE or too close to Sattler's layer. Figure 6. 2 demonstrates the appearances of CC OCTA slabs (Figure 6. 2: A-E) and OCT structural slabs (Figure 6. 2: F-J) when the start position for CC slab was selected differently relative to the RPE position. Machine output CC slabs from PLEX® Elite are defined as +29 μm to +49 μm under the RPE segmentation line (Figure 6. 2.E, J), where it appears that the slab may be too deep into the Sattler's layer.

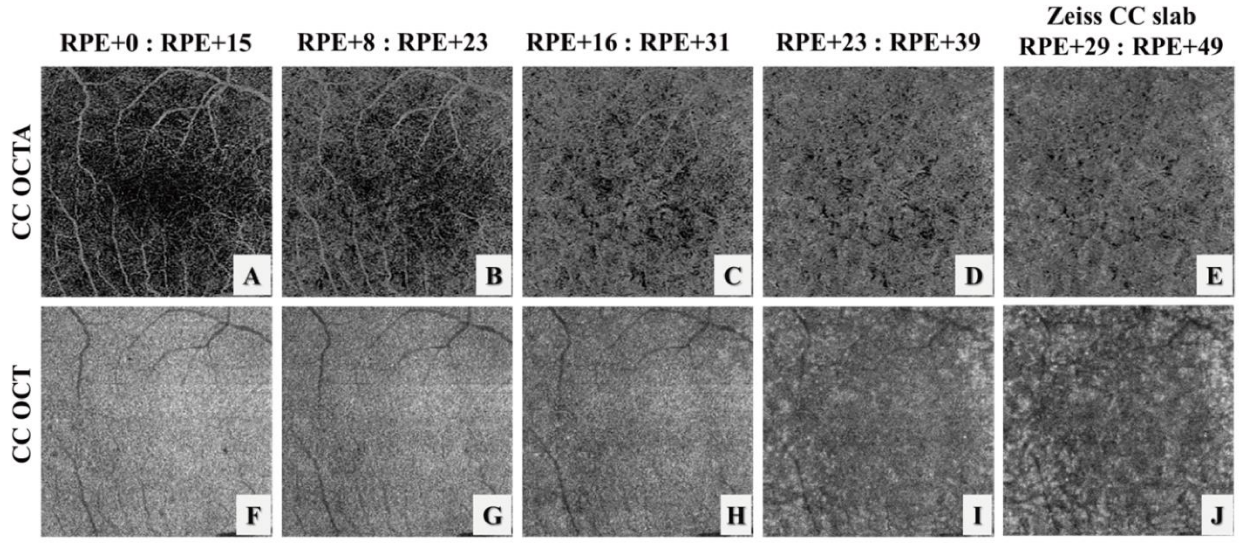


Figure 6.2. Illustration of the choriocapillaris (CC) appearances with different selections of the CC slab position relative to the RPE in a normal eye using automatic segmentation from the instrument.

(A-E) OCT angiography CC slabs with the selection of positions as shown relative to the RPE position. (F-J) corresponding OCT CC structural slabs. Note that since the axial pixel size in PLEX® Elite is 1.9 μm/pixel, the slab thickness in (D) and I is 16 μm rather than 15 μm due to rounding issues.

### 6.3.1 *Repeatability Study*

Six subjects with normal eyes and six subjects with drusen secondary to AMD were recruited for the repeatability study. For each subject, both 3x3 mm and 6x6 mm scans were acquired three times at the same visit. Figure 6. 1, panels A, D, and G show an example of the three repeated 3x3 mm scans while panels J, M and P show an example of the three repeated 6x6 mm scans. Both the FCM method and the Phansalkar method with four different radius choices were used to perform quantitative analyses of CC on each of the 3X3 mm and 6X6 mm averaged scans. Figure 6. 3 demonstrates an example of CC FD segmentation using both the FCM method (Figure 6. 3: B, H) and the Phansalkar method (Figure 6. 3: C-F and I-L) in both scan sizes for

the normal eye. Figure 6. 4 shows the same analysis for a subject with drusen. Qualitatively speaking, the Phansalkar method with larger radius options resulted in more FDs segmented in the same CC image.

Repeatability was assessed using the coefficient of variation (CV) with pooled means and variances. Table 1 shows the CVs for both the FCM method and the Phansalkar method for various radius options in 3x3 mm scans of normal eyes and Table 2 shows the CVs in 3x3 mm scans of eyes with drusen. When using the Phansalkar method, larger radius options tended to result in higher repeatability, likely because higher radius option leads to more and larger FD segmentations, since larger means can lead to smaller CV values. Similarly, Table 3 and 4 demonstrates the repeatability of both methods in normal and drusen for 6x6 mm scans, respectively. For both normal and drusen scans, the Phansalkar method with smaller radius options segmented fewer FDs, therefore a smaller means and typically larger CV values. For both methods, the 3x3 mm scans resulted in higher repeatability compared to the 6x6m mm scans.

Table 6.17. Coefficients of variation for quantitative metrics used to describe flow deficits (FDs) calculated from the fuzzy C-means (FCM) method and the Phansalkar method using various radius options in 3x3 mm scans of normal eyes

| Normal | The FCM method | the Phansalkar method | | | | |
|---|---|---|---|---|---|---|
| | | 2-pixel radius | 5-pixel radius | 12-pixel radius | 15-pixel radius | 30-pixel radius |
| FDD | 3.77% | 10.63% | 5.29% | 3.85% | 3.63% | 3.57% |
| MFDS | 2.65% | 2.13% | 2.97% | 3.69% | 3.94% | 3.69% |
| FDN | 5.12% | 8.63% | 3.45% | 2.25% | 2.13% | 2.25% |
| ICD | 1.21% | 0.57% | 1.62% | 2.13% | 2.32% | 1.98% |
| FDA | 3.16% | 11.42% | 5.79% | 4.16% | 3.90% | 3.73% |

Abbreviations: FCM, Fuzzy C-means; FD, Flow deficit; FDD, FD density; FDN, FD number; MFDS, mean FD size; ICD, inter-capillary distance; FDA, total FD area.

Table 6.18. Coefficients of variation for quantitative metrics used to describe flow deficits (FDs) calculated from the fuzzy C-means (FCM) method and the Phansalkar method using various radius options in 3x3 mm scans of eyes with drusen.

| Drusen | The FCM method | The Phansalkar method | | | | |
|---|---|---|---|---|---|---|
| | | 2-pixel radius | 5-pixel radius | 12-pixel radius | 15-pixel radius | 30-pixel radius |
| FDD | 3.66% | 2.97% | 2.01% | 1.62% | 1.49% | 1.55% |
| MFDS | 2.69% | 2.00% | 4.01% | 3.86% | 4.88% | 4.78% |
| FDN | 2.84% | 2.36% | 2.18% | 2.62% | 3.71% | 3.68% |
| ICD | 1.89% | 1.34% | 1.47% | 1.58% | 1.58% | 1.53% |
| FDA | 3.77% | 3.09% | 2.16% | 1.76% | 1.64% | 1.70% |

Abbreviations: FCM, Fuzzy C-means; FD, Flow deficit; FDD, FD density; FDN, FD number; MFDS, mean FD size; ICD, inter-capillary distance; FDA, total FD area .

Table 6.19. Coefficients of variation for quantitative metrics used to describe flow deficits (FDs) calculated from the fuzzy C-means (FCM) method and the Phansalkar method using various radius options in 6x6 mm scans of normal eyes.

| Normal | The FCM method | The Phansalkar method | | | | |
|---|---|---|---|---|---|---|
| | | 2-pixel radius | 4-pixel radius | 10-pixel radius | 15-pixel radius | 25-pixel radius |
| FDD | 5.33% | 41.14% | 25.32% | 16.40% | 15.23% | 10.58% |
| MFDS | 1.48% | 37.04% | 7.99% | 7.33% | 7.33% | 5.93% |
| FDN | 6.87% | 36.73% | 21.57% | 11.20% | 9.72% | 5.66% |
| ICD | 1.19% | 4.05% | 2.87% | 3.81% | 4.07% | 2.19% |
| FDA | 5.63% | 40.48% | 24.63% | 15.79% | 14.59% | 10.74% |

Abbreviations: FCM, Fuzzy C-means; FD, Flow deficit; FDD, FD density; FDN, FD number; MFDS, mean FD size; ICD, inter-capillary distance; FDA, total FD area.

Table 6.20. Coefficients of variation for quantitative metrics used to describe flow deficits (FDs) calculated from the fuzzy C-means (FCM) method and the Phansalkar method using various radius options in 6x6 mm scans of eyes with drusen.

| Drusen | The FCM method | The Phansalkar method | | | | |
|---|---|---|---|---|---|---|
| | | 2-pixel radius | 4-pixel radius | 10-pixel radius | 15-pixel radius | 25-pixel radius |
| FDD | 6.94% | 33.17% | 20.51% | 10.81% | 9.74% | 3.47% |
| MFDS | 3.75% | 5.60% | 4.66% | 5.18% | 5.10% | 1.84% |
| FDN | 8.82% | 26.22% | 16.31% | 6.43% | 5.50% | 2.13% |
| ICD | 1.33% | 2.29% | 1.77% | 2.34% | 2.16% | 0.89% |
| FDA | 6.41% | 33.77% | 20.86% | 10.97% | 9.87% | 3.28% |

Abbreviations: FCM, Fuzzy C-means; FD, Flow deficit; FDD, FD density; FDN, FD number; MFDS, mean FD size; ICD, inter-capillary distance; FDA, total FD area.

### 6.3.2 *Correlation analysis*

All twelve subjects were grouped and analyzed for correlations between the FCM method and the Phansalkar method. Only one scan was selected from three repeated scans with the highest signal strength, resulting in twelve 3x3 mm scans and twelve 6x6 mm scans. Table 5 shows the mean and standard deviation (SD) values of various quantitative CC metrics in 3x3 mm scans and Table 6 shows the same for 6x6 mm scans. In both 3x3 mm and 6x6 mm scans, the Phansalkar method with larger radius options typically resulted in larger FDD, MFDS, ICD and FDA values. ANOVA tests showed that quantitative CC metrics generated by the different methods are not equivalent.

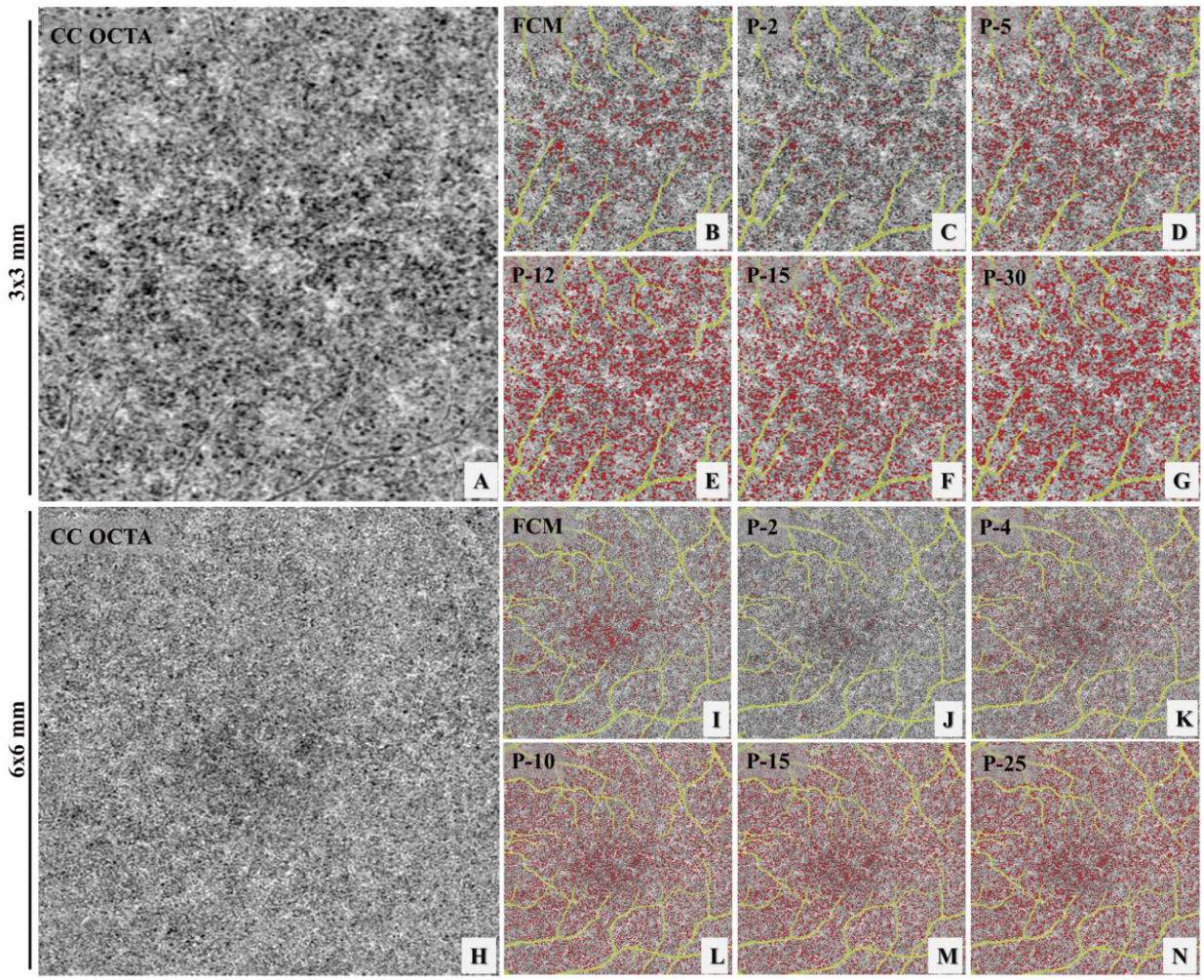


Figure 6.3. Example of choriocapillaris (CC) flow deficit (FD) segmentation in a subject with normal eyes using both a 3x3 mm averaged scan and a 6x6 mm averaged scan.

(**A**) 3x3 mm OCT angiographic (OCTA) CC en face image. (**B**) color coded FD segmentation map (red) using the fuzzy C-means (FCM) method overlaid with the OCTA CC image (grey) and the larger retinal blood vessels (yellow). (**C-G**) color coded FD segmentation map (red) using the Phansalkar method overlaid with OCTA CC image (grey) and the larger retinal vessels (yellow), with 2-pixel radius, 5-pixel radius, 12-pixel radius, 15-pixel radius, and 30-pixel radius, respectively. (**H**) 6x6 mm OCTA CC en face image. (**I**) color coded FD segmentation map (red) by the FCM method overlaid with the OCTA CC en face image (grey) and larger retinal blood vessels (yellow). (**J-N**) color coded FD segmentation map (red) by the Phansalkar method overlaid with the OCTA CC en face image (grey) and larger retinal vessels

(yellow), with 2-pixel radius, 5-pixel radius, 12-pixel radius, 15-pixel radius, and 30-pixel radius, respectively.

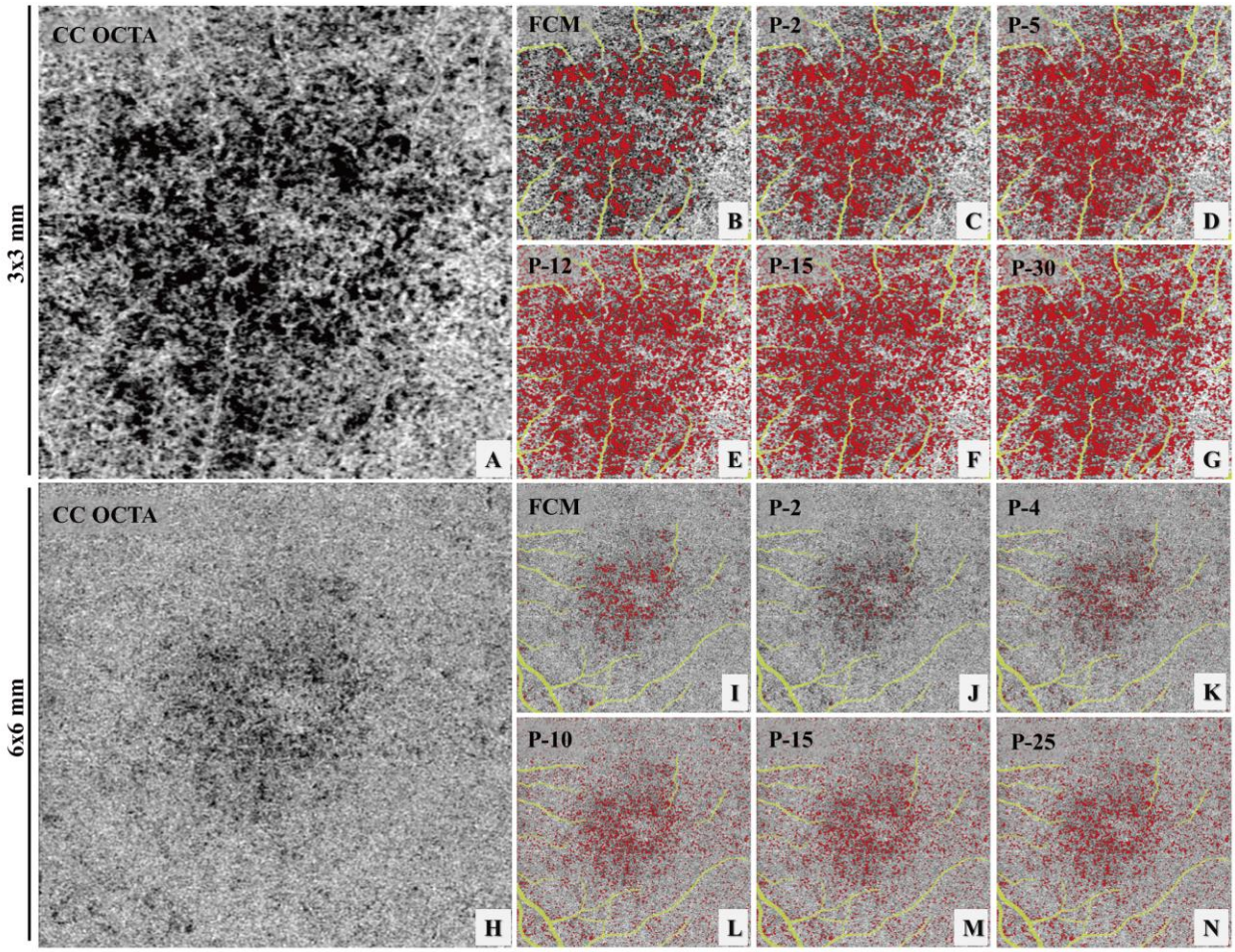


Figure 6.4. Example of choriocapillaris (CC) flow deficit (FD) segmentation in a 3x3 mm scan and a 6x6 mm scan acquired from an AMD subject with drusen.

(**A**) 3x3 mm OCT angiographic (OCTA) CC en face image. (**B**) color coded FD segmentation map (red) using the fuzzy C-means (FCM) method overlaid with the OCTA CC image (grey) and the larger retinal blood vessels (yellow). (**C-G**) color coded FD segmentation map (red) using the Phansalkar method overlaid with OCTA CC image (grey) and the larger retinal vessels (yellow), with 2-pixel radius, 5-pixel radius, 12-pixel radius, 15-pixel radius, and 30-pixel radius, respectively. (**H**) 6x6 mm OCTA CC en face image. (**I**) color coded FD segmentation map (red) by the FCM method overlaid with the OCTA CC en face image (grey) and larger retinal blood vessels (yellow). (**J-N**) color coded FD segmentation map (red) by the Phansalkar method overlaid with the OCTA CC en face image (grey) and larger retinal vessels

(yellow), with 2-pixel radius, 5-pixel radius, 12-pixel radius, 15-pixel radius, and 30-pixel radius, respectively.

Table 6.21. Descriptive statistics for several choriocapillaris (CC) metrics in the 3x3 mm scans over all 12 subjects.

| Mean (SD) | The FCM method | The Phansalkar method | | | | | ANOVA test |
|---|---|---|---|---|---|---|---|
| | | 2-pixel radius | 5-pixel radius | 12-pixel radius | 15-pixel radius | 30-pixel radius | |
| FDD, % (SD) | 7.62 (3.60) | 13.66 (8.18) | 22.03 (7.57) | 27.85 (6.68) | 28.51 (6.58) | 29.6 (6.27) | p<0.001 |
| MFDS, μm (SD) | 1703.6 (766.9) | 1679.4 (881.0) | 1718.8 (733.0) | 2597.8 (1033.5) | 2885.6 (1155.6) | 3475.2 (1389.7) | p<0.001 |
| FDN (SD) | 361.9 (24.1) | 632.6 (150.4) | 1082.5 (156.1) | 931.8 (166.5) | 862.6 (161.1) | 748.0 (149.8) | p<0.001 |
| ICD, μm (SD) | 33.0 (5.0) | 33.0 (5.5) | 33.2 (4.7) | 40.9 (5.5) | 42.8 (5.6) | 45.5 (5.5) | p<0.001 |
| FDA, μm2 (SD) | 0.79 (0.25) | 1.11 (0.64) | 1.80 (0.60) | 2.27 (0.54) | 2.33 (0.53) | 2.42 (0.51) | p<0.001 |

Abbreviations: FCM, Fuzzy C-means; SD, standard deviation; FD, Flow deficit; FDD, FD density; FDN, FD number; MFDS, mean FD size; ICD, inter-capillary distance; FDA, total FD area.

Table 6.22. Descriptive statistics for several choriocapillaris (CC) metrics in the 6x6 mm scans over all 12 subjects.

| Mean (SD) | The FCM method | The Phansalkar method | | | | | ANOVA test |
|---|---|---|---|---|---|---|---|
| | | 2-pixel radius | 4-pixel radius | 10-pixel radius | 15-pixel radius | 25-pixel radius | |
| FDD, % (SD) | 3.98 (0.93) | 1.75 (0.48) | 6.20 (1.37) | 14.04 (2.13) | 15.09 (2.17) | 15.65 (2.30) | p<0.001 |
| MFDS, μm (SD) | 1233.0 (324.5) | 847.8 (151.8) | 864.1 (84.1) | 1292.3 (96.1) | 1475.6 (135.6) | 1619.8 (175.0) | p<0.001 |
| FDN (SD) | 1160.4 (457.6) | 687.4 (174.0) | 2392.2 (621.5) | 3577.4 (566.9) | 3373.1 (520.0) | 3191.8 (515.7) | p<0.001 |

| | | | | | | | |
|---|---|---|---|---|---|---|---|
| ICD, μm (SD) | 28.7 (2.3) | 24.7 (1.9) | 25.0 (1.0) | 30.9 (1.0) | 32.9 (1.2) | 34.3 (1.3) | p<0.001 |
| FDA, μm2 (SD) | 1.80 (0.49) | 0.58 (0.17) | 2.04 (0.46) | 4.61 (0.71) | 4.96 (0.72) | 5.14 (0.77) | p<0.001 |

Abbreviations: FCM, Fuzzy C-means; SD, standard deviation; FD, Flow deficit; FDD, FD density; FDN, FD number; MFDS, mean FD size; ICD, inter-capillary distance; FDA, total FD area.

Pearson's correlation was assessed between quantitative CC metrics using the FCM method and the Phansalkar method, and Table 7 reports the corresponding r and p values for the 3x3 mm scans and Table 8 for the 6x6 mm scans. In the 3x3 mm scans, except for FDN, the Phansalkar method showed significant correlation with the FCM method, regardless of radius options. Such correlations were strongest with a 2-pixel radius option, and decreased for larger radii. In the 6x6 mm scans, the r values are smaller compared to those in the 3x3 mm scans, indicating weaker correlations. The 4-pixel radius (24 μm) option was the only radius option that resulted in significant correlation with the FCM method for all quantitative CC metrics.

Table 6.23. Pearson's correlations between the fuzzy C-means (FCM) method and the Phansalkar method in the 3x3 mm scans.

| 3x3 | The FCM method& the Phansalkar method (2-pixel radius) | The FCM method& the Phansalkar method (5-pixel radius) | The FCM method& the Phansalkar method (12-pixel radius) | The FCM method& the Phansalkar method (15-pixel radius) | The FCM method& the Phansalkar method (30-pixel radius) |
|---|---|---|---|---|---|
| FDD | r = 0.98, p < 0.001 | r = 0.96, p < 0.001 | r = 0.94, p < 0.001 | r = 0.94, p < 0.001 | r = 0.94, p < 0.001 |
| MFDS | r = 0.99, p < 0.001 | r = 0.99, p < 0.001 | r = 0.97, p < 0.001 | r = 0.97, p < 0.001 | r = 0.96, p < 0.001 |
| FDN | r = 0.26, p = 0.46 | r = 0.05, p = 0.88 | r = -0.14, p = 0.69 | r = -0.16, p = 0.65 | r = -0.20, p = 0.58 |
| ICD | r = 0.99, p < 0.001 | r = 0.96, p < 0.001 | r = 0.92, p < 0.001 | r = 0.90, p < 0.001 | r = 0.87, p < 0.001 |

| | | | | | |
|---|---|---|---|---|---|
| FDA | r = 0.97, p < 0.001 | r = 0.94, p < 0.001 | r = 0.90, p < 0.001 | r = 0.90, p < 0.001 | r = 0.89, p < 0.001 |

Abbreviations: FCM, Fuzzy C-means; SD, standard deviation; FD, Flow deficit; FDD, FD density; FDN, FD number; MFDS, mean FD size; ICD, inter-capillary distance; FDA, total FD area.

Table 6.24. Pearson's correlations between the fuzzy C-means (FCM) method and the Phansalkar method in the 6x6 mm scans.

| 6x6 | The FCM method& the Phansalkar method (2-pixel radius) | The FCM method& the Phansalkar method (4-pixel radius) | The FCM method& the Phansalkar method (10-pixel radius) | The FCM method& the Phansalkar method (15-pixel radius) | The FCM method& the Phansalkar method (25-pixel radius) |
|---|---|---|---|---|---|
| FDD | r = -0.04, p = 0.93 | r = 0.68, p = 0.03 | r = 0.71, p = 0.02 | r = 0.69, p = 0.03 | r = 0.68, p = 0.03 |
| MFDS | r = 0.96, p < 0.001 | r = 0.91, p < 0.001 | r = 0.45, p = 0.19 | r = 0.45, p = 0.19 | r = 0.51, p = 0.13 |
| FDN | r = 0.49, p = 0.15 | r = 0.85, p = 0.002 | r = 0.91, p < 0.001 | r = 0.94, p < 0.001 | r = 0.95, p < 0.001 |
| ICD | r = 0.93, p < 0.001 | r = 0.93, p < 0.001 | r = 0.52, p = 0.13 | r = 0.46, p = 0.18 | r = 0.63, p = 0.06 |
| FDA | r = -0.04, p = 0.93 | r = 0.68, p = 0.03 | r = 0.70, p = 0.02 | r = 0.67, p = 0.03 | r = 0.66, p = 0.04 |

Abbreviations: FCM, Fuzzy C-means; SD, standard deviation; FD, Flow deficit; FDD, FD density; FDN, FD number; MFDS, mean FD size; ICD, inter-capillary distance; FDA, total FD area.

## 6.4 DISCUSSION

Visualizing and quantifying the CC in vivo has been a keen interest of many investigators over the decades, especially since the recent technological advances in commercial OCTA systems. However, researchers should stay cautious and vigilant when conducting quantitative

analyses of the CC using OCTA images. There are several important factors that we should be aware that could potentially affect the results of CC quantification.

The first one is the signal intensity. All reported CC FD segmentation methods have used some form of intensity thresholds since morphological filters do not apply. The caveat of using intensity thresholds is that it requires high quality OCTA scans. If the scan signal strength is too low, or partially out of focus, CC OCTA images will appear darker than normal, and this could lead to false positive identifications of CC FDs. More dangerously, when anatomical abnormalities above CC are present, it could block OCT signals. The consequence is the creation of shadows in OCTA CC images, giving rise to false positive CC FDs identification. In order to counteract such situations, an OCT signal compensation strategy[93] should be considered for the attenuated signals detected from structural OCT images.

Another important consideration is the location of the CC slab segmentation. Because the CC is such a thin layer (10μm~20μm[9, 60], which represents as 5~10 pixels in PLEX® Elite), the analysis can be quite sensitive to the distance between the thickness of the CC slab and its distance from the RPE. Figure 6. 2 demonstrates that in commercial systems, the default CC slab might not be optimal, and researchers need to be cautious in using the default slab. This could become even more problematic in pathological cases, because the automatic identification of RPE (or BM) is often incorrect. On PLEX® Elite instruments, researchers might be better off using a CC slab defined by RPE-fit segmentation rather than the default RPE segmentation since accurate CC quantification is almost impossible without accurate CC slab segmentations. Therefore, before a robust automatic segmentation software is rigorously validated, semi-automated segmentation software[32] should be considered because it would ensure the correct identification of the CC slab to the best of our abilities.

Caution is also needed for the segmentation of FDs. Most methods of CC FD segmentation reported so far have used intensity threshold approaches. Using a single global intensity threshold across all cases can be problematic because of signal variability both within scans and across different scans and subjects. Many researchers have used Phansalkar's local thresholding method with a fixed 15-pixel radius, regardless of the pixel sizes. However, a proper selection of the local window radius should be based on actual size (in microns) rather than number of pixels. Too large a window could artificially overestimate the extent of FDs. The present study found that different radius options (10 μm to 150 μm) lead to different quantitative CC metrics and different repeatability. Moreover, the Phansalkar method in 3x3 mm scans of eyes with drusen seems to over identify CC FD areas. This is possibly because the Phansalkar method is designed for low contrast image segmentation, and in cases of extensive CC loss, the OCTA CC image becomes higher contrast, violating its assumption for proper use of this method. Our group has also reported a novel CC FD segmentation method using the mean and SD value from normal population[93]. This SD method has showed significant correlation with the FCM method using a normative database[156].

Another concern is the choice of OCTA scan size. All scan sizes from the same OCTA system share the same lateral resolution, but the digital resolutions (determined by the sampling density) may vary. High speed SS-OCTA system[9] can provide denser scans (~4 μm/pixel) with more repeated B-scans (~10 repeats) and provide higher CC imaging quality. In the PLEX® Elite, the 3x3 mm scan uses 4 repeated B-scans for OCTA and has a digital resolution of 10 μm/pixel. The 6x6 mm scan uses 2 repeated B-scans for OCTA and has a digital resolution of 12 μm/pixel. The 6x6 mm scan contains a larger area at the cost of digital resolution and signal to noise ratio (SNR). Both scan sizes have been reported to be useful in quantitative CC analyses.

The PLEX® Elite also provides 9x9 mm, 12x12 mm and 9x15 mm scans, all using 2 repeated B-scans for OCTA and providing a digital resolution of 18 µm/pixel, 24 µm/pixel and 18 µm/pixel, respectively. Larger scans are valuable because not all pathologies are contained within the 6x6 mm macular region, but they also offer lower digital resolution, lower SNR, and a longer scan time that increases the probability of having motion artifacts. Researchers need to pay extreme caution when using larger sized scans for CC quantification. Moreover, the thickness of the CC layer varies from macula region to equatorial regions, and a uniformly defined thickness of the CC slab will certainly introduce errors.

Lastly, given currently available clinical systems, researchers need to pay attention to what quantifiable parameters can be meaningfully calculated from the CC images. In retinal analysis, parameters such as vascular area density (VAD), vessel skeleton density (VSD), vessel length density (VLD) and vasculature diameter index (VDI), have been used[103]. These quantitative parameters are valid because the retinal inter-capillary distance is much larger than the system lateral resolution and OCTA can resolve the retinal vasculature. Therefore, morphological filters may be used to binarize retinal vessels. However, parameters like VSD/VLD and VDI are not applicable to the CC vasculature given the lateral resolution of current OCTA systems. As we have explained before, ICDs in the CC are too small and OCTA simply cannot resolve the CC vasculature. Because of this technical limitation, we are only able to examine non-perfusion in CC (FDs) but not detailed morphological vascular patterns. Moreover, when CC FD segmentation is performed with the Phansalkar method, the VDI is highly dependent on the size of radius, and a larger radius option would generally lead to wider segmentation of CC vasculature and larger VDI. Therefore, measurements of VSD/VLD and

VDI for the CC vasculature are substantially meaningless, at least in the macula, using the current OCTA resolution.

We have only examined CC quantification with SS-OCTA in this study, not spectral domain OCTA (SD-OCTA). SS-OCTA is superior to SD-OCTA in choroidal imaging due to the deeper penetration with a longer wavelength and less sensitivity roll-off[13]. SD-OCTA may still be useful in quantitative CC analysis. However, greater caution needs to be paid to scan quality in SD-OCTA images. Low quality scans can lead to false positive identification of FDs. SS-OCTA and SD-OCTA systems generally have different SNR and researchers might need to optimize their CC algorithms accordingly from one system to another. Future studies are warranted to investigate how SS-OCTA and SD-OCTA compare in quantitative CC analyses.

In this study, we compared two different CC FD segmentation methods: the FCM method and the Phansalkar method with different radius options. We utilized repeated scans from six subjects with normal eyes and six AMD drusen subjects to assess repeatability of each method. Overall, our results indicate that 3x3 mm scans yield better repeatability than 6x6 mm scans. When using the Phansalkar method, larger radius options resulted in larger FD areas being segmented and typically lower CV. Our data strongly suggests that the radius choice in the Phansalkar method is very important and researchers using this approach for CC analysis should be extremely careful in the proper use of radius parameter. When comparing quantitative CC metrics produced by both methods, 3x3 mm scans also showed stronger correlation among methods than 6x6 mm scans.

There are some limitations in our study. Firstly, there is a lack of ground truth for CC vasculature. Traditional dye-based angiography cannot provide detailed CC imaging suitable for quantification. Adaptive optics OCTA and higher speed SS-OCTA lab-built systems have

demonstrated high resolution images, yet smaller fields of view for CC imaging[9, 60]. We chose to use OCTA CC data acquired by a commercially available OCT system for clinical relevance. Secondly, we have a limited sample size. The purpose of this study was to demonstrate differences in different CC algorithms, and how those methods really compare needs to be studied further with a larger dataset.

In summary, we have demonstrated that CC quantitative analysis with commercial OCTA systems can be complicated. Researchers need to pay close attention to how they choose to conduct such analysis in the future.

# Chapter 7. SUMMARY AND FUTURE WORK

In this dissertation, the emerging application and quantitative potentials of OCTA in ophthalmology were studied. Algorithms to segment different ocular vascular networks were developed and quantitative indices to describe abnormal vasculature were proposed and tested in diseased populations. This dissertation has three main components, the introduction of OCT and OCTA; quantitative analysis of vasculature with OCTA in the retina; and quantitative analysis of vasculature with OCTA in the choriocapillaris. The main objective of this dissertation is to develop quantitative vasculature analysis in human eyes with OCTA, and to use such tools to aid early ocular diseases diagnosis and to avoid or delay vision impairment eventually.

In the first chapter, the basic principles of OCT and OCT's different hardware configurations were introduced. TDOCT was the first generation OCT and largely limited by its scanning speed. The introduction of FDOCT has significantly improved OCT's scanning speed and allowed 3D scans of human eye clinically. Currently there are two types of FDOCT: SDOCT and SSOCT. SSOCT provides better sensitivity and longer imaging range though more expensive compared to SDOCT. Data from both types of systems were analyzed in this dissertation. The higher scanning speed also allowed the introduction of OCTA, a non-invasive angiography technique. With OCTA, it is possible to acquire a snapshot of 3D ocular vasculature in human eye in clinical settings. With such information, it is possible to develop tools that can quantitatively describe the integrity of ocular vasculature and those quantitative indices can be used to establish correlation between OCTA data and disease pathology and eventually achieve earlier diagnosis, more accurate treatment monitoring and overall disease management.

In Chapter 2, quantitative analysis of retinal vasculature with OCTA was studied. A comprehensive quantification tool for human retina was developed and multiple parameters were proposed to describe retinal vasculature function and morphology. Blood perfusion was quantified using VAD, blood vessel length was quantified using VSD, blood vessel caliber was quantified using VDI and blood vessel morphological complexity was quantified using VCI. Moreover, the pathological blood flow impairment was quantified using FIZ and the amount of blood flow passing unit area in unit time was quantified using flux. With those proposed parameters, we achieve high repeatability in both normal and diseased subjects. Our analysis has also been proven practical and useful in differentiating disease severity stages in DR[157], RVO[106], uveitis[107] and glaucoma.[137, 158-161].

In chapter 3-6, quantitative analysis of CC with OCTA was studied. Using OCTA to visualize CC is a different story than using OCTA to visualize retina. The main reason is that the ICD in CC is a lot smaller than the ICD in retina. Therefore, CC visualization is largely limited by the OCTA's lateral resolution. When the ICD of vasculature is considerably larger than the system's lateral resolution, the SNR doesn't need to be extremely high to achieve high imaging quality. But when the ICD of vasculature is smaller or comparable with the system's lateral resolution, high SNR is essential for good image quality. In this dissertation, two approaches was proposed to increase system SNR in CC imaging. Firstly in chapter 3, a novel OCTA approach utilizing both AM and GM was proposed and validated for a higher contrast and strong SNR, while using the complex signal based OCTA approach. Then in chapter 4, a novel registration and averaging approach was introduced to further increase the SNR and contrast for CC imaging. Other than visualization, the quantification of CC is also different from retinal vasculature. Due to the difference in ICD, OCTA cannot always resolve detailed CC network all the time.

Therefore, it is not possible to use same morphological filters and thresholding method developed for retina directly in CC. To counteract such differences, a new vasculature segmentation algorithm was developed specifically for CC in chapter 4, one based on the fuzzy C-means clustering technique. With this novel algorithm, CC FDs were segmented and quantified rather than the vasculature.

In chapter 5, the proposed CC quantification algorithm was tested on a database consisting normal subjects and subjects with diagnosis of various uveitis diseases. This study is very meaningful because it was conducted completely in a clinical setting. The OCTA system used in this study is commercially available and FDA approved. No manual segmentation for the data was required and images acquired from the OCTA machine was directly analyzed by proposed CC quantification analysis. This study can be easily be reproduced by other researchers proving our algorithm. Using this dataset, not only were we able to find that CC alterations do not happen to all uveitis diseases, just ones that have choroidal involvement, but we were also able to find that MFDS is a stronger parameter than FDD in detecting CC abnormality in uveitis. This study could also attest to the validity and robustness of our proposed algorithm.

CC quantitative analysis with OCTA has been one of the hot topics in ophthalmology for the past two year. Many researchers have attempted studies conducting quantitative CC analyses. However, as explained before, imaging and quantifying CC is very different from retina and there are many details that researchers need to pay attention to. In chapter 6, The unique case of CC imaging and quantification was explained and the comparison between our proposed algorithm and a popularly used algorithm was conducted. In this chapter, the objective is to outline why CC imaging and quantification is different from retina and how should researcher

approach CC quantification. Such as how to select a proper CC slab, how to judge signal strength of selected cases and what quantitative parameters can or cannot be used.

Overall, this dissertation aims to develop a quantitative tool for ocular vasculature imaging. It is believed that vasculature alternation is an important indicator of disease pathology, if we can describe ocular vasculature in an objective and reliable way; we can study the disease pathology progression better, diagnose diseases earlier, make better treatment decisions and overall provide better clinical care for patients.

The ability to quantitative describe vasculature integrity will also be essential for large-scale clinical trials. With algorithms developed in this dissertation, the next step would be applying such tools into larger scale clinical studies for ocular diseases. For example, the developed CC analysis tool would be very useful in AMD clinical trials. AMD is considered one of the leading causes for blindness in the U.S. Many researchers have speculated that the integrity of CC is correlated with the diseases progression, or even that CC could potentially be an indicator of diseases activity. Our CC quantification tool would be very useful in testing such hypothesis and advance human knowledge in diseases like AMD.

# BIBLIOGRAPHY


1. Bourne, R.R., et al., *Magnitude, temporal trends, and projections of the global prevalence of blindness and distance and near vision impairment: a systematic review and meta-analysis.* The Lancet Global Health, 2017. **5**(9): p. e888-e897.
2. AAO. *US Eye Disease Statistics*. 2019; Available from: https://www.aao.org/eye-disease-statistics.
3. Rabb, M.F., et al., *Fluorescein angiography of the fundus: a schematic approach to interpretation.* Survey of ophthalmology, 1978. **22**(6): p. 387-403.
4. Slakter, J.S., et al., *Indocyanine-green angiography.* Current opinion in ophthalmology, 1995. **6**(3): p. 25-32.
5. Yannuzzi, L.A., et al., *Fluorescein angiography complication survey.* Ophthalmology, 1986. **93**(5): p. 611-617.
6. Bushberg, J.T. and J.M. Boone, *The essential physics of medical imaging*. 2011: Lippincott Williams & Wilkins.
7. Pavlin, C.J., et al., *Ultrasound biomicroscopy of anterior segment tumors.* Ophthalmology, 1992. **99**(8): p. 1220-1228.
8. Huang, D., et al., *Optical coherence tomography.* Science (New York, NY), 1991. **254**(5035): p. 1178.
9. Gorczynska, I., et al. *Imaging of the human choroid with a 1.7 MHz A-scan rate FDML swept source OCT system*. in *Ophthalmic Technologies XXVII*. 2017. International Society for Optics and Photonics.
10. Cui, D., et al., *Dual spectrometer system with spectral compounding for 1-μm optical coherence tomography in vivo.* Optics letters, 2014. **39**(23): p. 6727-6730.
11. Drexler, W., et al., *Ultrahigh-resolution ophthalmic optical coherence tomography.* Nature medicine, 2001. **7**(4): p. 502.
12. Song, S., J. Xu, and R.K. Wang, *Long-range and wide field of view optical coherence tomography for in vivo 3D imaging of large volume object based on akinetic programmable swept source.* Biomedical optics express, 2016. **7**(11): p. 4734-4748.
13. Xu, J., et al., *Long ranging swept-source optical coherence tomography-based angiography outperforms its spectral-domain counterpart in imaging human skin microcirculations.* Journal of biomedical optics, 2017. **22**(11): p. 116007.
14. Wang, R.K., et al., *Three dimensional optical angiography.* Optics express, 2007. **15**(7): p. 4083-4097.
15. Moult, E., et al., *Ultrahigh-speed swept-source OCT angiography in exudative AMD.* Ophthalmic surgery, lasers & imaging retina, 2014. **45**(6): p. 496.
16. Hwang, T.S., et al., *Optical coherence tomography angiography features of diabetic retinopathy.* Retina (Philadelphia, Pa.), 2015. **35**(11): p. 2371.
17. Spaide, R.F., *Volume-Rendered Optical Coherence Tomography of Diabetic Retinopathy Pilot Study.* American journal of ophthalmology, 2015. **160**(6): p. 1200-1210.
18. Kobrin Klein, B.E., *Overview of epidemiologic studies of diabetic retinopathy.* Ophthalmic epidemiology, 2007. **14**(4): p. 179-183.
19. Klein, R., et al., *The epidemiology of age-related macular degeneration.* American journal of ophthalmology, 2004. **137**(3): p. 486-495.
20. Kashani, A.H., et al., *OPTICAL COHERENCE TOMOGRAPHY ANGIOGRAPHY OF RETINAL VENOUS OCCLUSION.* RETINA, 2015. **35**(11): p. 2323-2331.

21. Zhang, Q., et al., *SWEPT SOURCE OPTICAL COHERENCE TOMOGRAPHY ANGIOGRAPHY OF NEOVASCULAR MACULAR TELANGIECTASIA TYPE 2.* RETINA, 2015. **35**(11): p. 2285-2299.
22. Mariampillai, A., et al., *Speckle variance detection of microvasculature using swept-source optical coherence tomography.* Optics letters, 2008. **33**(13): p. 1530-1532.
23. Jia, Y., et al., *Split-spectrum amplitude-decorrelation angiography with optical coherence tomography.* Optics express, 2012. **20**(4): p. 4710-4725.
24. Braaf, B., et al., *Angiography of the retina and the choroid with phase-resolved OCT using interval-optimized backstitched B-scans.* Optics express, 2012. **20**(18): p. 20516-20534.
25. Zhang, A., Q. Zhang, and R.K. Wang, *Minimizing projection artifacts for accurate presentation of choroidal neovascularization in OCT micro-angiography.* Biomedical optics express, 2015. **6**(10): p. 4130-4143.
26. Wang, R.K., et al., *Depth-resolved imaging of capillary networks in retina and choroid using ultrahigh sensitive optical microangiography.* Optics letters, 2010. **35**(9): p. 1467-1469.
27. Chu, Z., et al., *Repeatability and Reproducibility of Quantifying Parafoveal Vessel Density in Normal Subjects with OCT-based Microangiography.* Investigative Ophthalmology & Visual Science, 2015. **56**(7): p. 5958-5958.
28. Reif, R., et al., *Quantifying optical microangiography images obtained from a spectral domain optical coherence tomography system.* Journal of Biomedical Imaging, 2012. **2012**: p. 9.
29. Jia, Y., et al., *Quantitative optical coherence tomography angiography of vascular abnormalities in the living human eye.* Proceedings of the National Academy of Sciences, 2015. **112**(18): p. E2395-E2402.
30. Agemy, S.A., et al., *RETINAL VASCULAR PERFUSION DENSITY MAPPING USING OPTICAL COHERENCE TOMOGRAPHY ANGIOGRAPHY IN NORMALS AND DIABETIC RETINOPATHY PATIENTS.* RETINA, 2015. **35**(11): p. 2353-2363.
31. Zhang, Q., et al., *Wide-field imaging of retinal vasculature using optical coherence tomography-based microangiography provided by motion tracking.* Journal of biomedical optics, 2015. **20**(6): p. 066008-066008.
32. Yin, X., J.R. Chao, and R.K. Wang, *User-guided segmentation for volumetric retinal optical coherence tomography images.* Journal of biomedical optics, 2014. **19**(8): p. 086020-086020.
33. Frangi, A.F., et al., *Multiscale vessel enhancement filtering*, in *Medical Image Computing and Computer-Assisted Interventation—MICCAI'98*. 1998, Springer. p. 130-137.
34. Watson, A.B., *Perimetric complexity of binary digital images.* The Mathematica Journal, 2012. **14**: p. 1-40.
35. Mackenzie, P.J. and G.A. Cioffi, *Vascular anatomy of the optic nerve head.* Canadian Journal of Ophthalmology/Journal Canadien d'Ophtalmologie, 2008. **43**(3): p. 308-312.
36. Thorell, M.R., et al., *Swept-source OCT angiography of macular telangiectasia type 2.* Ophthalmic Surgery, Lasers and Imaging Retina, 2014. **45**(5): p. 369-380.
37. Lutty, G., et al., *Changes in choriocapillaris and retinal pigment epithelium in age-related macular degeneration.* Mol Vis, 1999. **5**(35): p. 35.
38. Bhutto, I. and G. Lutty, *Understanding age-related macular degeneration (AMD): relationships between the photoreceptor/retinal pigment epithelium/Bruch's membrane/choriocapillaris complex.* Molecular aspects of medicine, 2012. **33**(4): p. 295-317.
39. Herbort, C.P., *Posterior uveitis: new insights provided by indocyanine green angiography.* Eye, 1998. **12**(5): p. 757-759.
40. Cao, J., et al., *Choriocapillaris degeneration and related pathologic changes in human diabetic eyes.* Archives of Ophthalmology, 1998. **116**(5): p. 589-597.
41. Piccolino, F.C. and L. Borgia, *Central serous chorioretinopathy and indocyanine green angiography.* Retina, 1994. **14**(3): p. 231-242.

42. Hayreh, S.S., *The choriocapillaris.* Albrecht von Graefes Archiv für klinische und experimentelle Ophthalmologie, 1974. **192**(3): p. 165-179.
43. Torczynski, E. and M.O. Tso, *The architecture of the choriocapillaris at the posterior pole.* American journal of ophthalmology, 1976. **81**(4): p. 428-440.
44. Krey, H.F., *Segmental vascular patterns of the choriocapillaris.* American journal of ophthalmology, 1975. **80**(2): p. 198-202.
45. Sarks, J., S. Sarks, and M. Killingsworth, *Evolution of geographic atrophy of the retinal pigment epithelium.* Eye, 1988. **2**(Pt 5): p. 552-577.
46. McLeod, D.S., et al., *Relationship between RPE and choriocapillaris in age-related macular degeneration.* Investigative ophthalmology & visual science, 2009. **50**(10): p. 4982-4991.
47. Mullins, R.F., et al., *Choriocapillaris vascular dropout related to density of drusen in human eyes with early age-related macular degeneration.* Investigative ophthalmology & visual science, 2011. **52**(3): p. 1606-1612.
48. Gerl, V.B., et al., *Extensive deposits of complement C3d and C5b-9 in the choriocapillaris of eyes of patients with diabetic retinopathy.* Investigative ophthalmology & visual science, 2002. **43**(4): p. 1104-1108.
49. Hyvarinen, L., et al., *Fluorescein angiography of the choriocapillaris.* American journal of ophthalmology, 1969. **67**(5): p. 653-666.
50. Hayashi, K., Y. Hasegawa, and T. Tokoro, *Indocyanine green angiography of central serous chorioretinopathy.* International ophthalmology, 1986. **9**(1): p. 37-41.
51. Pauleikhoff, D., et al., *A fluorescein and indocyanine green angiographic study of choriocapillaris in age-related macular disease.* Archives of Ophthalmology, 1999. **117**(10): p. 1353-1358.
52. Gao, S.S., et al., *Optical Coherence Tomography AngiographyOptical Coherence Tomography Angiography.* Investigative ophthalmology & visual science, 2016. **57**(9): p. OCT27-OCT36.
53. Chen, C.-L. and R.K. Wang, *Optical coherence tomography based angiography.* Biomedical optics express, 2017. **8**(2): p. 1056-1082.
54. Kurokawa, K., et al., *Imaging choriocapillaris with adaptive optics optical coherence tomography angiography.* Investigative Ophthalmology & Visual Science, 2016. **57**(12): p. 5915-5915.
55. Fingler, J., et al., *Volumetric microvascular imaging of human retina using optical coherence tomography with a novel motion contrast technique.* Optics express, 2009. **17**(24): p. 22190-22200.
56. Mariampillai, A., et al., *Optimized speckle variance OCT imaging of microvasculature.* Optics letters, 2010. **35**(8): p. 1257-1259.
57. Huang, Y., et al., *Swept-source OCT angiography of the retinal vasculature using intensity differentiation-based optical microangiography algorithms.* Ophthalmic Surgery, Lasers and Imaging Retina, 2014. **45**(5): p. 382-389.
58. Ashton, N., *Observations on the choroidal circulation.* The British journal of ophthalmology, 1952. **36**(9): p. 465.
59. Wybar, K.C., *A study of the choroidal circulation of the eye in man.* Journal of anatomy, 1954. **88**(Pt 1): p. 94.
60. Kurokawa, K., Z. Liu, and D.T. Miller, *Adaptive optics optical coherence tomography angiography for morphometric analysis of choriocapillaris.* Biomedical Optics Express, 2017. **8**(3): p. 1803-1822.
61. Kurokawa, K., et al., *Three-dimensional retinal and choroidal capillary imaging by power Doppler optical coherence angiography with adaptive optics.* Optics express, 2012. **20**(20): p. 22796-22812.
62. Braaf, B., et al., *Phase-stabilized optical frequency domain imaging at 1-μm for the measurement of blood flow in the human choroid.* Optics express, 2011. **19**(21): p. 20886-20903.

63. Choi, W., et al., *Choriocapillaris and choroidal microvasculature imaging with ultrahigh speed OCT angiography.* PloS one, 2013. **8**(12): p. e81499.
64. Braaf, B., et al., *Real-time eye motion correction in phase-resolved OCT angiography with tracking SLO.* Biomedical optics express, 2013. **4**(1): p. 51-65.
65. Baran, U., et al., *High resolution imaging of acne lesion development and scarring in human facial skin using OCT‐based microangiography.* Lasers in surgery and medicine, 2015. **47**(3): p. 231-238.
66. Zagaynova, E., et al., *Endoscopic OCT with forward‐looking probe: clinical studies in urology and gastroenterology.* Journal of biophotonics, 2008. **1**(2): p. 114-128.
67. Arevalo, J.F., *Retinal angiography and optical coherence tomography*. 2009: Springer.
68. Wang, R.K., *Optical microangiography: a label-free 3-D imaging technology to visualize and quantify blood circulations within tissue beds in vivo.* IEEE Journal of Selected Topics in Quantum Electronics, 2010. **16**(3): p. 545-554.
69. Shi, L., et al., *Wide velocity range Doppler optical microangiography using optimized step-scanning protocol with phase variance mask.* Journal of biomedical optics, 2013. **18**(10): p. 106015-106015.
70. Choi, W., et al., *Ultrahigh-speed, swept-source optical coherence tomography angiography in nonexudative age-related macular degeneration with geographic atrophy.* Ophthalmology, 2015. **122**(12): p. 2532-2544.
71. Sardar, D. and L. Levy, *Optical properties of whole blood.* Lasers in medical science, 1998. **13**(2): p. 106-111.
72. Spraul, C.W., et al., *Morphometric changes of the choriocapillaris and the choroidal vasculature in eyes with advanced glaucomatous changes.* Vision research, 2002. **42**(7): p. 923-932.
73. Yoneya, S., M.O. Tso, and K. Shimizu, *Patterns of the choriocapillaris.* International ophthalmology, 1983. **6**(2): p. 95-99.
74. Olver, J., *Functional anatomy of the choroidal circulation: methyl methacrylate casting of human choroid.* Eye, 1990. **4**(2): p. 262-272.
75. Fryczkowski, A.W., *Anatomical and functional choroidal lobuli.* International ophthalmology, 1994. **18**(3): p. 131-141.
76. Malamos, P., et al., *The role of fundus autofluorescence imaging in the study of the course of posterior uveitis disorders.* BioMed research international, 2015. **2015**.
77. Zhang, A., et al., *Methods and algorithms for optical coherence tomography-based angiography: a review and comparison.* Journal of biomedical optics, 2015. **20**(10): p. 100901-100901.
78. Kashani, A.H., et al., *Optical coherence tomography angiography: A comprehensive review of current methods and clinical applications.* Progress in Retinal and Eye Research, 2017.
79. Gorczynska, I., et al. *Imaging of the human choroid with a 1.7 MHz A-scan rate FDML swept source OCT system*. in *Proc. of SPIE Vol*. 2017.
80. Chu, Z., et al., *Complex signal-based optical coherence tomography angiography enables in vivo visualization of choriocapillaris in human choroid.* Journal of biomedical optics, 2017. **22**(12): p. 121705.
81. Jia, Y., et al., *Quantitative optical coherence tomography angiography of vascular abnormalities in the living human eye.* Proceedings of the National Academy of Sciences, 2015: p. 201500185.
82. Gao, S.S., et al., *Choriocapillaris evaluation in choroideremia using optical coherence tomography angiography.* Biomedical optics express, 2017. **8**(1): p. 48-56.
83. Borrelli, E., et al., *REDUCED CHORIOCAPILLARIS FLOW IN EYES WITH TYPE 3 NEOVASCULARIZATION AND AGE-RELATED MACULAR DEGENERATION.* RETINA, 2018.
84. Moreira-Neto, C.A., et al., *Choriocapillaris Loss in Advanced Age-Related Macular Degeneration.* Journal of ophthalmology, 2018. **2018**.

85. Al-Sheikh, M., et al., *Quantitative Features of the Choriocapillaris in Healthy Individuals Using Swept-Source Optical Coherence Tomography Angiography.* Ophthalmic Surgery, Lasers and Imaging Retina, 2017. **48**(8): p. 623-631.
86. Klufas, M.A., et al., *Optical coherence tomography angiography reveals choriocapillaris flow reduction in placoid chorioretinitis.* Ophthalmology Retina, 2017. **1**(1): p. 77-91.
87. Salvatore, S., et al., *Multimodal imaging in acute posterior multifocal placoid pigment epitheliopathy demonstrating obstruction of the choriocapillaris.* Ophthalmic Surgery, Lasers and Imaging Retina, 2016. **47**(7): p. 677-681.
88. Ferrara, D., N.K. Waheed, and J.S. Duker, *Investigating the choriocapillaris and choroidal vasculature with new optical coherence tomography technologies.* Progress in retinal and eye research, 2016. **52**: p. 130-155.
89. Whitmore, S.S., et al., *Complement activation and choriocapillaris loss in early AMD: implications for pathophysiology and therapy.* Progress in retinal and eye research, 2015. **45**: p. 1-29.
90. Uji, A., et al., *Choriocapillaris imaging using multiple en face optical coherence tomography angiography image averaging.* JAMA ophthalmology, 2017. **135**(11): p. 1197-1204.
91. Mo, S., et al., *Visualization of radial peripapillary capillaries using optical coherence tomography angiography: the effect of image averaging.* PloS one, 2017. **12**(1): p. e0169385.
92. Spaide, R.F., *Choriocapillaris flow features follow a power law distribution: implications for characterization and mechanisms of disease progression.* American journal of ophthalmology, 2016. **170**: p. 58-67.
93. Zhang, Q., et al., *A Novel Strategy for Quantifying Choriocapillaris Flow Voids Using Swept-Source OCT Angiography.* Investigative ophthalmology & visual science, 2018. **59**(1): p. 203-211.
94. Meditec, C.Z. *Carl Zeiss Meditec Plex Elite 9000 OCT 501(k) premarket report of FDA*. 2016 [cited 2018 30 Sep]; Available from: https://www.accessdata.fda.gov/cdrh_docs/pdf16/K161194.pdf.
95. Sage, D. and M. Unser, *Teaching image-processing programming in Java.* IEEE Signal Processing Magazine, 2003. **20**(6): p. 43-52.
96. Gonzalez, R.C., S.L. Eddins, and R.E. Woods, *Digital Image Publishing Using MATLAB*. 2004: Prentice Hall.
97. Soh, L.-K. and C. Tsatsoulis, *Texture analysis of SAR sea ice imagery using gray level co-occurrence matrices.* CSE Journal Articles, 1999: p. 47.
98. Morimoto, C. and R. Chellappa. *Evaluation of image stabilization algorithms*. in *Acoustics, Speech and Signal Processing, 1998. Proceedings of the 1998 IEEE International Conference on*. 1998. IEEE.
99. Ayres, C.E., et al., *Measuring fiber alignment in electrospun scaffolds: a user's guide to the 2D fast Fourier transform approach.* Journal of Biomaterials Science, Polymer Edition, 2008. **19**(5): p. 603-621.
100. Aja-Fernández, S., A.H. Curiale, and G. Vegas-Sánchez-Ferrero, *A local fuzzy thresholding methodology for multiregion image segmentation.* Knowledge-Based Systems, 2015. **83**: p. 1-12.
101. Zhang, D.-Q. and S.-C. Chen, *A novel kernelized fuzzy c-means algorithm with application in medical image segmentation.* Artificial intelligence in medicine, 2004. **32**(1): p. 37-50.
102. Kodinariya, T.M. and P.R. Makwana, *Review on determining number of Cluster in K-Means Clustering.* International Journal, 2013. **1**(6): p. 90-95.
103. Chu, Z., et al., *Quantitative assessment of the retinal microvasculature using optical coherence tomography angiography.* Journal of biomedical optics, 2016. **21**(6): p. 066008-066008.
104. Krawitz, B.D., et al., *Acircularity index and axis ratio of the foveal avascular zone in diabetic eyes and healthy controls measured by optical coherence tomography angiography.* Vision research, 2017. **139**: p. 177-186.

105. Spaide, R.F., J.M. Klancnik, and M.J. Cooney, *Retinal vascular layers imaged by fluorescein angiography and optical coherence tomography angiography.* JAMA ophthalmology, 2015. **133**(1): p. 45-50.
106. Koulisis, N., et al., *Quantitative microvascular analysis of retinal venous occlusions by spectral domain optical coherence tomography angiography.* PloS one, 2017. **12**(4): p. e0176404.
107. Kim, A.Y., et al., *Quantifying Retinal Microvascular Changes in Uveitis Using Spectral-Domain Optical Coherence Tomography Angiography.* American journal of ophthalmology, 2016. **171**: p. 101-112.
108. Kim, A.Y., et al., *Quantifying Microvascular Density and Morphology in Diabetic Retinopathy Using Spectral-Domain Optical Coherence Tomography AngiographyQuantifying Vascular Changes in DR With SD-OCTA.* Investigative ophthalmology & visual science, 2016. **57**(9): p. OCT362-OCT370.
109. Waizel, M., et al., *Superficial and deep retinal foveal avascular zone OCTA findings of non-infectious anterior and posterior uveitis.* Graefe's Archive for Clinical and Experimental Ophthalmology, 2018: p. 1-8.
110. Spaide, R.F., et al., *REtinal vascular layers in macular telangiectasia type 2 imaged by optical coherence tomographic angiography.* JAMA Ophthalmology, 2015. **133**(1): p. 66-73.
111. Hassan, M., et al., *The role of optical coherence tomography angiography in the Management of Uveitis.* International ophthalmology clinics, 2016. **56**(4): p. 1-24.
112. Talisa, E., et al., *Retinal and choroidal vasculature in birdshot chorioretinopathy analyzed using spectral domain optical coherence tomography angiography.* Retina, 2015. **35**(11): p. 2392-2399.
113. Khairallah, M., et al., *Optical coherence tomography angiography in patients with Behcet uveitis.* Retina, 2017. **37**(9): p. 1678-1691.
114. Pichi, F., et al., *The application of optical coherence tomography angiography in uveitis and inflammatory eye diseases.* Progress in retinal and eye research, 2017. **59**: p. 178-201.
115. Graham, E., et al., *Neovascularisation associated with posterior uveitis.* British journal of ophthalmology, 1987. **71**(11): p. 826-833.
116. Pakzad-Vaezi, K., et al., *Swept-Source OCT Angiography of Serpiginous Choroiditis.* Ophthalmology Retina, 2017.
117. Howes, E.L. and V.K. Cruse, *The structural basis of altered vascular permeability following intraocular inflammation.* Archives of Ophthalmology, 1978. **96**(9): p. 1668-1676.
118. Nazari, H., et al., *Choroidal atrophy and loss of choriocapillaris in convalescent stage of Vogt-Koyanagi-Harada disease: in vivo documentation.* Journal of ophthalmic inflammation and infection, 2014. **4**(1): p. 9.
119. Aggarwal, K., et al., *The Role of Optical Coherence Tomography Angiography in the Diagnosis and Management of Acute Vogt–Koyanagi–Harada Disease.* Ocular immunology and inflammation, 2018. **26**(1): p. 142-153.
120. Zhang, Q., et al., *Ultra-wide optical coherence tomography angiography in diabetic retinopathy.* Quantitative imaging in medicine and surgery, 2018. **8**(8): p. 743.
121. Pepple, K.L., et al., *Use of En Face Swept-Source Optical Coherence Tomography Angiography in Identifying Choroidal Flow Voids in 3 Patients With Birdshot Chorioretinopathy.* JAMA ophthalmology, 2018. **136**(11): p. 1288-1292.
122. Cheung, C.M.G., et al., *Characterization and differentiation of polypoidal choroidal vasculopathy using swept source optical coherence tomography angiography.* Retina, 2017. **37**(8): p. 1464-1474.
123. Jung, J.J., et al., *Swept-source optical coherence tomography angiography for choroidal neovascularization after bevacizumab and photodynamic therapy.* American Journal of Ophthalmology Case Reports, 2016. **1**: p. 1-4.

124. Nassisi, M., et al., *Choriocapillaris impairment around the atrophic lesions in patients with geographic atrophy: a swept-source optical coherence tomography angiography study.* British Journal of Ophthalmology, 2018: p. bjophthalmol-2018-312643.
125. Rochepeau, C., et al., *Optical Coherence Tomography Angiography Quantitative Assessment of Choriocapillaris Blood Flow in Central Serous Chorioretinopathy.* American journal of ophthalmology, 2018. **194**: p. 26-34.
126. Al-Sheikh, M., et al., *Quantitative OCT angiography of the retinal microvasculature and the choriocapillaris in myopic eyes.* Investigative ophthalmology & visual science, 2017. **58**(4): p. 2063-2069.
127. Spaide, R.F., et al., *Optical coherence tomography angiography.* Progress in retinal and eye research, 2018. **64**: p. 1-55.
128. Chu, Z., et al., *Improving visualization and quantitative assessment of choriocapillaris with swept source OCTA through registration and averaging applicable to clinical systems.* Scientific reports, 2018. **8**(1): p. 16826.
129. Bland, J.M. and D.G. Altman, *Measurement error proportional to the mean.* Bmj, 1996. **313**(7049): p. 106.
130. Cao, J.H., et al., *Birdshot chorioretinitis lesions on indocyanine green angiography as an indicator of disease activity.* Retina, 2016. **36**(9): p. 1751-1757.
131. Bouchenaki, N., et al., *Assessment and classification of choroidal vasculitis in posterior uveitis using indocyanine green angiography.* Klinische Monatsblätter für Augenheilkunde, 2002. **219**(04): p. 243-249.
132. Howe, L., et al., *Indocyanine green angiography in inflammatory eye disease.* Eye, 1998. **12**(5): p. 761.
133. Rao, N.A., *Pathology of Vogt–Koyanagi–Harada disease.* International ophthalmology, 2007. **27**(2-3): p. 81-85.
134. Lauermann, J.L., N. Eter, and F. Alten, *Optical coherence tomography angiography offers new insights into choriocapillaris perfusion.* Ophthalmologica, 2018. **239**(2-3): p. 74-84.
135. Wang, Q., et al., *Vascular density in retina and choriocapillaris as measured by optical coherence tomography angiography.* American journal of ophthalmology, 2016. **168**: p. 95-109.
136. Zhang, Q., et al., *Projection artifact removal improves visualization and quantitation of macular neovascularization imaged by optical coherence tomography angiography.* Ophthalmology retina, 2017. **1**(2): p. 124-136.
137. Richter, G.M., et al., *Structural and Functional Associations of Macular Microcirculation in the Ganglion Cell-Inner Plexiform Layer in Glaucoma Using Optical Coherence Tomography Angiography.* Journal of glaucoma, 2018. **27**(3): p. 281-290.
138. Chan, G., et al., *In vivo optical imaging of human retinal capillary networks using speckle variance optical coherence tomography with quantitative clinico-histological correlation.* Microvascular research, 2015. **100**: p. 32-39.
139. Zheng, F., et al., *Age-Dependent Changes in the Macular Choriocapillaris of Normal Eyes Imaged with Swept-Source OCT Angiography.* American journal of ophthalmology, 2019.
140. Zhang, Q., et al., *Accurate estimation of choriocapillaris flow deficits beyond normal intercapillary spacing with swept source OCT angiography.* Quantitative imaging in medicine and surgery, 2018. **8**(7): p. 658.
141. Matet, A., et al., *PATTERNS OF CHORIOCAPILLARIS FLOW SIGNAL VOIDS IN CENTRAL SEROUS CHORIORETINOPATHY: An Optical Coherence Tomography Angiography Study.* Retina (Philadelphia, Pa.), 2018.
142. Chen, C.-L., et al., *Optic nerve head perfusion in normal eyes and eyes with glaucoma using optical coherence tomography-based microangiography.* Quantitative imaging in medicine and surgery, 2016. **6**(2): p. 125.

143. Samara, W.A., et al., *Quantitative optical coherence tomography angiography features and visual function in eyes with branch retinal vein occlusion.* American journal of ophthalmology, 2016. **166**: p. 76-83.
144. Pepple, K.L., et al., *Use of En Face Swept-Source Optical Coherence Tomography Angiography in Identifying Choroidal Flow Voids in 3 Patients With Birdshot Chorioretinopathy.* JAMA ophthalmology, 2018.
145. Otsu, N., *A threshold selection method from gray-level histograms.* IEEE transactions on systems, man, and cybernetics, 1979. **9**(1): p. 62-66.
146. Nesper, P.L., B.T. Soetikno, and A.A. Fawzi, *Choriocapillaris nonperfusion is associated with poor visual acuity in eyes with reticular pseudodrusen.* American journal of ophthalmology, 2017. **174**: p. 42-55.
147. Borrelli, E., et al., *Impact of Choriocapillaris Flow on Multifocal Electroretinography in Intermediate Age-Related Macular Degeneration Eyes.* Investigative ophthalmology & visual science, 2018. **59**(4): p. AMD25-AMD30.
148. Carnevali, A., et al., *Optical coherence tomography angiography analysis of retinal vascular plexuses and choriocapillaris in patients with type 1 diabetes without diabetic retinopathy.* Acta diabetologica, 2017. **54**(7): p. 695-702.
149. Sugano, Y., et al., *Morphometrical evaluation of the choriocapillaris imaged by swept-source optical coherence tomography angiography.* Clinical Ophthalmology (Auckland, NZ), 2018. **12**: p. 2267.
150. Phansalkar, N., et al. *Adaptive local thresholding for detection of nuclei in diversity stained cytology images*. in *Communications and Signal Processing (ICCSP), 2011 International Conference on*. 2011. IEEE.
151. Borrelli, E., et al., *Reduced choriocapillaris flow in eyes with type 3 neovascularization and age-related macular degeneration.* Retina, 2018. **38**(10): p. 1968-1976.
152. Borrelli, E., et al., *Topographic Analysis of the Choriocapillaris in Intermediate Age-related Macular Degeneration.* American journal of ophthalmology, 2018. **196**: p. 34-43.
153. Nassisi, M., et al., *Topographic distribution of choriocapillaris flow deficits in healthy eyes.* PloS one, 2018. **13**(11): p. e0207638.
154. Spaide, R.F., *Choriocapillaris signal voids in maternally inherited diabetes and deafness and in pseudoxanthoma elasticum.* Retina, 2017. **37**(11): p. 2008-2014.
155. Spaide, R.F., *Ising model of choriocapillaris flow.* Retina, 2018. **38**(1): p. 79-83.
156. Chu, Z., et al., *Quantifying choriocapillaris flow deficits using global and localized thresholding methods: a correlation study.* Quantitative Imaging in Medicine and Surgery, 2018.
157. Kim, A.Y., et al., *Quantifying microvascular density and morphology in diabetic retinopathy using spectral-domain optical coherence tomography angiography.* Investigative ophthalmology & visual science, 2016. **57**(9): p. OCT362-OCT370.
158. Richter, G.M., et al., *Peripapillary microvasculature in the retinal nerve fiber layer in glaucoma by optical coherence tomography angiography: focal structural and functional correlations and diagnostic performance.* Clinical ophthalmology (Auckland, NZ), 2018. **12**: p. 2285.
159. Richter, G.M., et al., *Diagnostic Performance of Macular Versus Peripapillary Vessel Parameters by Optical Coherence Tomography Angiography for Glaucoma.* Translational vision science & technology, 2018. **7**(6): p. 21-21.
160. Chang, R., et al., *Comparison of Diagnostic Accuracy of Peripapillary Vessel Parameters from 4.5 x4. 5mm and 6x6mm SD-OCTA Scans for Glaucoma.* Investigative Ophthalmology & Visual Science, 2018. **59**(9): p. 5060-5060.
161. Do, J.L., et al., *Utility of optical coherence tomography angiography in detecting glaucomatous damage in a uveitic patient with disc congestion: A case report.* American Journal of Ophthalmology Case Reports, 2017. **8**: p. 78-83.

# VITA

Zhongdi Chu received her B.Sc. degree in biomedical engineering from Northeastern University, China and her M.Sc. degree in bioengineering from University of Washington, Seattle, USA, in 2013 and 2015, respectively. She received her Ph.D. in bioengineering from University of Washington, Seattle, USA, in 2019, working under supervision of Prof. Ruikang Wang. She is the author/co-author of more than 30 journal articles, and the co-inventor of 2 pending US patents.